UNIVERSITÀ DEGLI STUDI DI PALERMO

Dottorato di Ricerca in Ingegneria Civile, Ambientale, dei Materiali
Dipartimento di Ingegneria Civile, Ambientale, Aerospaziale, dei Materiali
Settore Scientifico Disciplinare ICAR/08 - Scienza delle Costruzioni

MULTI-SCALE COMPUTATIONAL HOMOGENIZATION WITH APPLICATIONS TO MASONRY STRUCTURES

La Dottoressa
Emma La Malfa Ribolla

Il Coordinatore
Prof. Mario Di Paola

Il Tutor
Prof. Giuseppe Giambanco

CICLO XXIX
Anno 2017

Emma La Malfa Ribolla
Palermo, Febbraio 2017
e-mail:emma.lamalfaribolla@unipa.it
e-mail:emmalamalfa@gmail.com
Thesis of the Ph.D. course in *Civil, Environmental, Materials Engineering - Structural and Geotechnical Engineering*
(Ingegneria Civile, Ambientale, dei Materiali - Ingegneria Strutturale e Geotecnica)
Dipartimento di Ingegneria Civile Ambientale, Aerospaziale, dei Materiali
Università degli Studi di Palermo
Scuola Politecnica
Viale delle Scienze, Ed.8 - 90128 Palermo, ITALY
Written in LaTeX
Examples and figures made with *MATLAB*© and *Adobe Illustrator*©

Ad Agostino, Franca ed Emma

Contents

List of Figures

List of Tables

Notations

Tensorial notation is used throughout the text when dealing with theoretical derivations. Voigt or matrix notation is used when developing a numerical algorithm that can be implemented in a computer code.

Tensorial notation

Quantities

Scalar	a
First-order tensor	$\mathbf{u}$
Second-order tensor	$\boldsymbol{\sigma}$
Fourth-order tensor	$\mathbf{E}$

Operators

Dot or scalar product of two first-order tensors	$\mathbf{u} \cdot \mathbf{v}$
Double-dot or scalar product of two second order tensors	$\boldsymbol{\sigma} : \boldsymbol{\varepsilon}$
Double-dot product of a fourth order with a second order tensor	$\mathbf{E} : \boldsymbol{\varepsilon}$
Direct product of two first-order tensors	$\mathbf{r} \otimes \mathbf{x}$
Gradient operator	$\nabla \mathbf{u}$
Divergence operator	$\text{div}\, \boldsymbol{\sigma}$
Triple product of two third order tensors	$\vdots$

Voigt notation

Quantities

Scalar	a
Vector	$\mathbf{u}$
Matrix	$\mathbf{A}$

Operators

Matrix product	$\mathbf{A}\,\mathbf{B}$
Transposition	$\mathbf{A}^T$
Inversion	$\mathbf{A}^{-1}$

Chapter 1

Introduction

Masonry is a heterogeneous material constituted by the assemblage of units and joints. Units can be bricks, blocks, ashlars, adobes, irregular stones and other. Mortar can be clay, bitumen, chalk, lime/cement based mortar, glue and other. Actually the term masonry refers to a wide group of assemblages because a huge number of possible combinations, generated by the geometry, nature and arrangements of units as well as the characteristics of mortar, exists.
Masonry structures represent the most of historical Italian construction heritage and, in the recent past, improving the safety of these structures has represented a priority need. The Italian census in 2001 provides a detailed snapshot of the distribution of the building type, finding that 61.5% of the buildings are made up by masonry, 24.66% by reinforced concrete and the remaining 13.84% by other constituents. Also, the recent seismic events have emphasized the need of safety and conservation that often involve the execution of interventions. In this framework, the development of a reliable stress analyses to verify the safety and properly design strengthening and repairing interventions is fundamental.
A primary source of information can be represented by the study of regular masonry structures, i.e. the ones constituted by the periodic repetition of a representative volume element or unit cell. This can be regarded as the smallest microstructure containing the mechanical informations that governs the main global inelastic phenomena. Handling with regular masonry is clearly a simplification, however, many difficulties are still involved. Masonry is in fact characterized by a strong nonlinear behavior and one of the main problem is associated with the definition of suitable material constitutive laws. In addition, the structural correlated schemes are more complex than the ones adopted for concrete or steel frames structures, as masonry elements require often to be

modeled by two- or three-dimensional elements.
The choice of adequate criteria of modeling requires definitively a comprehensive experimental description of the material, which seems mostly available at the present state of art [52, 75, 76]. The experimental studies have showed how the behavior of masonry is dependent not only on the composition of units and joints, but also on how they are arranged.

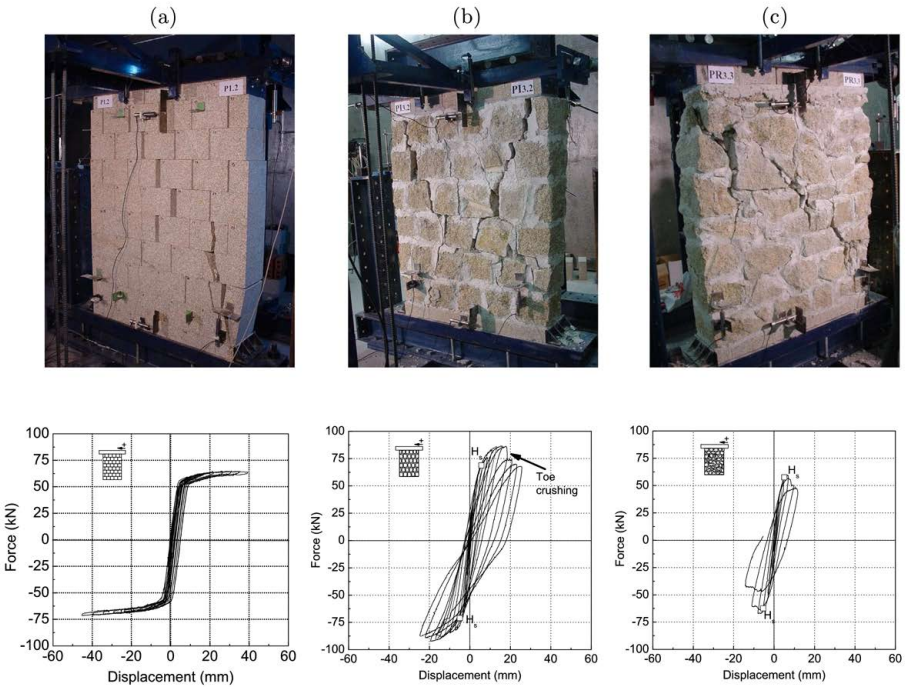

Figure 1.1: Typical deformations configurations and load-displacement diagrams obtained for (a) dry masonry walls; (b) irregular walls; (c) rubble walls. (Adapted from [90]).

An interesting example on how the masonry meso-structure influences the global response is given in the work of Vasconcelos and Lourenço.
Three different types of stone masonry walls with the same external geometry are in plane tested under cyclic shear, namely regular dry stone masonry, irregular mortared joints masonry and rubble masonry. Not only the strength and stiffness degradation of the walls is rather different but also the strength en-

velope found mismatches, with a tangent of the friction angle varying between 0.4 (for dry stone masonry), 0.3 (for irregular masonry) and 0.2 (for rubble masonry).

1.1 Modeling strategies for masonry structures

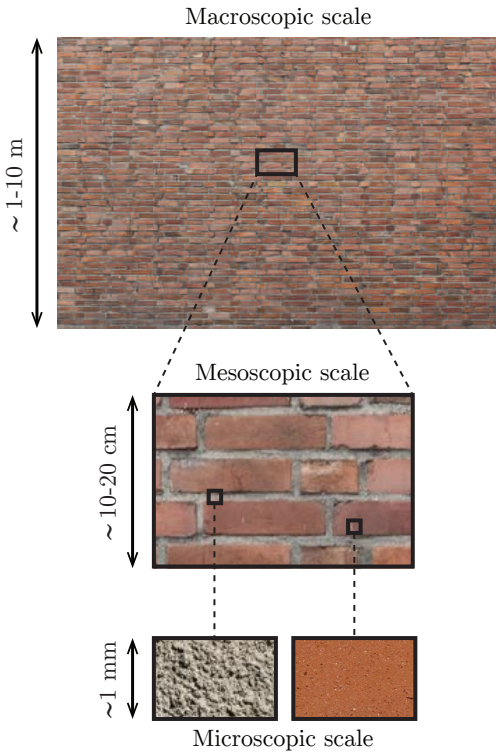

Figure 1.2: Masonry material: the three scales of interest. (Adapted from [59]).

Several approaches have been proposed in literature for modeling masonry and considering the heterogeneity of the material. The different modeling strategies usually depends on the choice of the scale of interest. In fact, different scales of interest or of observation can be distinguished for masonry material. The *macroscopic* scale is the global or structural scale. At this scale of observation the structural element can be considered as a continuum and homogeneous

material. The mechanical variables defined at this scale are related to some average material properties and consequently stresses and strains have to be considered as average stress and strain fields.
The *mesoscopic* scale instead is the one where the presence of different materials is recognizable and its characteristic dimensions are the same of the basic constituents dimensions. In this case, stress and strain fields are studied individually for each constituent and interfacial relations are needed to correlate the behavior of different materials. Inelastic phenomena can take place either on one or more of the constituents. In masonry structures, one of the common inelastic phenomenon is the developing of plastic effects at the mortar joints, such as sliding, that causes a nonlinear response of the entire structure. A study at the mesoscopic scale therefore needs not only the knowledge of the mechanical response of the constituents materials, but also a deep vision of the failure mechanism of the composite material.
Finally a *microscopic* scale can be also defined when attention is paid on a further level of detail and the microscopic nature of the basic constituents is analyzed. A mortar joint, for example, may be considered made up of at least two different materials, namely the aggregate and the matrix.

1.1.1 The Macroscopic approach

If no distinction between units and joints is made and the effect of the joints is taken into account in a smeared mode in the formulation of a fictitious continuous material, the modelling approach can be regarded as macroscopic. Actually, the effects of the coexistence of different materials with their interfaces are considered by defining an appropriate homogenized constitutive model proper of the fictitious continuum. Macroscopic modelling represents the simplest way to analyze masonry material and it is a phenomenological approach, in the sense that material laws approximate peculiar behaviors observed experimentally. A complete macro-model should be able to reproduce an orthotropic material with different tensile and compressive strengths along the material axes as well as different behavior for each material axis and this represents a challenging task. On the other hand, the ease of implementation and the computational cost represent advantages of the approach.
Examples of macro-models can be the cases of the smeared crack approach models [7] or no-tension material (NTM) [55]. In the framework of fracture mechanics, the smeared crack approach models consider cracks and joints in average sense modifying the material properties. The crack at a certain point

of the material is established when the stress or the strain exceed a threshold level. Zucchini and Lourenço [96] applied homogenization techniques to masonry without making distinctions between joints and bricks, but treating masonry as an anisotropic homogenized continuum.
The no-tension material model usually assumes an idealized continuous medium made up of non-cohesive aggregate of frictionless spherical granules of infinitely small size, held together by monolateral-compression-only contact forces, i.e. incapable of supporting any tensile stress, where isotropy and homogeneity are assumed [26]. The *no-tension condition* can be written as:

$$\sigma_n = (\mathbf{n} \cdot \boldsymbol{\sigma}) \cdot \mathbf{n} \leqslant 0 \tag{1.1}$$

i.e. the normal stress, σ_n, acting upon any infinitesimal element with unit normal $\mathbf{n}$ cannot be positive, and the second-order tensor $\boldsymbol{\sigma}$ results in being negative semi-definite.
The additive decomposition of total strain tensor $\boldsymbol{\varepsilon}$ is assumed also to hold:

$$\boldsymbol{\varepsilon} = \boldsymbol{\varepsilon}^e + \boldsymbol{\varepsilon}^c \tag{1.2}$$

with $\boldsymbol{\varepsilon}^e$ and $\boldsymbol{\varepsilon}^c$ elastic and inelastic or crack strains, respectively. If condition (1.1) is satisfied as strong inequality, i.e. $\sigma_n < 0 \, \forall n$, the NTM has an indefinitely linear elastic-type behavior; otherwise, if $\sigma_n = 0$ for some n, crack strains $\boldsymbol{\varepsilon}^c$ take place. The latter can be regarded as plastic strains that model the crack opening phenomena, interpreted in the smeared way of continuum mechanics.

1.1.2 The Mesoscopic approach

If the heterogeneous material is analyzed by a discontinuous assembly of units connected by joints, the modelling approach can be regarded as mesoscopic. Clearly, it represents a more rigorous and accurate method since it allows considering the effective anisotropy of the structure and obtaining a global response governed by local effects. On the other hand, it requires a higher computational effort as a finer discretization is needed.
The material constituents are modelled making use of the classical 2D or 3D continuum elements while the joints are simulated through mechanical devices able to reproduce opening-closing, slide and dilatancy phenomena. These mechanical devices, generally called contact elements, are classified in the following categories [30]:

- link elements between two opposite nodes [34] or a node and a segment [94] of the elements in contact;
- continuum finite elements of small but finite thickness sometimes referred as thin layer elements [32];
- zero thickness interface (ZTI) or interphase (ZTIPH) elements in which the displacements discontinuities between the top and bottom sides of the element represent the primary kinematic variables [31].

Part of the present theses involves a mesoscopic modelling where the ZTI model is used to model the mortar joints. The model was firstly used in rock mechanics by Goodman et al. [31] and later developed for different applications by many authors [4, 29, 53].

1.1.2.1 Interface model

In solid mechanics the term interface model refers to a device that connects two or more adjacent solids and is able to simulate the principal deformative modes that develop between the two parts. The mechanical behavior of the interface is modeled by means of constitutive laws written in terms of contact stresses and displacement jumps. Hence, contact stresses and displacement jumps are considered as static and kinematic variables, respectively.
Two main categories of interface models can be distinguished, frictional and cohesive models. Frictional interface models are mostly used to simulate discontinuities in rocks, dry joints or generally parts of structures characterized by pure frictional effects. Differently, cohesive interface models are mostly used to simulate mortar joints in masonry, adhesive layers in composite materials or generally parts of structures where the formation of a crack is the consequence of a decohesion process inside the joint material or at the contact surface between the two different materials. Usually, cohesive interface models consider a cohesive to frictional transition.
With reference to Fig. 1.3 (a), let us consider in the Euclidean space $\Re^3$, referred to the orthonormal frame $(0, \mathbf{i_1}, \mathbf{i_2}, \mathbf{i_3})$, two bodies Ω^+ and Ω^- connected by the joint Ω^j. It is possible to assume that the joint thickness h is small if compared with the characteristic dimensions of the bonded assembly. The two bodies have Lipschitz boundaries $\partial\Omega^+$ and $\partial\Omega^-$ and the joint Ω^j interacts with the two bodies through the two physical interfaces Σ^+ and Σ^- defined as follows

$$\Sigma^+ = \partial\Omega^+ \cap \Omega^j, \quad \Sigma^- = \partial\Omega^- \cap \Omega^j. \tag{1.3}$$

Kinematic conditions and surface loads are applied to the bodies along $\Gamma_u^{+,-}$ and $\Gamma_t^{+,-}$, respectively. The previous problem can be treated in a more simple way by averaging the joint deformation along the thickness h of the interface. With this simplification, the assembly of the body Ω^j and the contact surfaces Σ^+ and Σ^- can be regarded as an interface model Σ, as shown in Fig. 1.3 (b).

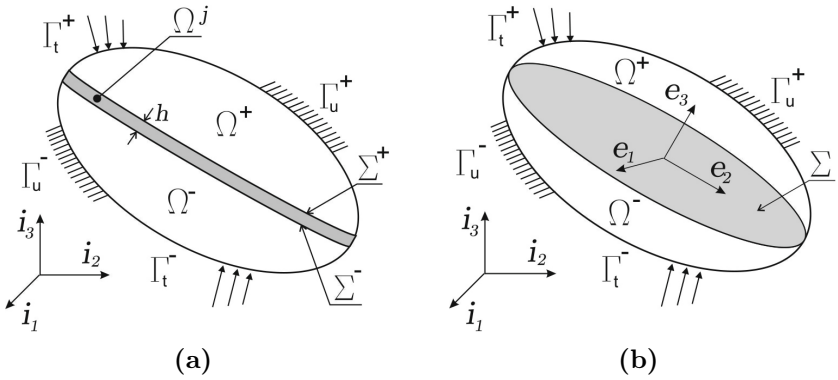

Figure 1.3: Mechanical scheme of an interface interposed between two bodies.

The joint interacts with the two adherents through the following traction components:

$$\mathbf{t}^+ = t_1^+\mathbf{e}_1 + t_2^+\mathbf{e}_2 + t_3^+\mathbf{e}_3, \quad \mathbf{t}^- = t_1^-\mathbf{e}_1 + t_2^-\mathbf{e}_2 + t_3^-\mathbf{e}_3 \tag{1.4}$$

which can be considered as external surface loads for the joint.
Any kinematic phenomenon (opening, sliding, dilatancy) of the interface can be described by the displacement $\mathbf{u}^+$ and $\mathbf{u}^-$ of the surfaces Σ^+ and Σ^-, thus

$$\mathbf{u}(x_1, x_2, x_3) = \frac{x_3}{h}\left(\mathbf{u}^+(x_1, x_2) - \mathbf{u}^-(x_1, x_2)\right) \tag{1.5}$$

with (x_1, x_2, x_3) a Cartesian coordinate system associated to the interphase orthonormal frame. Due to the small thickness of the joint, the strain state $\boldsymbol{\varepsilon}$ is assumed constant along $\mathbf{e}_3$ direction thus

$$\boldsymbol{\varepsilon}(x_1, x_2) = \frac{1}{h} \int_{-\frac{h}{2}}^{\frac{h}{2}} \nabla^s \mathbf{u}(x_1, x_2, x_3) dx_3 \tag{1.6}$$

and substituting the expression (1.5) we have

$$\boldsymbol{\varepsilon}(x_1, x_2) = \frac{1}{2h}([\mathbf{u}] \otimes \mathbf{I}_3 + [\mathbf{u}] \otimes \mathbf{I}_3), \tag{1.7}$$

where $[\mathbf{u}] = \mathbf{u}^+ - \mathbf{u}^-$, $\mathbf{I}_3 = \{\delta_{i_3}\}$ and ∇^s is the symmetric gradient operator. In order to derive the equilibrium equations, let us assign the virtual displacements $\delta\mathbf{u}^+$ and $\delta\mathbf{u}^-$ at the surfaces Σ^+ and Σ^-. The principle of virtual displacements (PVD) asserts that the external work, produced by the contact tractions, equals the internal work developed in the thin joint. According to the hypothesis of a constant strain state along the thickness direction, the conjugate stress state is considered uniform along the same direction and the PVD assume the following form:

$$\int_{\Sigma^+} \delta\mathbf{u}^+ \cdot \mathbf{t}^+ d\Sigma + \int_{\Sigma^-} \delta\mathbf{u}^- \cdot \mathbf{t}^- d\Sigma = h \int_{\Sigma} \delta\boldsymbol{\varepsilon} : \boldsymbol{\sigma}\, d\Sigma. \tag{1.8}$$

Taking into account the kinematic relation (1.7) the PVD becomes

$$\int_{\Sigma^+} \delta\mathbf{u}^+ \cdot \mathbf{t}^+ d\Sigma + \int_{\Sigma^-} \delta\mathbf{u}^- \cdot \mathbf{t}^- d\Sigma = \frac{1}{2} \int_{\Sigma} (\delta[\mathbf{u}] \otimes \mathbf{I}_3 + \delta[\mathbf{u}] \otimes \mathbf{I}_3) : \boldsymbol{\sigma}\, d\Sigma. \tag{1.9}$$

Assuming $\Sigma^+ = \Sigma^- = \Sigma$ and the PVD reads

$$\int_{\Sigma} \delta\mathbf{u}^+ \cdot (\mathbf{t}^+ - \boldsymbol{\sigma} \cdot \mathbf{I}_3) d\Sigma + \int_{\Sigma} \delta\mathbf{u}^- \cdot (\mathbf{t}^- + \boldsymbol{\sigma} \cdot \mathbf{I}_3) d\Sigma = 0 \tag{1.10}$$

which has to hold for all virtual displacements fields. Hence the local equilibrium relations of the interface model are generated:

$$\mathbf{t}^+ = \boldsymbol{\sigma} \cdot \mathbf{I}_3, \qquad \mathbf{t}^- = -\boldsymbol{\sigma} \cdot \mathbf{I}_3 \qquad \text{on } \Sigma \tag{1.11}$$

and they require the continuity conditions of the tractions components.

The constitutive relations can be expressed in terms of contact tractions and elastic displacement discontinuities as follows

$$\mathbf{t} = \mathbf{K}[\mathbf{u}]_e \tag{1.12}$$

where $\mathbf{K}$ is the elastic stiffness matrix expressed by

$$\mathbf{K} = \lceil \ K_{t_1} \ K_{t_2} \ K_n \rfloor \tag{1.13}$$

with K_{t_1} and K_{t_2} the tangential stiffnesses and K_n the normal one. The tangential and normal interface stiffnesses are commonly evaluated from the elastic properties of the bulk material as

$$K_{t_1} = K_{t_2} = \frac{G}{h}, \qquad K_n = \frac{E}{h} \tag{1.14}$$

with G and E the tangential and the Young's moduli of the joint material. The inelastic response associated to dissipative phenomena can be included by introducing different constitutive laws. The latter may be determined in the framework of a consistent thermodynamics.

1.2 Scope and outline

The aim of this thesis is to develop a multi-scale computational homogenization technique for modeling the nonlinear behavior of masonry structures. The technique offers some advantages over the approaches presented in the previous sections. It is in fact based on the coupling of the macroscopic and mesoscopic scales, overcoming the drawbacks of the computational cost and the coarseness of the estimated mechanical response, proper of the meso- and macro-modeling, respectively. According to this technique the constitutive behavior is determined *on the fly* from a mesoscopic unit cell (UC) [67]. The UC is regarded as a sample of the heterogeneous material that is sufficiently large to be statistically representative of the heterogeneous material, i.e. to effectively include a sampling of all micro-structural heterogeneities that occur in the material [43]. In chapter 2 the multi-scale computational homogenization approach is introduced as a standard tool to model heterogeneous materials. It is remarkable that there are several key-aspects that can characterize the approach. The principle of separation of scales represents one of the limits of applicability of the

method. The choice of the UC, statistically representative of the heterogeneous material as well as computationally convenient, is a crucial point too. The scales transitions laws are also not univocally determined and their assumption can influence the mechanical global response. Then, the two main groups of computational homogenization schemes are presented. The first-order computational homogenization scheme fit entirely into a standard local continuum mechanics framework. The macroscopic deformation tensor is calculated for every integration point of the macrostructure and is next used to formulate kinematic boundary conditions to be applied on the associated UC. Only the first gradient of the macroscopic displacement field is included in the framework, which thus is called *first-order*. Conversely, the second-order computational homogenization scheme employs Cosserat or higher order continua to consider those cases in which strong strain and stress gradients arise at the macroscopic level or the mesoscopic dimensions of the UC constituents are comparable to the ones at the macro-level. At the end of chapter 2, the adopted strategy is illustrated.
Chapter 3 presents the UC boundary value problem and its related aspects. The formulation is given in a weak form and is discretized according to a meshless approach. Both linear and periodic boundary conditions are discussed and some computational aspects are studied. The inelastic behavior is concentrated in the mortar joints that are modeled as zero-thickness interface exhibiting a elasto-plastic response.
Therefore, the mesoscopic model response admits the formation and propagation of fractures at the block-joint interfaces. At the macro-scale, the material is elasto-plastic and exhibits a strain-softening response, hence strain localization may occur in one or more narrow bands which are separated by the remaining part of the material by weak discontinuity surfaces. In the computational homogenization approach the evolution of strain localization at the meso- or micro-scales and the macroscopic material failure are coupled making use of the concept of embedded discontinuity [17] or of X-FEM enrichment approach [14]. In the present thesis the macroscopic strain localization is considered making use of the smeared band model proposed by [58] that is based on a weighted-average of the strain in the localized and non localized regions [64]. Several authors treat the strain localization in elasto-plastic materials and most of them use the general theory of continuous bifurcations in order to identify the critical constitutive condition corresponding to the onset of the plastic band. In this sense, chapter 4 presents theoretical and computational aspects of strain localization, including also the simplest one dimensional case.
Chapter 5 presents some global illustrative examples of the adopted strategy.

Numerical comparison with examples already presented in literature as well as experimental validations are provided. It is also analyzed a particular case of study consisting of a wall where a collapse caused by a foundation settlement occurred. Finally, chapter 6 gives a brief summary of the conclusions and recommendations on the practical use of the computational homogenization techniques given attention in this thesis. Perspectives of future developments in computational homogenization strategies are shortly discussed.

Chapter 2

The Multi-Scale Computational Homogenization

2.1 Introduction

Over the last decades, the multi-scale computational homogenization (CH) approach has been considerably developed. This technique couples different scales of interest by means of apposite transition laws capable to exchange informations between different consecutive scales.
Following Nguyen et al. [67], the homogenization methods are able to determine the apparent or overall properties of a heterogeneous material by means of the substitution with an equivalent homogeneous one. According to the authors, the homogenization methods can be classified into three categories: the analytical (AH), the numerical (NH) and the computational homogenization (CH).
The AH aims to derive the material properties at the macro-level through a statistical averaging which takes into account the properties of all phases of the heterogeneous media and their interactions. So far, several rigorous homogenization processes have been developed. Pietruszczak and Niu [73] regarded the masonry material as an orthotropic elastic-brittle material based on a two-phase homogenization theory. Nemat-Nasser and Hori [63] in their pioneering work treated the derivation of the effective elastic properties of two or multi-phases composite materials.
Within the NH methods, the parameters which characterize a macroscopic canonical constitutive model are determined by fitting the data arising from

numerical computations of a mesoscopic element. This approach was employed to model composite materials [16, 37] since it allows the development of the micro-mechanically derived continuum damage and plastic models.
Finally, the CH methods are those in which the macroscopic constitutive behavior is determined *on the fly* from a mesoscopic unit cell (UC) [67]. The UC is regarded as a sample of the heterogeneous material that is sufficiently large to be statistically representative of the heterogeneous material, i.e. to effectively include a sampling of all micro-structural heterogeneities that occur in the material [43].
The CH scheme can be briefly summarized as follows. A macroscopic strain or stress is used to apply kinematic or static boundary conditions to the UC (*macro-meso scale transition*). The equilibrium of the UC is obtained by solving a boundary value problem (BVP) at the mesoscale. Lastly, the macro-strain or macro-stresses are assumed to be the average on the UC of the corresponding meso-strain or meso-stresses (*meso-macro scale transition*). Most of CH methods proposed in the existing literature involve a transfer of field quantities between scales where continuum models are used. In the first-order CH methods, Cauchy models are used at all scales. These methods are based on the *Principle of Separation of Scales*, which asserts that the characteristic size of the UC is much smaller of the size of the structure [27]. Smit et al. [83] applied the first-order homogenization approach to polymeric materials. Feyel and Chaboche [24] modeled the behavior of fiber reinforced structures by employing a FE^2 multi-scale modeling, i.e. approaching to the macro-model and to the UC model by a finite element computation. Massart [59] proposed an enhanced multi-scale model for masonry structures using nonlocal implicit gradient isotropic damage models for both the constituents of the UC.
A second group of CH methods exists. It employs Cosserat or higher order continua to consider those cases in which strong strain and stress gradients arise at the macroscopic level or the mesoscopic dimensions of the UC constituents are comparable to the ones at the macro-level. Examples of such procedures are given in the papers of Kouznetsova et al. [46] and Kaczmarczyk et al. [42], who used second-order macro-continua and first-order meso-continua to investigate the effect of the meso-structure size. Addessi et al. [3] and Addessi and Sacco [2] analyzed masonry panels in the framework of transformation field analysis (TFA) by using a two-dimensional Cosserat continuum for macro-scale model and a nonlinear damage contact-friction model for the mortar joint at the meso-scale. Since the models employed at both observation scales were not the same, Kouznetsova et al. [46] and Kaczmarczyk et al. [42] gave suitable extensions of

the averaging principle in order to correlate the deformation at the meso-scale to the first order and second order strain measured at the macro scale.
This Chapter gives an overview on the main aspects that are involved in the multi-scale CH procedure. For the sake of shortness, only the two main groups of multi-scale CH procedure are reported in the following Section 2.2. Section 2.3 discusses the classical notion of UC and investigates different spatial periodic arrangement that characterize the masonry material. Section 2.4 presents the possible macro-meso scale transition that could be used for the procedure.

2.2 General Procedure

2.2.1 First-Order Computational Homogenization

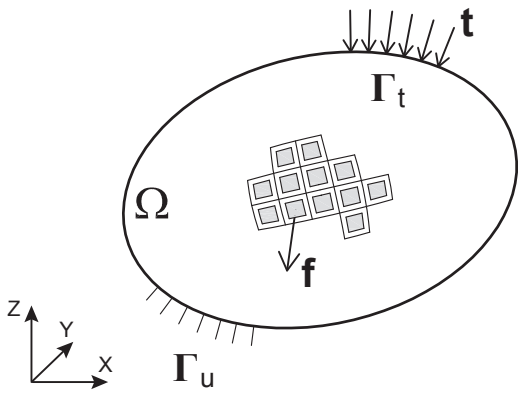

Figure 2.1: Mechanical scheme of a structure constituted by a heterogeneous material.

Let us consider, in the Euclidean space $\Re^3$ referred to the orthonormal frame ($\mathbf{X}$, $\mathbf{Y}$, $\mathbf{Z}$), a structure Ω constituted by a heterogeneous material at the mesoscopic scale, Fig. 2.1. The aim is to derive the structure-properties, or the properties at the macroscopic level (M), based on the kinematical and mechanical phenomena occurring at the mesoscale level (m) of the heterogeneous material. The boundary of the structure is divided in two parts Γ_u and Γ_t where kinematic and loading conditions are specified, respectively. The external actions are the body force $\mathbf{f}$ for unit volume and the surface tractions $\mathbf{t}$. The structural response at the macroscopic level is given by the displacement

$\mathbf{u}_M$, strain $\boldsymbol{\varepsilon}_M$ and stress $\boldsymbol{\sigma}_M$ fields.
The continuous structure is discretized in a finite number of sub-domains or elements Ω_e, Fig. 2.2. The equilibrium of the discretized structure requires the equilibrium of each element, expressed in a weak form as follows:

$$\int_{\Omega_e} \mathbf{f} \cdot \delta\mathbf{u}_M \, \mathrm{d}\Omega + \int_{\Gamma_{te}} \mathbf{t} \cdot \delta\mathbf{u}_M \, \mathrm{d}\Gamma = \int_{\Omega_e} \boldsymbol{\sigma}_M : \delta\boldsymbol{\varepsilon}_M \, \mathrm{d}\Omega. \tag{2.1}$$

In a common CH scheme, $\boldsymbol{\sigma}_M$ is not linked to $\boldsymbol{\varepsilon}_M$ by direct analytical constitutive relations, but it is obtained solving an equilibrium problem at the mesoscale level.
As schematized in Fig. 2.2, in fact, the macroscopic response is evaluated at the sample point (GP) of the finite element as the average of the response of a finite size volume which is representative of the heterogeneous material and is named *unit cell* (UC). The UC has the characteristic size l_m much smaller than the size of the structure l_M. This principle is known as Principle of Separation of scales [27] and leads to the selection of the smallest cell, among those representing the periodic material.

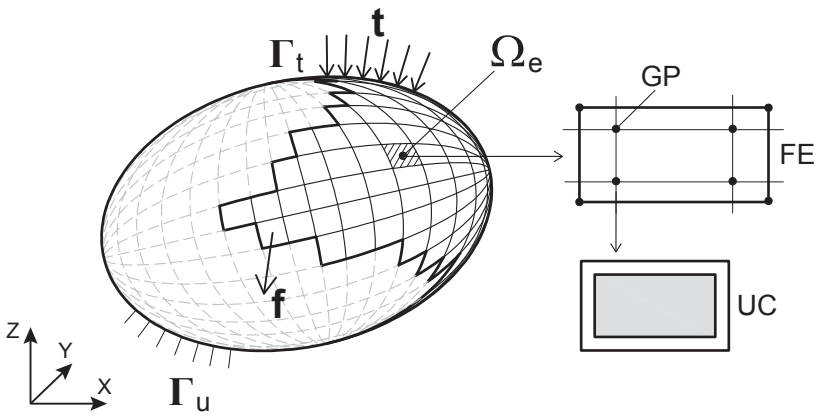

Figure 2.2: Mechanical scheme of the CH strategy.

The scale transition is based on the Hill-Mandel principle [36, 56] which establishes that the virtual work density at the macro-scale must be equal to the average on the volume of the virtual work at the meso-scale over the UC:

$$\boldsymbol{\sigma}_M : \delta\boldsymbol{\varepsilon}_M = \frac{1}{|\Omega_{UC}|} \int_{\Omega_{UC}} \boldsymbol{\sigma}_m : \delta\boldsymbol{\varepsilon}_m \, \mathrm{d}\Omega. \tag{2.2}$$

From Eqs.(2.1) and (2.2) it comes out that the equilibrium of the discretized structure constituted by the heterogeneous material can be solved if the equilibrium of the UC is assessed under specific boundary conditions.
The downscaling operation, also known as *macro-meso transition*, consists in the evaluation of the boundary conditions to be applied to the UC. In the first-order CH, the macro-meso transition is usually "deformation driven" because this procedure can be directly fit into a displacement-based finite element framework. Therefore, the macroscopic deformation tensor is calculated at the material point of the finite element and it is next used to formulate the kinematical boundary conditions to be imposed on the UC associated to this point. If linear boundary conditions are applied:

$$\mathbf{u}_m = \boldsymbol{\varepsilon}_M \, \mathbf{x} \qquad \text{on } \Gamma_{\mathrm{UC}} \tag{2.3}$$

where $\mathbf{u}_m$ are the prescribed values of the displacements for the point of position $\mathbf{x}$ located on the boundary Γ_{UC} of the UC and $\boldsymbol{\varepsilon}_M$ the macroscopic strain. This choice could be easily modified on the basis of the obtained numerical results.
Since the body forces can be neglected and the whole boundary is constrained, the variational form of the UC equilibrium can be expressed as follows:

$$\int_{\Omega_{UC}} \boldsymbol{\sigma}_m : \delta\boldsymbol{\varepsilon}_m \, \mathrm{d}\Omega = 0, \tag{2.4}$$

that has to hold in the presence of the kinematical constraints:

$$\mathbf{u}_m = \bar{\mathbf{u}}_m \qquad \text{on } \Gamma_{\mathrm{UC}}. \tag{2.5}$$

The kinematical constraint (2.5) can be incorporated in the variational equality (2.4) making use of the Lagrange multiplier method, thus

$$\int_{\Omega_{UC}} \boldsymbol{\sigma}_m : \delta\boldsymbol{\varepsilon}_m \, \mathrm{d}\Omega = \int_{\Gamma_{UC}} \delta\mathbf{r} \cdot (\mathbf{u}_m - \bar{\mathbf{u}}_m) \, \mathrm{d}\Gamma + \int_{\Gamma_{UC}} \mathbf{r} \cdot \delta\mathbf{u}_m \, \mathrm{d}\Gamma, \tag{2.6}$$

where $\mathbf{r}$ is the vector of Lagrangian multipliers and $\delta\boldsymbol{\varepsilon}_m$ the virtual strain tensor of the UC related to the virtual displacements, through the following compatibility condition:

$$\delta\boldsymbol{\varepsilon}_m = \nabla^s \delta\mathbf{u}_m \qquad \text{on}\,\Omega_{\text{UC}}. \tag{2.7}$$

The Lagrangian multipliers are those mechanical quantities conjugated to the imposed displacements at the boundary of the UC and represent the reaction forces acting on the same boundary. Invoking the Hill-Mandel equality (2.2) the variational equality (2.6) can be rewritten in the following form

$$\boldsymbol{\sigma}_M : \delta\boldsymbol{\varepsilon}_M = \frac{1}{|\Omega_{UC}|}\left[\int_{\Gamma_{UC}} \delta\mathbf{r}\cdot(\mathbf{u}_m - \bar{\mathbf{u}}_m)\,\mathrm{d}\Gamma + \int_{\Gamma_{UC}} \mathbf{r}\cdot\delta\mathbf{u}_m \mathrm{d}\Gamma\right]. \tag{2.8}$$

Substituting in (2.8) the downscaling Eq.(2.3) and after some mathematical manipulations it is obtained:

$$\left[\boldsymbol{\sigma}_M - \frac{1}{2|\Omega_{UC}|}\int_{\Gamma_{UC}} (\mathbf{r}\otimes\mathbf{x} + \mathbf{x}\otimes\mathbf{r})\,\mathrm{d}\Gamma\right] : \delta\boldsymbol{\varepsilon}_M = \\ = \frac{1}{|\Omega_{UC}|}\int_{\Gamma_{UC}} \delta\mathbf{r}\cdot(\boldsymbol{\varepsilon}_M\mathbf{x} - \bar{\mathbf{u}}_m)\,\mathrm{d}\Gamma. \tag{2.9}$$

Since the previous equation has to hold for any value of $\delta\mathbf{r}$ and $\delta\boldsymbol{\varepsilon}_M$, it provides the following conditions:

$$\boldsymbol{\varepsilon}_M\,\mathbf{x} = \bar{\mathbf{u}}_m \qquad \text{on}\,\Gamma_{\text{UC}} \tag{2.10}$$

$$\boldsymbol{\sigma}_M = \frac{1}{2|\Omega_{UC}|}\int_{\Gamma_{UC}} (\mathbf{r}\otimes\mathbf{x} + \mathbf{x}\otimes\mathbf{r})\,\mathrm{d}\Gamma. \tag{2.11}$$

Equation (2.10) is the macro-meso transition condition here adopted for the multi-scale problem. Equation (2.11) represents the equilibrium condition of the UC but also relates the macroscopic stress to the mesoscopic mechanical response in terms of reaction forces arising along the boundary of the cell and, in this sense, it can be considered as the *meso-macro transition* or upscaling

equation. Fig. 2.3 schematizes the CH procedure where the first gradient of the displacement field is transferred to the mesoscale, hence it was classified as *first-order* CH method [46].

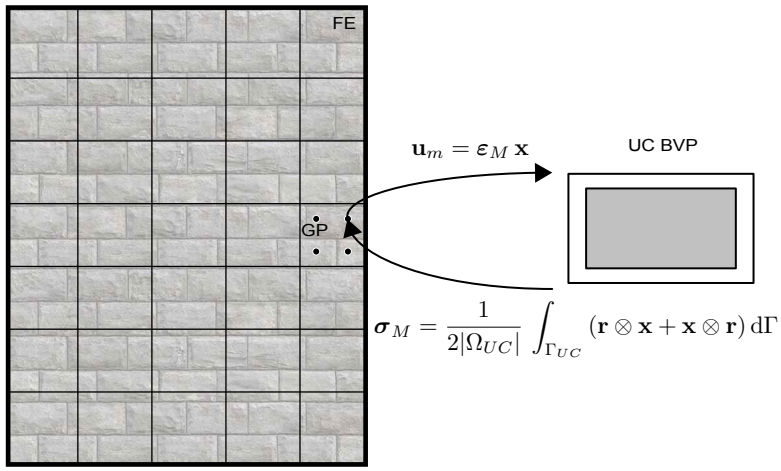

Figure 2.3: Scheme of the first-order CH strategy.

2.2.1.1 Principle of Separation of Scales

The scale separation made in such a framework relies on some basic assumptions. The composition of any heterogeneous solid can generally be considered as an assembly of different constituents, phases, imperfections. However, as the characteristic dimensions of these mesoscopic and microscopic features are still much larger than the molecular dimensions, the use of a continuum approach at this level remains justified. Meanwhile, the mesoscopic length scale is often much smaller than the characteristic length over which the macroscopic excitation varies in space. The distinct hierarchy of scales is known as the *principle of scale separation*. This principle states that the characteristic length scale over which the macroscopic field variables vary, should be much larger than the size of the UC considered. In other words, macroscopic quantities are nearly constant at the level of a UC.
Geers et al. [27] states that "*the aforementioned principle of separation of scales clearly sets limits for the first-order case. As a consequence, large spatial gradients at the macro-scale cannot be resolved. The method is therefore not suited for the analysis of localization problems.*"

To obtain objective results in case of localization problems, the first-order computational homogenization was extended to the second-order computational homogenization [46], in which a length scale was derived from the BVP by adding the gradient of the macroscopic deformation tensor to the boundary conditions of the UC.
An alternative approach is to extend the macro-scale framework with discontinuities to allow localization of deformation at the meso-scale to develop into fracture-like discontinuities at the macro-scale. For this purpose, a decomposition of the macro-scale deformation into an elastic unloading part and an inelastic part has been introduced in a continuous-discontinuous framework by Massart et al. [58]. Following a similar philosophy of tensorial decomposition of the deformation was used to model localization along macro-scale cracks [64].

2.2.2 Second-Order Computational Homogenization

If the first and second gradient of the macroscopic displacement field are used for the boundary conditions imposed to the UC and the generalized Hill-Mandel principle is used to define a macroscopic high order stresses, the CH method can be referred to *second-order* CH method. Second-order CH methods are given in Kouznetsova et al. [46] and Kaczmarczyk et al. [42]. This attempt finds its roots on a limitation of the first-order CH when applied to softening materials. In fact, as it will specified in Chapter 4, when strain localization occurs at the mesoscopic level, the homogenized constitutive equation $\sigma_M - \varepsilon_M$ is a strain softening constitutive equation. The consequence of this is that the macroscopic BVP is ill-posed or, in mathematical terms, the macroscopic BVP loses ellipticity. The numerical effect is that the solution, obtained by the CH procedure when softening materials are adopted at the mesoscale, is sensitive with respect to the macroscopic finite element discretization. However the second-order CH schemes cannot properly deal with softening materials exhibiting deformation beyond a quadratic nature in the displacements [27]. For a finite size material line element, the transformation from the undeformed macroscopic state (position vector $\mathbf{X}$) to the deformed state ($\mathbf{x}$) is obtained using a Taylor expansion truncated after the second-order term, if $\Delta\mathbf{x}$ and $\Delta\mathbf{X}$ are assumed small

$$\Delta\mathbf{x} = \mathbf{F}_M \cdot \Delta\mathbf{X} + \frac{1}{2}\Delta\mathbf{X} \cdot \nabla\mathbf{F}_M \cdot \Delta\mathbf{X}, \tag{2.12}$$

being $\mathbf{F}_M$ the deformation gradient tensor. In order to construct the bound-

ary value problem, Eq. (2.12) is considered, with the extra term $\mathbf{w}$ that represents the fluctuation field at the mesoscopic scale

$$\Delta\mathbf{x} = \mathbf{F}_M \cdot \Delta\mathbf{X} + \frac{1}{2}\Delta\mathbf{X} \cdot \nabla\mathbf{F}_M \cdot \Delta\mathbf{X} + \mathbf{w}. \tag{2.13}$$

The key point in the second-order two-scale framework, resides in applying relation (2.13) to the UC, such that a classical boundary value problem is obtained. The equilibrium equation in the absence of body forces is

$$\nabla \cdot \mathbf{P}_m^T = \mathbf{0}, \tag{2.14}$$

being $\mathbf{P}_m$ the mesoscopic first Piola-Kirchoff stress tensor, related to the Cauchy stress tensor by $\mathbf{P}_m = \det(\mathbf{F}_m)\boldsymbol{\sigma}_m \cdot \mathbf{F}^{-T}$. Since the model deals with a full gradient higher-order continuum, the extended Hill-Mandel relation reads

$$\mathbf{P}_M : \delta\mathbf{F}_M^T + \mathbf{Q}_M \vdots \delta\nabla\mathbf{F}_M = \frac{1}{|\Omega_{UC}|}\int_{\Omega_{UC}} \mathbf{P}_m : \delta\mathbf{F}_m \, \mathrm{d}\Omega, \tag{2.15}$$

with $\mathbf{P}_M$ and $\mathbf{Q}_M$ the macroscopic stress tensor and the higher-order stress tensor, respectively calculated as

$$\mathbf{P}_M = \frac{1}{|\Omega_{UC}|}\int_{\Omega_{UC}} \mathbf{P}_m \, \mathrm{d}\Omega, \tag{2.16}$$

$$\mathbf{Q}_M = \frac{1}{|2\Omega_{UC}|}\int_{\Omega_{UC}} \left(\mathbf{P}_m^T\mathbf{X} + \mathbf{X}\mathbf{P}_m\right) \mathrm{d}\Omega. \tag{2.17}$$

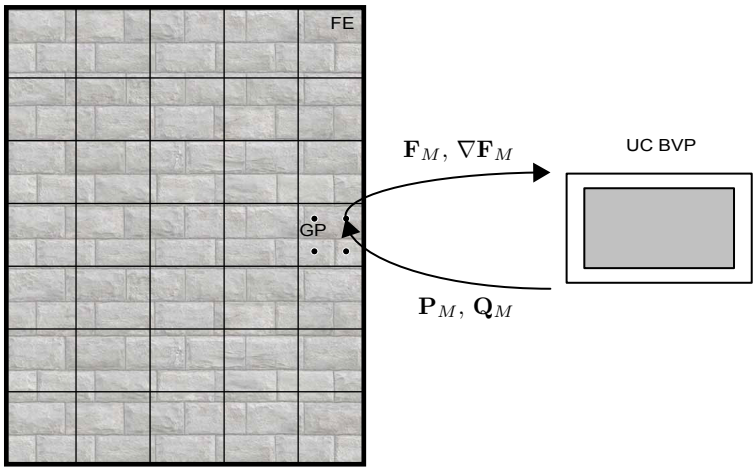

Figure 2.4: Scheme of the second-order CH strategy.

2.3 Selection of the Unit Cell

The question about an appropriate selection of the UC was faced by many authors, several and slightly different definitions of UC have been given.
According to Drugan and Willis [21], the UC has to be a statistically representative sample of the meso-structure. Hence, it has to be chosen in a way that it includes all the possible mechanisms that occur at the local level (see Fig. 2.5). Another definition refers to the UC as the smallest volume that sufficiently accurately represents the overall macroscopic properties of interest [5]. This usually leads to much smaller UC than the statistical one. Hill [35] affirmed that a UC is well-defined if it reflects the material meso-structure and if the responses under uniform displacement and traction boundary condition coincide. Nguyen [65] verified and confirmed the existence of the UC for softening quasi-brittle materials with random microstructure, calculating the homogenized stress and strain as the average of the mesoscopic strain and stress over the damage domain, i.e. the region containing Gauss points which are damaged and loading.
The choice of the UC cannot be performed regardless of the observation of the structural pattern. If we refer to structures composed by a quite regular repetition of UC, different regular patterns can be distinguished. Rectangular patterns are those where the UC is bordered by segments perpendicular to the

ones connecting the centre of the cell and those of the neighboring cells, passing through the mid point of them [49]. Such a tessellation scheme is applicable for stack bond masonry, English bond or 1/2, 1/3 running bond [5]. Hexagonal patterns are those where the periodical repetition of the UC takes place along a not orthogonal frame of reference. For masonry material, this is the case of Dutch bond and Flemish bond [5].

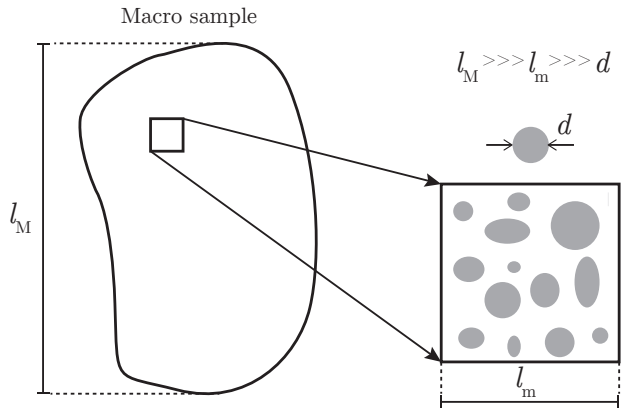

Figure 2.5: Definition of an UC for a statistically homogeneous material.

In a more general framework of heterogeneous materials, specifically the fibre reinforced composites, some efforts in the criteria for selecting an efficient UC were provided by Li [48–50]. The micro-mechanical analysis of such a material can be simplified to a two-dimensional problem in the plane of a cross-section of the composite (see Fig. 2.6). In this plane, assuming a periodic pattern that is a hexagonal layout, Li [48] distinguishes periodical elements and unit cells. The periodic elements are those that cover the whole region by translating in the periodic directions ν_1 and ν_2. He pointed out that all the possible different selections of periodic elements can be unified by choosing the trapezoidal UC that takes advantage of the existing symmetries. Actually, depending on the way of realizing a rotational symmetry of the trapezoidal UC, all the other selections can be reproduced. If the border line of the quarter part of the periodical elements is chosen as the diagonal of the quarter model, triangular UCs T_1 and T_2 are obtained. If the border line of the quarter part is chosen as a line 60° from horizontal direction, the trapezoidal UC Z is reproduced. Lastly, if the border line is horizontal, the UC R is achieved.

It is observed that the strict application of the whole inequality of Fig. 2.5 may lead to a choice of UC not efficient or with a characteristic length bigger than the macro-characteristic length. In this respect, in the following dissertation, only the left term of the inequality of Fig. 2.5 is considered and the UC chosen for the multi-scale analyses represents a compromise between the studies of Li [48] and other authors [21, 27] with the aim of reaching the maximum accuracy with the least computational cost.

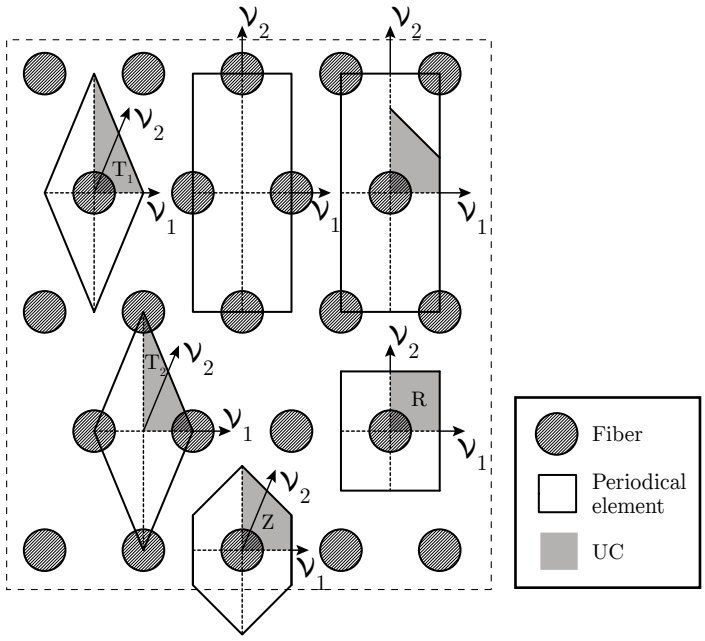

Figure 2.6: Hexagonal fiber-matrix packing with several periodical elements and UCs [48].

2.4 Choice of the scale transition laws

The Hill-Mandel condition (2.2) is satisfied for different boundary conditions. The most commonly used in CH schemes are those in Table 2.1.
Linear and constant tractions boundary conditions are sometimes referred to as homogeneous boundary conditions.
Taylor's assumption, also referred to as isostrain condition, assumes a linear homogeneous mapping of the entire UC domain. Under the Taylor's assump-

tion, the stress equilibrium at the interface between different phases is violated. This configuration furnishes the stiffest possible UC response [78].
Several authors, e.g. Refs. [62, 87, 88], have shown that in pure mechanical linear and nonlinear problems, the effective behavior derived under periodic boundary conditions is bounded by linear displacement boundary conditions from above and constant traction boundary conditions from below. Thus, even for non-periodic heterogeneous materials, periodic BCs provide reasonable estimate of the effective properties. However, this does not imply that the results obtained under periodic boundary conditions are always the closest ones to the exact solutions as clearly stated by Terada et al. [88] *there is no guarantee that periodic boundary conditions are the best among a class of possible boundary conditions. Nonetheless, the periodic boundary conditions provide the reasonable estimates on the effective moduli in the sense that they are always bounded by the other.* Also, it has been claimed by Shen and Brinson [80] that *periodic boundary conditions require the continuity of the inclusions on opposite boundaries to ensure the periodicity of the microstructure. Because such unnatural periodicity is seldom observed in real heterogeneous materials, periodic boundary conditions are not appropriate for finite element models developed by cutting out fragments of actual microstructures or by using simulated microstructures based on actual microstructures.* On the other hand, compared to linear and constant traction BCs, periodic BCs give a faster convergence of the effective properties.

Name	Equation
Taylor BCs	$\mathbf{u}_m = \boldsymbol{\varepsilon}_M \mathbf{x} \quad \text{on}\, \Omega_{\text{UC}}$
Linear BCs	$\mathbf{u}_m = \boldsymbol{\varepsilon}_M \mathbf{x} \quad \text{on}\, \Gamma_{\text{UC}}$
Constant traction BCs	$\mathbf{t}_m = \boldsymbol{\sigma}_M \mathbf{n} \quad \text{on}\, \Gamma_{\text{UC}}$
Periodic BCs	$\mathbf{u}_m^+ = \mathbf{u}_m^- + \boldsymbol{\varepsilon}_M \Delta\mathbf{x} \quad \text{on}\, \Gamma_{\text{UC}}$ $\mathbf{u}_m = \boldsymbol{\varepsilon}_M \mathbf{x} \quad \text{on}\, \mathbf{x} = \bar{\mathbf{x}}$

Table 2.1: Commonly used boundary conditions for UC.

Chapter 3

Mesoscopic level

3.1 Introduction

In a generic computational homogenization (CH) procedure, the crucial point is the definition and the solution of the Unit Cell (UC) Boundary Value Problem (BVP). In the present chapter, some aspects regarding the UC BVP are analyzed considering the masonry material under plane stress condition. The main aspects to be chosen for the formulation of the UC BVP are (i) geometry; (ii) boundary conditions (BCs); (iii) material models; (iv) numerical approximation techniques. All these components play a key-role in the formulation of the problem.
The choice of the UC depends strongly on the geometry of the composite media. In the case of stack bond or running bond masonry patterns, Anthoine [5] states that ? *a "good" basic cell is made up of one brick surrounded by half mortar joint* ?. This UC, characterized by two perpendicular axes of symmetry, was chosen by many authors who have worked in the framework of masonry homogenization, among them Luciano and Sacco [54], Massart [57, 58], Giambanco and co-authors [28, 84] (Fig. 3.1 (a)). In this case, a general masonry pattern is obtained by the periodic repetition of the UC along the skewed directions ν_1 and ν_2:

$$\nu_1 = L\mathbf{e}_1, \qquad \nu_2 = D\mathbf{e}_1 + H\mathbf{e}_2, \tag{3.1}$$

where L is the length of the brick plus the thickness of the head joint, H is the height of the brick plus the thickness of the bed joint and D is the overlapping of the unit cells in two different consecutive courses, that, in the case of

running bond masonry is equal to half of L. Another repetitive cell characterizing the same masonry texture is the not symmetric one represented in Fig. 3.1 (b), used by Luciano and Sacco [54]. Mercatoris et al. [60] selected a parallelogram spanned by the vectors oriented along the periodicity directions (Fig. 3.1 (c)). UCs involving more than one brick are used by Sacco and co-authors [2, 54, 77], De Bellis and Addessi [18] (Fig. 3.1 (d)) or Zucchini and Lourenço [97], Bacigalupo and Gambarotta [6] (Fig. 3.1 (e)). These choices allow to deal with an orthogonal periodicity. Lastly, a UC containing two blocks, two head joints and one bed joint is also a plausible choice [91, 95], even though symmetric BCs have to be used (Fig. 3.1 (f)).

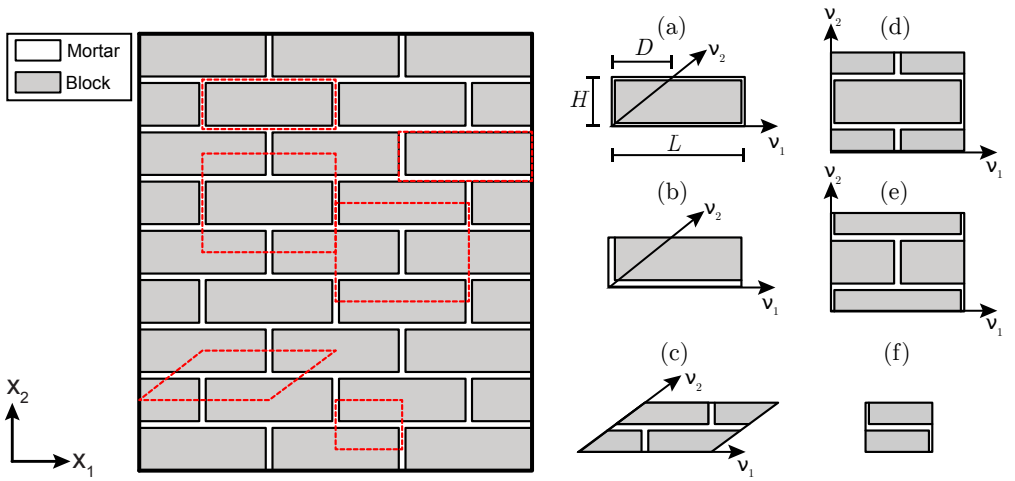

Figure 3.1: Possible UCs extracted from running bond masonry characterized by (a), (b), (c) skewed periodicity [54, 58, 60] and (d), (e) orthogonal periodicity [2, 6, 18, 54, 77, 97] or (f) symmetric properties [91, 95].

As pointed out by Nguyen [67], the choice of the type of BCs to be applied at the mesoscopic level affects the result in terms of macroscopic constitutive response. The most commonly BCs used are (i) Taylor BCs (ii) Linear BCs (iii) Constant traction BCs (iv) Periodic BCs. Many authors agree upon the fact that periodic BCs give a faster convergence of the effective properties, compared to linear and constant traction BCs. It is remarked that the periodic BCs must be applied with discernment, depending on the UC geometry and on the masonry macroscopic patterns.

As concern the constitutive behavior of UC constituents, there is no a universally recognized model for modeling brick and mortar. Periodic homogenization techniques with elastic behavior of both brick and mortar have been advanced by Anthoine [5] and Luciano and Sacco [54]. Quite often, the brick is assumed to behave elastically and nonlinear behavior reside in the mortar joints. Sacco [77] proposed a coupled damage-friction model for the mortar, Spada et al. [85] formulated a elasto-plastic damaging interface model. Models that assume the nonlinear response of both the constituents also exists. Gambarotta and Lagomarsino adopt damage constitutive laws for brick and mortar. Massart et al. [58] proposed nonlocal implicit gradient isotropic damage models for both constituents.
Lastly, as regard the discretization method for the mesoscopic problem, FEM is the dominant one, even though, in principle, any numerical method can be adopted. For the sake of completeness, it is remarked that, in the general framework of heterogeneous material, the boundary element method (BEM) was adopted at the UC level [33] or at both the macroscopic and mesoscopic one, realizing the so-called BE^2 [79].
In the present study, the UC BVP is formulated according to a displacement based variational formulation, where the material of the blocks is considered indefinitely elastic and the mortar joints are simulated by zero-thickness elasto-plastic interfaces (Section 3.2). The choice of adopting an elasto-plastic response of mortar may appear restrictive, however it represents a good compromise between ease of applicability and effective representation of the decohesion process occurring at the joint level.
Both linear and periodic BCs are used to apply the macroscopic strain tensor to the UC (Section 3.3). The numerical discretization is original with respect to the more common FE mesoscopic discretization, it is in fact formulated in the framework of Meshless Methods (Section 3.4). It is well-known that mesh-free methods are particularly suitable in simulations where the material can move around (as in computational fluid dynamics) or where large deformations of the material can occur (as in simulations of plastic materials). In a FE mesh, differently, each point has a fixed number of predefined neighbors and, in problems requiring remeshing, some errors can be introduced. The masonry material modeled at this stage does not require any remeshing and most of times it can be described by UC with a fixed geometry. However, it will be showed that the meshless discretization allows to obtain a considerable computational gain with respect to a standard FE discretization. Moreover, it offers some advantages in the imposition of periodic BCs.

The computational aspects together with the UC numerical response are provided both for linear and periodic BCs, in Sections 3.5 and 3.6, respectively.

3.2 The Unit Cell Boundary Value Problem

Let us consider the UC in Fig. 3.2, constituted by a block having a domain Ω_b surrounded by four interfacial domains Γ_k. Assuming that the body forces can be neglected, the equilibrium of the UC, having the whole boundary constrained, can be assessed in a weak form making use of the constrained principle of virtual displacement (PVD), Eq. (2.6).

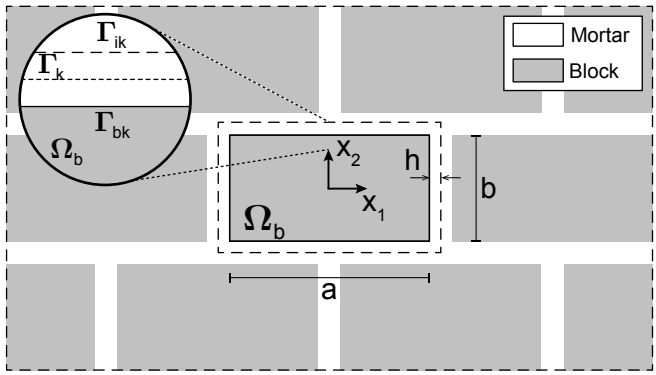

Figure 3.2: UC extracted from running bond masonry.

Indicating with the subscript k and b the mechanical quantities associated to the interfaces and the block, respectively, the following general assumptions are adopted to describe the mechanical behavior of the interfaces:

- the traction components are continuos at the interfaces

$$[\boldsymbol{\sigma}_{mi}] = \mathbf{0}; \tag{3.2}$$

- the strain components along the thickness h of the interface are uniform and evaluated on the basis of the values assumed by the displacement discontinuity components between Γ_{ik} and Γ_{bk} (see close-up view of Fig. 3.2)

$$\boldsymbol{\varepsilon}_{mi} = \frac{[\mathbf{u}_{mi}]}{h}; \tag{3.3}$$

- the total strain and the total displacement discontinuities are decomposed in the elastic (e) and inelastic (p) parts

$$\boldsymbol{\varepsilon}_{mi} = \boldsymbol{\varepsilon}^{e}_{mi} + \boldsymbol{\varepsilon}^{p}_{mi}, \qquad [\mathbf{u}_{mi}] = [\mathbf{u}_{mi}]^{e} + [\mathbf{u}_{mi}]^{p}\,; \tag{3.4}$$

- the density of the internal work can be expressed as

$$L_{mi} = \boldsymbol{\sigma}_{mi} \cdot [\mathbf{u}_{mi}]\,. \tag{3.5}$$

The weak form of the UC equilibrium, Eq. (2.6), taking into account the above reported assumptions, can be rewritten in the following form:

$$\int_{\Omega_b} \boldsymbol{\sigma}_{mb} : \delta\boldsymbol{\varepsilon}_{mb}\,\mathrm{d}\Omega + \\ + \sum_{k=1}^{N_{int}} \int_{\Gamma_k} \left[\boldsymbol{\sigma}_{mi} \cdot \delta\,[\mathbf{u}_{mi}] - \delta\mathbf{r} \cdot (\mathbf{u}_m - \bar{\mathbf{u}}_m) - \mathbf{r} \cdot \delta\mathbf{u}_m\right] \mathrm{d}\Gamma = 0, \tag{3.6}$$

where Γ_k represents the middle surface of the mortar joint surrounding the block, that coincides with the UC boundary Γ_{ik} (Fig. 3.2). In the most general and simplest case, k ranges from 1 to 4, however, since the UC boundaries can be split in any number of interfacial sub-domains, N_{int} indicates the total number of domains on the UC boundary. Applying the divergence theorem at the first term of the equality (3.6):

$$\sum_{k=1}^{N_{int}} \int_{\Gamma_{bk}} \boldsymbol{\sigma}_{mb}\,\mathbf{n}_k \cdot \delta\mathbf{u}_m\,\mathrm{d}\Gamma - \int_{\Omega_b} \mathrm{div}\boldsymbol{\sigma}_{mb} \cdot \delta\mathbf{u}_m\,\mathrm{d}\Omega + \\ + \sum_{k=1}^{N_{int}} \int_{\Gamma_k} \left[\boldsymbol{\sigma}_{mi} \cdot \delta\,[\mathbf{u}_{mi}] - \delta\mathbf{r} \cdot (\mathbf{u}_m - \bar{\mathbf{u}}_m) - \mathbf{r} \cdot \delta\mathbf{u}_m\right] \mathrm{d}\Gamma = 0, \tag{3.7}$$

where Γ_{bk} indicates the block-mortar joints contact surfaces (close-up view of Fig. 3.2). Considering that the interface stresses are constant along the thickness and the displacement discontinuities are calculated as the difference between the displacements evaluated at the interface middle plane Γ_k and the displacements of the joint-block contact surface Γ_{bk}, the terms of the equality (3.7) can be collected in the following way

$$\sum_{k=1}^{N_{int}} \int_{\Gamma_{bk}} (\boldsymbol{\sigma}_{mb}\,\mathbf{n}_k - \boldsymbol{\sigma}_{mi}) \cdot \delta\mathbf{u}_m \,\mathrm{d}\Gamma - \int_{\Omega_b} \mathrm{div}\boldsymbol{\sigma}_{mb} \cdot \delta\mathbf{u}_m \,\mathrm{d}\Omega + \\ + \sum_{k=1}^{N_{int}} \int_{\Gamma_k} \left[(\boldsymbol{\sigma}_{mi} - \mathbf{r}) \cdot \delta\mathbf{u}_m - \delta\mathbf{r} \cdot (\mathbf{u}_m - \bar{\mathbf{u}}_m)\right] \mathrm{d}\Gamma = 0. \quad (3.8)$$

The previous equality (3.8) has to hold for any values of the virtual displacements and of the Lagrangian multipliers. Therefore the equilibrium equations of the block, the block-joint contact stress relations and the boundary conditions of the UC are obtained:

$$\mathrm{div}\boldsymbol{\sigma}_{mb} = \mathbf{0} \qquad \mathrm{on}\,\Omega_\mathrm{b} \quad (3.9)$$

$$\boldsymbol{\sigma}_{mb}\,\mathbf{n}_k = \boldsymbol{\sigma}_{mi} \qquad \mathrm{on}\,\Gamma_\mathrm{bk} \quad \mathrm{k} = 1, .., \mathrm{N_{int}} \quad (3.10)$$

$$\boldsymbol{\sigma}_{mi} = \mathbf{r} \qquad \mathrm{on}\,\Gamma_\mathrm{k} \quad \mathrm{k} = 1, .., \mathrm{N_{int}} \quad (3.11)$$

$$\mathbf{u}_m = \bar{\mathbf{u}}_m \qquad \mathrm{on}\,\Gamma_\mathrm{k} \quad \mathrm{k} = 1, .., \mathrm{N_{int}}. \quad (3.12)$$

In order to complete the mechanical problem, the constitutive equations for the block material and for the interfaces have to be introduced. With reference to the assumed hypotheses, the material of the block is considered elastic and inelastic displacement discontinuities arise at the ZTIs, thus

$$\boldsymbol{\sigma}_{mb} = \mathbf{E}_b\,\boldsymbol{\varepsilon}_{mb}, \quad (3.13)$$

$$\boldsymbol{\sigma}_{mi} = \mathbf{E}_i\left([\mathbf{u}_{mi}] - [\mathbf{u}_{mi}]^p\right), \quad (3.14)$$

where $\mathbf{E}_b$ and $\mathbf{E}_i$ are the elastic stiffness matrices of the block material and of the ZTIs, respectively. Irreversible discontinuous displacements occur when

the interface stress state reaches a limit condition.
The elastic domain is defined by two convex limit surfaces intersecting in a non-smooth fashion: the Coulomb bilinear limit surface and a tension cut-off. The limit functions, reported in the stress space, take the following form:

$$\Phi^{p1}(\boldsymbol{\sigma}_{mi}, \chi^p) = |\boldsymbol{\tau}_{mi}| + \sigma_{mi} \tan\phi - c_0(1 - \chi^p), \tag{3.15}$$

$$\Phi^{p2}(\boldsymbol{\sigma}_{mi}, \chi^p) = \sigma_{mi} - \sigma_0(1 - \chi^p), \tag{3.16}$$

where $\boldsymbol{\tau}_{mi}$ and σ_{mi} are the tangential stress vector and the normal stress component of the contact stresses, ϕ is the friction angle, c_0 and σ_0 the cohesion and tensile strength of the virgin interfaces. χ^p is a static variable which is associated to the internal variable ξ^p which regulates the isotropic hardening-softening interface behavior:

$$\chi^p = h^p \xi^p, \tag{3.17}$$

with h^p the hardening-softening parameter.
The two yield functions are depicted in Fig. 3.3. The following four zones can be distinguished:

1. elastic zone, $\Phi^{p1} < 0 \quad \Phi^{p2} < 0$;
2. plastic activation in shear, $\Phi^{p1} = 0 \quad \Phi^{p2} < 0$;
3. plastic activation in tension, $\Phi^{p1} < 0 \quad \Phi^{p2} = 0$;
4. plastic activation in tension and shear (corner), $\Phi^{p1} = 0 \quad \Phi^{p2} = 0$.

The inelastic displacement discontinuities develop according to a non-associative flow rule expressed by the well known Koiter's form [45]:

$$[\dot{\mathbf{u}}_{mi}]^p = \dot{\lambda}^{p1} \frac{\partial G^p}{\partial \boldsymbol{\sigma}_{mi}} + \dot{\lambda}^{p2} \frac{\partial \Phi^{p2}}{\partial \boldsymbol{\sigma}_{mi}}, \quad \dot{\xi}^p = -\dot{\lambda}^{p1} \frac{\partial \Phi^{p1}}{\partial \chi^p} - \dot{\lambda}^{p2} \frac{\partial \Phi^{p2}}{\partial \chi^p}, \tag{3.18}$$

where $\dot{\lambda}^{p1}$, $\dot{\lambda}^{p2}$ are the plastic multipliers which satisfy the following complementarity conditions:

$$\Phi^{p1} \leq 0, \quad \dot{\lambda}^{p1} \geq 0, \quad \Phi^{p1}\dot{\lambda}^{p1} = 0; \tag{3.19}$$

$$\Phi^{p2} \leq 0, \quad \dot{\lambda}^{p2} \geq 0, \quad \Phi^{p2}\dot{\lambda}^{p2} = 0. \tag{3.20}$$

Equations (3.19) and (3.20) describe all the loading/unloading or Kuhn and Tucker conditions. The plastic potential related to the limit condition (3.15) is expressed by the following function:

$$G^p(\boldsymbol{\sigma}_{mi}, \chi^p) = |\boldsymbol{\tau}_{mi}| + \sigma_{mi}(1 - \chi^p)\tan\delta - r, \tag{3.21}$$

with $\delta \in [0, \phi]$ dilatancy angle and r an arbitrary material constant. From the above reported expression it appears that $\tan\delta$ is the initial dilatancy coefficient and it decreases along the loss of cohesion process according to the experimental observations.

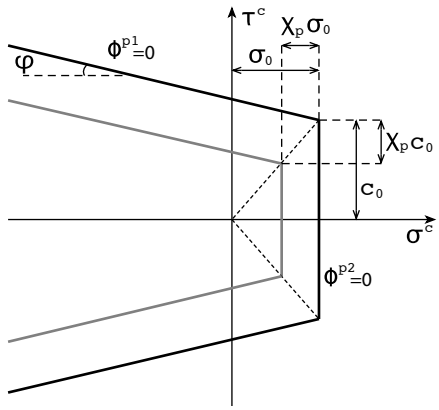

Figure 3.3: Bilinear plastic limit condition represented in the plane stress space.

3.3 Boundary conditions for the UC

In Section 2.2.1 the BVP is generally formulated considering linear BCs (2.3). In literature, the periodic boundary conditions are also suggested for non periodic materials, since they conduct to better estimate the effective properties

of the heterogeneous material [88, 89]. Periodic conditions imposed to the UC imply that an eventual developing of plasticity at a UC should repeat in the near cells, while the real structure localizes degradation in precise narrow zones.

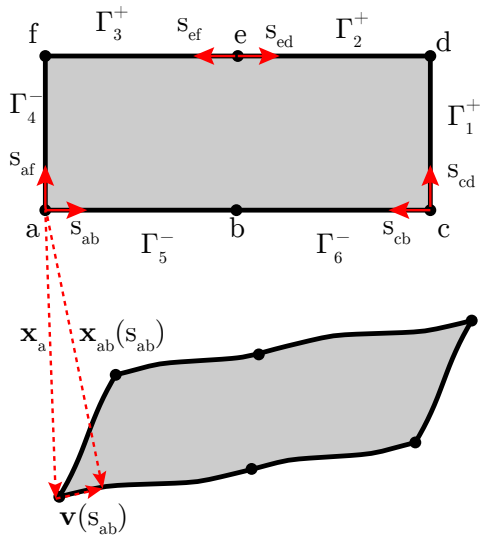

Figure 3.4: Periodic BCs imply identical shape on the coupled boundaries of the UC [83].

With reference to Fig. 3.4, assuming for the case of running bond masonry $\left(D = \frac{L}{2}\right)$, the UC boundary is divided into two parts such as $\Gamma_{\mathrm{UC}} = \Gamma_{\mathrm{UC}}^+ \cup \Gamma_{\mathrm{UC}}^-$, where three pairs of periodic boundaries can be distinguished:

$$\Gamma_1^+ \rightleftarrows \Gamma_4^-, \qquad \Gamma_2^+ \rightleftarrows \Gamma_5^-, \qquad \Gamma_3^+ \rightleftarrows \Gamma_6^-. \tag{3.22}$$

For each boundary of the unit cell we can introduce the shape vector [83] defined as

$$\mathbf{v}\left(s_{ij}\right) = \mathbf{x}_{ij}\left(s_{ij}\right) - \mathbf{x}_i \tag{3.23}$$

where $\mathbf{x}_{ij}\left(s_{ij}\right)$ is the position vector of a material point located on the boundary, with local coordinate s_{ij} and $\mathbf{x}_i$ is position of the initial vertex of the same boundary.

Enforcing the kinematical compatibility condition (3.22), i.e. identical shape for each pair of opposite sides, the following equations are obtained:

$$\mathbf{v}\left(s_{ab}\right) = \mathbf{v}\left(s_{ed}\right) \quad \rightarrow \quad \mathbf{x}_{ed}\left(s_{ed}\right) = \mathbf{x}_{ab}\left(s_{ab}\right) + \mathbf{x}_e - \mathbf{x}_a, \tag{3.24}$$

$$\mathbf{v}\left(s_{cb}\right) = \mathbf{v}\left(s_{ef}\right) \quad \rightarrow \quad \mathbf{x}_{ef}\left(s_{ef}\right) = \mathbf{x}_{cb}\left(s_{cb}\right) + \mathbf{x}_e - \mathbf{x}_c, \tag{3.25}$$

$$\mathbf{v}\left(s_{af}\right) = \mathbf{v}\left(s_{cd}\right) \quad \rightarrow \quad \mathbf{x}_{cd}\left(s_{cd}\right) = \mathbf{x}_{af}\left(s_{af}\right) + \mathbf{x}_c - \mathbf{x}_a. \tag{3.26}$$

On the basis of the previous kinematical compatibility conditions, the volume averaged deformation gradient of the unit cell $\bar{\mathbf{F}}_m$, for the two-dimensional case, can be written as

$$\bar{\mathbf{F}}_m = \frac{1}{A}\int_A \mathbf{F}\,\mathrm{d}A = \frac{1}{A}\int_A \nabla\mathbf{x}\,\mathrm{d}A, \tag{3.27}$$

where A is the area of the UC in the undeformed configuration. Making use of the divergence theorem, the average deformation gradient can be rewritten as a linear integral along the interfaces:

$$\bar{\mathbf{F}}_m = \frac{1}{A}\int_{\Gamma_{UC}} \mathbf{x}\otimes\mathbf{n}\,\mathrm{d}\Gamma \tag{3.28}$$

which, after some mathematical manipulations, becomes

$$\bar{\mathbf{F}}_m = \frac{1}{A}\left[\int_a^b \left(\mathbf{x}_a - \mathbf{x}_e\right)\otimes\mathbf{n}_{ab}\,\mathrm{d}s + \int_c^b \left(\mathbf{x}_c - \mathbf{x}_e\right)\otimes\mathbf{n}_{cb}\,\mathrm{d}s + \right.$$

$$\left. + \int_a^f \left(\mathbf{x}_a - \mathbf{x}_c\right)\otimes\mathbf{n}_{af}\,\mathrm{d}s\right]. \tag{3.29}$$

From Eq. (3.29), it is clear that the measure of the average deformation of the UC can be obtained on the basis of the positions of three vertices of the

cell a, c, e or equally, b, d, f.
The compatibility conditions (3.24-3.26) expressed in terms of displacement are:

$$\mathbf{u}_{ed}\left(s_{ed}\right) = \mathbf{u}_{ab}\left(s_{ab}\right) + \mathbf{u}_{e} - \mathbf{u}_{a}, \tag{3.30}$$

$$\mathbf{u}_{ef}\left(s_{ef}\right) = \mathbf{u}_{cb}\left(s_{cb}\right) + \mathbf{u}_{e} - \mathbf{u}_{c}, \tag{3.31}$$

$$\mathbf{u}_{cd}\left(s_{cd}\right) = \mathbf{u}_{af}\left(s_{af}\right) + \mathbf{u}_{c} - \mathbf{u}_{a}. \tag{3.32}$$

The displacement of the vertices a, c, e can be calculated through the expression (**??**), hence the equations (3.30-3.32) lead to a sort of non-homogenous master-slave constraint relations between two opposite sides of the UC:

$$\mathbf{u}_{ed}\left(s_{ed}\right) = \mathbf{u}_{ab}\left(s_{ab}\right) + \boldsymbol{\varepsilon}_{M}\left(\mathbf{x}_{e} - \mathbf{x}_{a}\right), \tag{3.33}$$

$$\mathbf{u}_{ef}\left(s_{ef}\right) = \mathbf{u}_{cb}\left(s_{cb}\right) + \boldsymbol{\varepsilon}_{M}\left(\mathbf{x}_{e} - \mathbf{x}_{c}\right), \tag{3.34}$$

$$\mathbf{u}_{cd}\left(s_{cd}\right) = \mathbf{u}_{af}\left(s_{af}\right) + \boldsymbol{\varepsilon}_{M}\left(\mathbf{x}_{c} - \mathbf{x}_{a}\right), \tag{3.35}$$

that can be reassumed into a more compacted form as:

$$\mathbf{u}_{m}^{+} = \mathbf{u}_{m}^{-} + \boldsymbol{\varepsilon}_{M}\Delta\mathbf{x}, \qquad \text{on}\,\Gamma_{\text{UC}} \tag{3.36}$$

where $\mathbf{u}_{m}^{+}$ and $\mathbf{u}_{m}^{-}$ are the displacements on Γ_{UC}^{+} and Γ_{UC}^{-}, respectively, and $\Delta\mathbf{x}$ the increments of coordinates from a point on Γ_{UC}^{-} and its corresponding periodic point on Γ_{UC}^{+}.
The correct imposition of Eqs. (3.33÷3.35) guarantees the uniqueness of the solution up to rigid body translations, in fact rigid body rotations are eliminated as (3.33÷3.35) are imposed (see Appendix B) [51]. Hence, to ensure no rigid

body motion, the two translations have to be enforced at least at one point of the UC boundary:

$$\mathbf{u}_m = \bar{\mathbf{u}}_m, \qquad \text{on } \mathbf{x} = \bar{\mathbf{x}}\,. \tag{3.37}$$

In a displacement-based variational formulation, Eqs. (3.36) and (3.37) are essential BCs and, as such, should be explicitly imposed into Eq. (**??**):

$$\begin{aligned}\sum_{k=1}^{N_{int}} \int_{\Gamma_{bk}} \boldsymbol{\sigma}_{mb}\,\mathbf{n}_k \cdot \delta\mathbf{u}_m \,\mathrm{d}\Gamma - \int_{\Omega_b} \mathrm{div}\boldsymbol{\sigma}_{mb} \cdot \delta\mathbf{u}_m \,\mathrm{d}\Omega + \sum_{k=1}^{N_{int}} \int_{\Gamma_k} \boldsymbol{\sigma}_{mi} \cdot \delta\left[\mathbf{u}_{mi}\right] \mathrm{d}\Gamma \\ + \sum_{k\in k^+} \int_{\Gamma_k^+} \left[\boldsymbol{\lambda} \cdot \left(\delta\mathbf{u}_m^+ - \delta\mathbf{u}_m^-\right) + \delta\boldsymbol{\lambda} \cdot \left(\mathbf{u}_m^+ - \mathbf{u}_m^- - \boldsymbol{\varepsilon}_M \Delta\mathbf{x}\right)\right] \mathrm{d}\Gamma + \\ - \delta\mathbf{R} \cdot (\mathbf{u}_m - \bar{\mathbf{u}}_m) - \mathbf{R} \cdot \delta\mathbf{u}_m = 0.\end{aligned} \tag{3.38}$$

In Eq. (3.38), similarly to Eq. (3.6), the first three integrals represent the virtual internal work evaluated on the block domain Ω_b and interfaces domains Γ_k, respectively. The periodic BCs are imposed on half of the UC boundary through the Lagrange multipliers $\boldsymbol{\lambda}$. Lastly, $\mathbf{R}$ is the Lagrange multiplier coincident with the reaction force in $\mathbf{x} = \bar{\mathbf{x}}$.
By making explicit the displacement discontinuities $[\mathbf{u}_{mi}]$ as the difference between the displacements evaluated at the interface middle plane Γ_k and the displacements of the joint-block contact surface Γ_{bk}, and considering $\Gamma^+ = \Gamma^-$, the terms of the equality (3.38) can be collected in the following way

$$\begin{aligned}\sum_{k=1}^{N_{int}} \int_{\Gamma_{bk}} (\boldsymbol{\sigma}_{mb}\,\mathbf{n}_k - \boldsymbol{\sigma}_{mi}) \cdot \delta\mathbf{u}_m \,\mathrm{d}\Gamma - \int_{\Omega_b} \mathrm{div}\boldsymbol{\sigma}_{mb} \cdot \delta\mathbf{u}_m \,\mathrm{d}\Omega + \\ + \sum_{k\in k^+} \int_{\Gamma_k^+} (\boldsymbol{\sigma}_{mi} + \boldsymbol{\lambda}) \cdot \delta\mathbf{u}_m^+ \mathrm{d}\Gamma + \sum_{k\in k^-} \int_{\Gamma_k^-} (\boldsymbol{\sigma}_{mi} - \boldsymbol{\lambda}) \cdot \delta\mathbf{u}_m^- \mathrm{d}\Gamma + \\ \sum_{k\in k^+} \int_{\Gamma_k^+} \delta\boldsymbol{\lambda} \cdot \left(\mathbf{u}_m^+ - \mathbf{u}_m^- - \boldsymbol{\varepsilon}_M \Delta\mathbf{x}\right) \mathrm{d}\Gamma - \delta\mathbf{R} \cdot (\mathbf{u}_m - \bar{\mathbf{u}}_m) - \mathbf{R} \cdot \delta\mathbf{u}_m = 0.\end{aligned} \tag{3.39}$$

The previous equality (3.39) has to hold for any values of the virtual displacements and of the Lagrangian multipliers, hence

$$\mathrm{div}\boldsymbol{\sigma}_{mb} = \mathbf{0} \qquad \mathrm{on}\,\Omega_{\mathrm{b}} \tag{3.40}$$

$$\boldsymbol{\sigma}_{mb}\,\mathbf{n}_k = \boldsymbol{\sigma}_{mi} \qquad \mathrm{on}\,\Gamma_{\mathrm{bk}} \quad \mathrm{k} = 1, .., \mathrm{N_{int}} \tag{3.41}$$

$$\boldsymbol{\sigma}_{mi} = -\boldsymbol{\lambda} \qquad \mathrm{on}\,\Gamma_{\mathrm{k}}^{+} \quad \mathrm{k} = 1, .., \mathrm{N_{int}}/2 \tag{3.42}$$

$$\boldsymbol{\sigma}_{mi} = \boldsymbol{\lambda} \qquad \mathrm{on}\,\Gamma_{\mathrm{k}}^{-} \quad \mathrm{k} = \frac{\mathrm{N_{int}}}{2} + 1, .., \mathrm{N_{int}} \tag{3.43}$$

$$\mathbf{u}_m^{+} = \mathbf{u}_m^{-} + \boldsymbol{\varepsilon}_M \Delta\mathbf{x} \qquad \mathrm{on}\,\Gamma_{\mathrm{k}}^{+} \quad \mathrm{k} = 1, .., \mathrm{N_{int}}/2 \tag{3.44}$$

$$\mathbf{u}_m = \bar{\mathbf{u}}_m \qquad \mathrm{on}\,\mathbf{x} = \bar{\mathbf{x}} \tag{3.45}$$

$$\mathbf{R} = \mathbf{0} \qquad \mathrm{on}\,\mathbf{x} = \bar{\mathbf{x}} \tag{3.46}$$

where Eqs. (3.40) and (3.41) represent the equilibrium of the block and the block-joint contact stress relations, Eqs. (3.42) and (3.43) represent the anti-periodicity of the traction field on the UC boundary, Eqs. (3.44÷3.46) give back the boundary conditions and the equilibrium of the reaction forces that constrain translational motions. Particular attention is laid on the fact that the traction BCs (3.42 and 3.43), namely the fact that the tractions are opposite on corresponding sides of the UC, result as natural BCs, hence an additional enforcement is neither necessary nor correct [51].

3.4 Meshless solutions

In the CH, the macroscopic constitutive behavior of the material is carried out during the simulation on the basis of the mechanical phenomena occurring at the UC level. Generally the solution of the UC BVP is approached in an approximated way making use of the finite element method and, since two finite element meshes are used at the macroscopic and mesoscopic levels, the method is known as FE^2.
The present study approaches the numerical solution of the mesoscopic model by means of a meshless strategy which is described in the present section for a plane stress condition.
Similarly to the FEM, the displacement field is obtained from the nodal displacement values $\mathbf{U}_m$ but the *Moving Least Square* approximation (MLS) is used. Making use of matrix algebra notation, the approximated value of a displacement component is expressed as a polynomial function:

$$u_m^h(\mathbf{x}) = \mathbf{p}^T(\mathbf{x})\,\mathbf{a}(\mathbf{x}) \tag{3.47}$$

with $\mathbf{p}(\mathbf{x})$ a monomial basis function and $\mathbf{a}(\mathbf{x})$ the vector of coefficients which are functions of the spatial coordinates $\mathbf{x}$. In the present case the simplest basis function adopted is linear, $\mathbf{p}^T(\mathbf{x}) = [1 \quad x_1 \quad x_2]$, and the coefficients are obtained by performing the minimization of the following functional:

$$J(\mathbf{x}) = \sum_{j=1}^{N} w_j(\mathbf{x}) \left[u_m^h(\mathbf{x}_j) - U_{mj}\right]^2, \tag{3.48}$$

where N is the number of nodes and $w_j(\mathbf{x}) = w_j(\mathbf{x} - \mathbf{x}_j)$ is the weight function depending on the distance between the sampling point and the node j. Minimizing functional (3.48) results in a system of linear equations

$$\mathbf{a}(\mathbf{x}) = \mathbf{A}^{-1}(\mathbf{x})\ \mathbf{B}(\mathbf{x})\ \mathbf{U}_m, \tag{3.49}$$

where

$$\mathbf{A}(\mathbf{x}) = \sum_{j=1}^{N} w_j(\mathbf{x})\,\mathbf{p}(\mathbf{x})\,\mathbf{p}^T(\mathbf{x}), \tag{3.50}$$

$$\mathbf{B}(\mathbf{x}) = [w_1(\mathbf{x})\ \mathbf{p}(\mathbf{x}_1),\ w_2(\mathbf{x})\ \mathbf{p}(\mathbf{x}_2),\ \ldots,\ w_N(\mathbf{x})\ \mathbf{p}(\mathbf{x}_N)], \tag{3.51}$$

$$\mathbf{U}_m = [\mathbf{U}_{m1}\ \mathbf{U}_{m2}\ \ldots\ \mathbf{U}_{mN}]^T. \tag{3.52}$$

Substituting the result (3.49) into (3.47) the MLS approximation function is finally obtained as

$$u_m^h(\mathbf{x}) = \boldsymbol{\phi}^T(\mathbf{x})\,\mathbf{U}_m \tag{3.53}$$

where the shape function $\boldsymbol{\phi}^T(\mathbf{x})$ is given by

$$\boldsymbol{\phi}^T(\mathbf{x}) = \mathbf{p}^T(\mathbf{x})\,\mathbf{A}^{-1}(\mathbf{x})\,\mathbf{B}(\mathbf{x}). \tag{3.54}$$

Considering a 1D element divided in two parts as the ZTI domain, the shape functions of all three nodes are plotted in Fig. 3.5. These shape functions are obtained using a fourth-order spline as weight function

$$w_j(\mathbf{x}) = \begin{cases} 1 - 6\,r_j^2 + 8\,r_j^3 - 3\,r_j^4, & \text{for} \quad 0 \le r_j \le 1 \\ 0, & \text{for} \quad r_j \ge 1 \end{cases} \tag{3.55}$$

with $r_j = \|\mathbf{x} - \mathbf{x_j}\|/d$, being d the radius of the domain of definition of the point $\mathbf{x}$ equal to l, the length of the domain. This results in rational functions with polynomial functions of the $9th$ and $8th$ order on the numerator and denominator, respectively. It is visible that, in general, the shape functions do not satisfy Kronecker delta properties at nodal points.

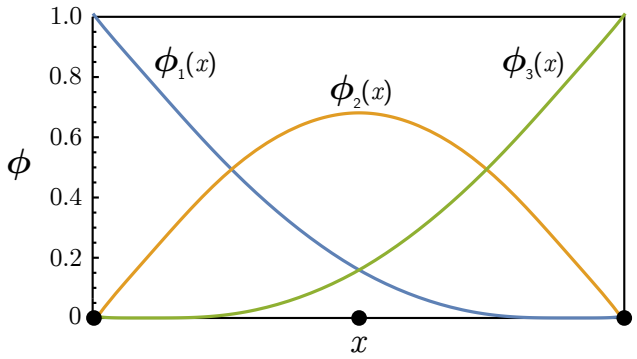

Figure 3.5: Meshless shape functions of a 1D domain with three nodes discretization and radius d of the weight function equal to the length of the domain.

The property of approximation is strictly dependent on the choice of the radius d that governs the domain of influence of the weight function associated with the I*th* node. In particular, the domain of influence should be (i) large enough to provide a sufficient number of neighbors to ensure the invertibility of matrix **A**, (ii) small enough to provide adequate local character to the least-square approximation, (iii) not to large for the sake of computational cost [15].

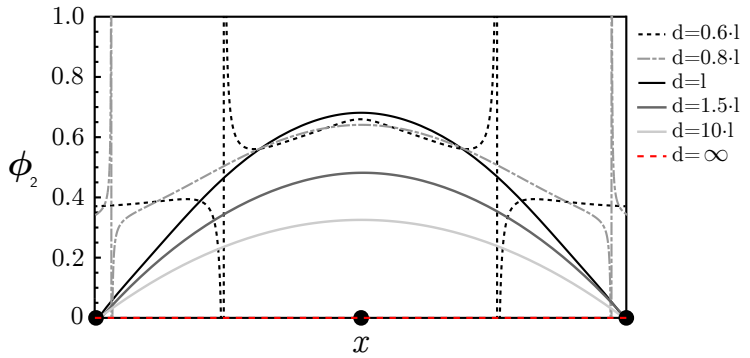

Figure 3.6: Influence of the radius d of the support of the Ith node on the shape function ϕ_2 (l indicates the length of the 1D domain).

In Fig. 3.6, the shape function $\phi_2(x)$ is showed for different sizes of the domain of influence. It is observed that, on the one hand, too small values of d imply a not continuous shape function, on the other hand too high values of d negatively affect the approximation property of the function. The most

reasonable size is coincident with the one including the all nodes of the domain, i.e. $d = l$.
The approximation character of the meshless shape functions is also visible in Fig. 3.7 where the peculiar shape functions of the block are plotted considering a rectangular domain with dimensions 220×50 mm.

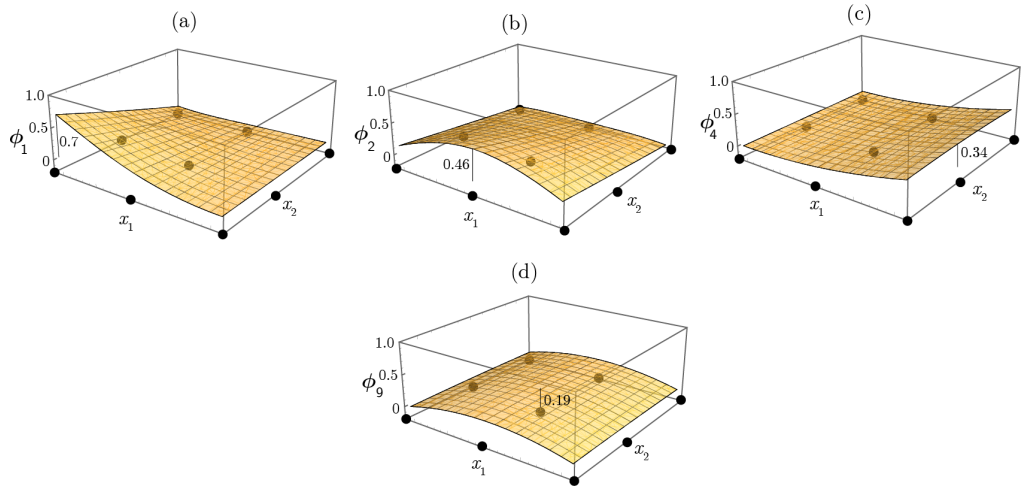

Figure 3.7: Meshless shape functions of a 2D domain with nine nodes discretization and radius d of the weight function equal to the diagonal of the rectangular domain. With reference to the nodes indicated in Fig. 3.8: (a) $\phi_1(x_1, x_2)$ symmetric with respect to $\phi_3(x_1, x_2), \phi_5(x_1, x_2), \phi_7(x_1, x_2)$ (b) $\phi_2(x_1, x_2)$ symmetric with respect to $\phi_6(x_1, x_2)$ (c) $\phi_4(x_1, x_2)$ symmetric with respect to $\phi_8(x_1, x_2)$, (d) $\phi_9(x_1, x_2)$

3.4.1 Linear BCs

With reference to Fig. 3.8, the UC is divided in five integration domains: the first Ω_b corresponds to the volume occupied by the block. To this domain nine nodes are associated, each one with two degrees of freedom consisting in the displacements along the two directions of the reference axes (x_1, x_2). The other integration domains are the interfaces Γ_k $(k = 1, 2, 3, 4)$, each one defined by six nodes, among which three are in common with the block and the others are located on the boundary of the UC. Totally seventeen nodes are used to discretize the UC. This discretization has to be considered as the minimum one, i.e. the sparsest one to get a reasonable UC mechanical response. Different

choices are obviously possible in order to refine the numerical solution.

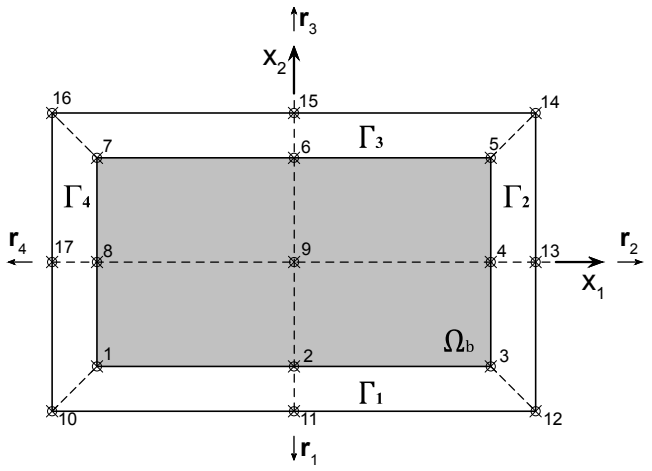

Figure 3.8: UC Meshless model for linear BCs.

Making use of the MLS approximations for the two components of the displacement field in each subdomain, the kinematical compatibility conditions for the block and for the interfaces are

$$\varepsilon_{mb} = \mathbf{C}\,\mathbf{\Phi}_b\mathbf{S}_b\mathbf{U}_m, \qquad [\mathbf{u}_{mi}] = \mathbf{T}(\mathbf{\Phi}_k\mathbf{S}_k - \mathbf{\Phi}_b\mathbf{S}_b)\,\mathbf{U}_m \tag{3.56}$$

where the $\mathbf{\Phi}_b$ and $\mathbf{\Phi}_k$ are the approximation functions, $\mathbf{S}_b$ and $\mathbf{S}_k$ are the selectivity matrices, evaluated for the block and for the interface domains, respectively. $\mathbf{C}$ is the classical compatibility matrix for the plane stress case:

$$\mathbf{C} = \begin{bmatrix} \partial/\partial x_1 & 0 \\ 0 & \partial/\partial x_2 \\ \partial/\partial x_2 & \partial/\partial x_1 \end{bmatrix} \tag{3.57}$$

while $\mathbf{T}$ is the rotation matrix

$$\mathbf{T} = \begin{bmatrix} \cos\alpha & \sin\alpha \\ -\sin\alpha & \cos\alpha \end{bmatrix} \tag{3.58}$$

used to relate quantities written according to the local or global reference systems.
The reaction forces on the boundaries Γ_k are also approximated in terms of nodal values $\mathbf{R}$ as

$$\mathbf{r} = \mathbf{\Psi}\left(\mathbf{x}\right) \bar{\mathbf{S}}_k \mathbf{R} \tag{3.59}$$

where $\mathbf{\Psi}\left(\mathbf{x}\right)$ are the approximation functions for the reaction forces, and $\bar{\mathbf{S}}_k$ the selectivity matrix for the reaction forces of the interfaces.
Considering the kinematical Eq. (3.56), the approximation (3.59) and the elastic constitutive laws for the block (3.13) and for the mortar joints (3.63), the weak form of the UC equilibrium (3.7) can be particularized in the following equation:

$$\begin{aligned}
&\delta\mathbf{U}_m^T \left\{ \left[\int_{\Omega_b} \mathbf{S}_b^T \mathbf{\Phi}_b^T \mathbf{C}^T \mathbf{E}_b \mathbf{C} \mathbf{\Phi}_b \mathbf{S}_b \, d\Omega + \right.\right. \\
&\left. + \sum_{k=1}^{4} \int_{\Gamma_k} \left(\mathbf{\Phi}_k \mathbf{S}_k - \mathbf{\Phi}_b \mathbf{S}_b\right)^T \mathbf{T}_k^T \mathbf{E}_i \, \mathbf{T}_k \left(\mathbf{\Phi}_k \mathbf{S}_k - \mathbf{\Phi}_b \mathbf{S}_b\right) d\Gamma \right] \mathbf{U}_m + \\
&\left. - \sum_{k=1}^{4} \int_{\Gamma_k} \left(\mathbf{\Phi}_k \mathbf{S}_k - \mathbf{\Phi}_b \mathbf{S}_b\right)^T \mathbf{T}_k^T \mathbf{E}_i \, \left[\mathbf{u}_{mi}\right]^p d\Gamma - \sum_{k=1}^{4} \int_{\Gamma_k} \mathbf{S}_k^T \mathbf{\Phi}_k^T \mathbf{\Psi}_k \bar{\mathbf{S}}_k \mathbf{R} d\Gamma \right\} + \\
&- \sum_{k=1}^{4} \int_{\Gamma_k} \delta\mathbf{R}^T \bar{\mathbf{S}}_k^T \mathbf{\Psi}_k^T \left(\mathbf{\Phi}_k \mathbf{S}_k \mathbf{U}_m - \bar{\mathbf{u}}_m\right) d\Gamma = 0.
\end{aligned} \tag{3.60}$$

Making the following positions

$$\mathbf{K}_b = \int_{\Omega_b} \mathbf{S}_b^T \mathbf{\Phi}_b^T \mathbf{C}^T \mathbf{E}_b \mathbf{C} \mathbf{\Phi}_b \mathbf{S}_b \mathrm{d}\Omega, \tag{3.61}$$

$$\mathbf{K}_i = \sum_{k=1}^{4} \int_{\Gamma_k} \left(\mathbf{\Phi}_k \mathbf{S}_k - \mathbf{\Phi}_b \mathbf{S}_b\right)^T \mathbf{T}_k^T \mathbf{E}_i \, \mathbf{T}_k \left(\mathbf{\Phi}_k \mathbf{S}_k - \mathbf{\Phi}_b \mathbf{S}_b\right) d\Gamma, \tag{3.62}$$

$$\mathbf{K} = \mathbf{K}_b + \mathbf{K}_i, \tag{3.63}$$

$$\mathbf{G} = \sum_{k=1}^{4} \int_{\Gamma_k} \mathbf{S}_k^T \boldsymbol{\Phi}_k^T \boldsymbol{\Psi}_k \bar{\mathbf{S}}_k d\Gamma, \tag{3.64}$$

$$\mathbf{F}_p = \sum_{k=1}^{4} \int_{\Gamma_k} \left(\boldsymbol{\Phi}_k \mathbf{S}_k - \boldsymbol{\Phi}_b \mathbf{S}_b\right)^T \mathbf{T}_k^T \mathbf{E}_k \, [\mathbf{u}_{mi}]^p \, d\Gamma, \tag{3.65}$$

$$\bar{\mathbf{U}}_m = \sum_{k=1}^{4} \int_{\Gamma_k} \bar{\mathbf{S}}_k^T \boldsymbol{\Psi}_k^T \bar{\mathbf{u}}_m d\Gamma, \tag{3.66}$$

Eq. (3.60) becomes

$$\delta \mathbf{U}_m^T \left(\mathbf{K}\mathbf{U}_m - \mathbf{G}\mathbf{R} - \mathbf{F}_p\right) - \delta \mathbf{R}^T \left(\mathbf{G}^T \mathbf{U}_m - \bar{\mathbf{U}}_m\right) = 0. \tag{3.67}$$

Since Eq. (3.67) has to hold for any arbitrary $\delta\mathbf{U}_m$ and $\delta\mathbf{R}$, the governing equations of the UC are thus obtained:

$$\begin{bmatrix} \mathbf{K} & -\mathbf{G} \\ \mathbf{G}^T & \mathbf{0} \end{bmatrix} \begin{bmatrix} \mathbf{U}_m \\ \mathbf{R} \end{bmatrix} = \begin{bmatrix} \mathbf{F}_p \\ \bar{\mathbf{U}}_m \end{bmatrix}. \tag{3.68}$$

In order to evaluate the integrals (3.61) and (3.62), and (3.64)÷(3.66), the Gauss quadrature rule is adopted. Furthermore, it is assumed $\boldsymbol{\Psi} \equiv \boldsymbol{\Phi}$.
A static condensation of the equilibrium Eqs. (3.68) is not applicable, due to the singularity of $\mathbf{K}$ matrix. Calculating the inverse of coefficient matrix, it is possible to rewrite the governing equations as:

$$\begin{bmatrix} \mathbf{U}_m \\ \mathbf{R} \end{bmatrix} = \begin{bmatrix} \mathbf{B}_{11} & \mathbf{B}_{12} \\ \mathbf{B}_{21} & \mathbf{B}_{22} \end{bmatrix} \begin{bmatrix} \mathbf{F}_p \\ \bar{\mathbf{U}}_m \end{bmatrix} \tag{3.69}$$

whose solution is given by

$$\mathbf{U}_m = \mathbf{B}_{11}\, \mathbf{F}_p + \mathbf{B}_{12}\, \bar{\mathbf{U}}_m, \tag{3.70}$$

$$\mathbf{R} = \mathbf{B}_{21}\,\mathbf{F}_p + \mathbf{B}_{22}\,\bar{\mathbf{U}}_m. \tag{3.71}$$

If the stiffness matrix $\mathbf{K}$, the matrix $\mathbf{G}$, the vectors $\mathbf{U}_m$ and $\mathbf{F}_p$ are re-partitioned considering the degrees of freedom related to the block b and the interfaces i, the system of Eqs. (3.68) can be written as:

$$\begin{bmatrix} \mathbf{K}_{bb} & \mathbf{K}_{bi} & \mathbf{0} \\ \mathbf{K}_{ib} & \mathbf{K}_{ii} & -\mathbf{G}_{i\mathrm{R}} \\ \mathbf{0} & \mathbf{G}_{i\mathrm{R}}^T & \mathbf{0} \end{bmatrix} \begin{bmatrix} \mathbf{U}_{mb} \\ \mathbf{U}_{mi} \\ \mathbf{R} \end{bmatrix} = \begin{bmatrix} \mathbf{F}_{pb} \\ \mathbf{F}_{pi} \\ \bar{\mathbf{U}}_m \end{bmatrix}. \tag{3.72}$$

Considering that the whole boundary is constrained, the number of degrees of freedom related to the interfaces i coincides with the number of the components of the reaction forces R, i.e. $\mathbf{G}_{\mathrm{iR}}$ is a square matrix. Thus, instead of solving an $(b + i + \mathrm{R}) \times (b + i + \mathrm{R})$ matrix problem for the nodal degrees of freedom $\mathbf{U}_m$, we first solve a $(i \times \mathrm{R})$ problem:

$$\mathbf{U}_{mi} = \left(\mathbf{G}_{i\mathrm{R}}^T\right)^{-1} \bar{\mathbf{U}}_m, \tag{3.73}$$

followed by the use of the first and second Eqs. of the system (3.72) to recover $\mathbf{U}_{mb}$ and $\mathbf{R}$:

$$\mathbf{U}_{mb} = \mathbf{K}_{bb}^{-1} \left[\mathbf{F}_{pb} - \mathbf{K}_{bi} \left(\mathbf{G}_{i\mathrm{R}}^T\right)^{-1} \bar{\mathbf{U}}_m\right], \tag{3.74}$$

$$\mathbf{R} = \mathbf{G}_{i\mathrm{R}}^{-1} \left[\mathbf{K}_{ib}\mathbf{K}_{bb}^{-1}\mathbf{F}_{pb} - \mathbf{F}_{pi} + \left(\mathbf{K}_{ii} - \mathbf{K}_{ib}\mathbf{K}_{bb}^{-1}\mathbf{K}_{bi}\right) \left(\mathbf{G}_{i\mathrm{R}}^T\right)^{-1} \bar{\mathbf{U}}_m\right]. \tag{3.75}$$

3.4.2 Periodic BCs

With reference to Fig. 3.9, the UC is divided in seven integration domains: the first Ω_b corresponds to the volume occupied by the block with thirteen nodes. The other integration domains are the interfaces Γ_k $(k = 1, 2, 3, 4, 5, 6)$, each one defined by six nodes. With respect to the discretization used in the framework of linear BCs, the horizontal interfaces are split in two-parts to better estimate the integrals associated to the imposition of periodic conditions.

The weak form of Eq. (3.13) can be discretized using the MLS approximation function (3.53). Eqs. (3.56)÷(3.59) are here re-called to obtain:

$$\begin{aligned}
&\delta\mathbf{U}_m^T \left\{ \left[\int_{\Omega_b} \mathbf{S}_b^T \mathbf{\Phi}_b^T \mathbf{C}^T \mathbf{E}_b \mathbf{C} \mathbf{\Phi}_b \mathbf{S}_b \, d\Omega + \right.\right. \\
&\left. + \sum_{k=1}^{6} \int_{\Gamma_k} \left(\mathbf{\Phi}_k \mathbf{S}_k - \mathbf{\Phi}_b \mathbf{S}_b \right)^T \mathbf{T}_k^T \mathbf{E}_i \, \mathbf{T}_k \left(\mathbf{\Phi}_k \mathbf{S}_k - \mathbf{\Phi}_b \mathbf{S}_b \right) d\Gamma \right] \mathbf{U}_m + \\
&+ \sum_{k=1}^{3} \int_{\Gamma_k^+} \left(\mathbf{\Phi}_k \mathbf{S}_k - \mathbf{\Phi}_{k+3} \mathbf{S}_{k+3} \right)^T \mathbf{\Phi}_k \bar{\bar{\mathbf{S}}}_k \mathbf{\Lambda} d\Gamma - \left(\mathbf{\Phi}_i \left(\mathbf{x}=\bar{\mathbf{x}} \right) \mathbf{S}_i \right)^T \mathbf{R} + \\
&\left. - \sum_{k=1}^{6} \int_{\Gamma_k} \left(\mathbf{\Phi}_k \mathbf{S}_k - \mathbf{\Phi}_b \mathbf{S}_b \right)^T \mathbf{T}_k^T \mathbf{E}_i \, \left[\mathbf{u}_{mi} \right]^p d\Gamma \right\} + \\
&+ \delta\mathbf{\Lambda}^T \left\{ \sum_{k=1}^{3} \int_{\Gamma_k^+} \bar{\bar{\mathbf{S}}}_k{}^T \mathbf{\Phi}_k{}^T \left[\left(\mathbf{\Phi}_k \mathbf{S}_k - \mathbf{\Phi}_{k+3} \mathbf{S}_{k+3} \right) \mathbf{U}_m - \boldsymbol{\varepsilon}_M \Delta\mathbf{x} \right] d\Gamma \right\} + \\
&- \delta\mathbf{R}^T \left[\mathbf{\Phi}_i \left(\mathbf{x}=\bar{\mathbf{x}} \right) \mathbf{S}_i \mathbf{U}_m - \bar{\mathbf{u}}_m \right] = 0.
\end{aligned} \tag{3.76}$$

In the equality (3.76), k is an index with variation associated to the associated summation, i is whatever fixed index between 1 to 6. $\mathbf{\Phi}_i \left(\mathbf{x}=\bar{\mathbf{x}} \right)$ represents the shape functions of a generic interfacial domain calculated in a generic point of coordinates $\bar{\mathbf{x}}$, $\bar{\bar{\mathbf{S}}}_k$ indicates the selectivity matrix of the Lagrangian multipliers $\mathbf{\Lambda}$. Positions (3.61÷3.63) and (3.66) are again considered, while new ones are made:

$$\mathbf{G}_1 = \sum_{k=1}^{3} \int_{\Gamma_k^+} \left(\mathbf{\Phi}_k \mathbf{S}_k - \mathbf{\Phi}_{k+3} \mathbf{S}_{k+3} \right)^T \mathbf{\Phi}_k \bar{\bar{\mathbf{S}}}_k d\Gamma \tag{3.77}$$

$$\mathbf{G}_2 = \mathbf{S}_i^T \mathbf{\Phi}_i \left(\mathbf{x}=\bar{\mathbf{x}} \right)^T \tag{3.78}$$

$$\bar{\mathbf{U}}_m = \sum_{k=1}^{3} \int_{\Gamma_k^+} \bar{\bar{\mathbf{S}}}_k{}^T \mathbf{\Phi}_k{}^T \boldsymbol{\varepsilon}_M \Delta\mathbf{x} d\Gamma \tag{3.79}$$

Thus Eq. (3.76) becomes

$$\delta \mathbf{U}_m^T \left(\mathbf{K}\mathbf{U}_m + \mathbf{G}_1\boldsymbol{\Lambda} - \mathbf{G}_2\mathbf{R} - \mathbf{F}_p \right) + \\ - \delta\boldsymbol{\Lambda}^T \left({\mathbf{G}_1}^T\mathbf{U}_m - \bar{\mathbf{U}}_m \right) - \delta\mathbf{R}^T \left({\mathbf{G}_2}^T\mathbf{U}_m - \bar{\mathbf{u}}_m \right) = 0 \quad (3.80)$$

Since Eq. (3.76) has to hold for any arbitrary $\delta\mathbf{U}_m$, $\delta\boldsymbol{\Lambda}$ and $\delta\mathbf{R}$, the governing equations of the UC are thus obtained:

$$\begin{bmatrix} \mathbf{K} & \mathbf{G}_1 & -\mathbf{G}_2 \\ \mathbf{G}_1^T & \mathbf{0} & \mathbf{0} \\ \mathbf{G}_2^T & \mathbf{0} & \mathbf{0} \end{bmatrix} \begin{bmatrix} \mathbf{U}_m \\ \boldsymbol{\Lambda} \\ \mathbf{R} \end{bmatrix} = \begin{bmatrix} \mathbf{F}_p \\ \bar{\mathbf{U}}_m \\ \bar{\mathbf{u}}_m \end{bmatrix}. \quad (3.81)$$

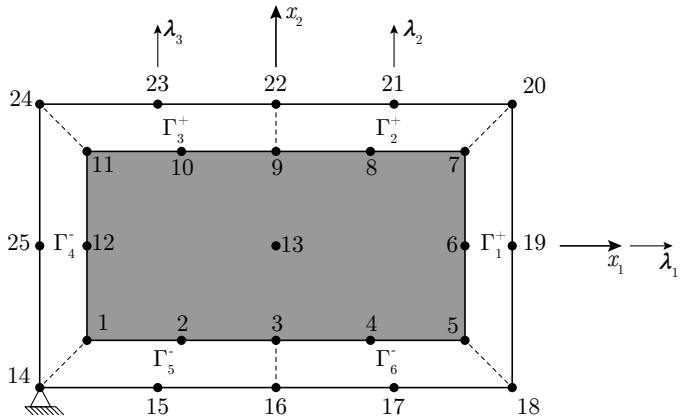

Figure 3.9: UC Meshless model for periodic BCs.

3.5 Nonlinear solution of the UC BVP

The elasto-plastic numerical response of the UC has to be evaluated for a fixed value of the macroscopic strain increment.
Let $[0,T] \subset \Re$ be the time interval of interest. At the generic time step $[t_n, t_{n+1}] \subset [0,T]$ the increment $\Delta\boldsymbol{\varepsilon}_M$ of the macroscopic strain is given at the generic sample point of the macroscopic finite element model. This value permits to evaluate the corresponding increment $\Delta\bar{\mathbf{U}}_m$ of nodal displacements to set up the UC BVP through Eq. (3.66) and Eq. (3.79) with linear or periodic BCs, respectively:

$$\Delta\bar{\mathbf{U}}_m = \mathbf{Q}^T \Delta\varepsilon_M \tag{3.82}$$

where

$$\mathbf{Q} = \sum_{k=1}^{4} \int_{\Gamma_k} \mathbf{D}_m^T \boldsymbol{\Phi}_k \bar{\mathbf{S}}_k d\Gamma, \tag{3.83}$$

with $\mathbf{D}_m = \begin{bmatrix} x_1 & 0 & x_2/2 \\ 0 & x_2 & x_1/2 \end{bmatrix}$, under linear BCs (**??**),
while

$$\mathbf{Q} = \sum_{k=1}^{3} \int_{\Gamma_k^+} \mathbf{D}_m^T \boldsymbol{\Phi}_k \bar{\bar{\mathbf{S}}}_k d\Gamma, \tag{3.84}$$

with $\mathbf{D}_m = \begin{bmatrix} \Delta x_1 & 0 & \Delta x_2/2 \\ 0 & \Delta x_2 & \Delta x_1/2 \end{bmatrix}$, under periodic BCs (3.36).

The solution of the nonlinear BVP (Eq. (3.69)) is carried out making use of an iterative procedure of Newton-Raphson (NR) type which leads to the numerical evaluation of the increments of the mesoscopic displacements and reaction forces:

$$\Delta\mathbf{U}_{m_{n+1}}^{(k)} = \mathbf{U}_{m_{n+1}}^{(k)} - \mathbf{U}_{m_n} \tag{3.85}$$

$$\Delta \mathbf{R}_{n+1}^{(k)} = \mathbf{R}_{n+1}^{(k)} - \mathbf{R}_n \tag{3.86}$$

where the apex k indicates the kth iteration of the iterative NR procedure in the time step $[t_n, t_{n+1}]$.

Introducing the vector of the unknowns

$$\mathbf{d}_{n+1}^{(k)} = \begin{bmatrix} \mathbf{U}_{m_{n+1}}^{(k)} \\ \mathbf{R}_{n+1}^{(k)} \end{bmatrix}, \tag{3.87}$$

and the error function

$$\left| \boldsymbol{\mathcal{E}}_{n+1}^{(k)} \right| = \left| \begin{bmatrix} \mathbf{K} & -\mathbf{G} \\ \mathbf{G^T} & \mathbf{0} \end{bmatrix} \begin{bmatrix} \mathbf{U}_{m_{n+1}}^{(k)} \\ \mathbf{R}_{n+1}^{(k)} \end{bmatrix} - \begin{bmatrix} \mathbf{F}_{p_{n+1}}^{(k)} \\ \bar{\mathbf{U}}_{m_{n+1}} \end{bmatrix} \right|, \tag{3.88}$$

the iterative procedure converges if the following condition is satisfied:

$$\left| \boldsymbol{\mathcal{E}}_{n+1}^{(k)} \right| < tol. \tag{3.89}$$

The linearization of the residual $\boldsymbol{\mathcal{E}}$ at the kth iteration gives:

$$\boldsymbol{\mathcal{E}}_{n+1}^{(k)} = \boldsymbol{\mathcal{E}}_{n+1}^{(k-1)} + \left. \frac{d\boldsymbol{\mathcal{E}}}{d\mathbf{d}} \right|_{n+1} \Delta \mathbf{d}_{n+1}^{(k)} \tag{3.90}$$

and the imposition of condition (3.89) in a strong form gives the increment of the unknowns vector:

$$\Delta \mathbf{d}_{n+1}^{(k)} = - \left. \frac{d\boldsymbol{\mathcal{E}}}{d\mathbf{d}} \right|_{n+1} \boldsymbol{\mathcal{E}}_{n+1}^{(k-1)} \tag{3.91}$$

with

$$\left. \frac{d\boldsymbol{\mathcal{E}}}{d\mathbf{d}} \right|_{n+1} = \begin{bmatrix} \left(\mathbf{K} - \left. \frac{d\mathbf{F}_p}{d\mathbf{U}_m} \right|_{n+1} \right) & -\mathbf{G} \\ \mathbf{G}^T & \mathbf{0} \end{bmatrix}, \tag{3.92}$$

where

$$\left. \frac{d\mathbf{F}_p}{d\mathbf{U}_m} \right|_{n+1} = \sum_{k=1}^{4} \int_{\Gamma_k} \left(\boldsymbol{\Phi}_k \, \mathbf{S}_k - \boldsymbol{\Phi}_b \, \mathbf{S}_b \right)^T \mathbf{T}_k^T \mathbf{E}_i \left. \frac{d[\mathbf{u}_{mi}]^p}{d\,[\mathbf{u}_{mi}]} \right|_{n+1} \mathbf{T}_k \left(\boldsymbol{\Phi}_k \, \mathbf{S}_k - \boldsymbol{\Phi}_b \, \mathbf{S}_b \right) d\Gamma \tag{3.93}$$

When imposing periodic BCs the nonlinear BVP is formulated in Eq. (3.80). The same procedure conformed to the different solving system leads to considering also the increments of tractions on the UC boundary

$$\Delta\boldsymbol{\Lambda}_{n+1}^{(k)} = \boldsymbol{\Lambda}_{n+1}^{(k)} - \boldsymbol{\Lambda}_n, \tag{3.94}$$

and the vector of unknowns and the error function become

$$\mathbf{d}_{n+1}^{(k)} = \begin{bmatrix} \mathbf{U}_{m_{n+1}}^{(k)} \\ \boldsymbol{\Lambda}_{n+1}^{(k)} \\ \mathbf{R}_{n+1}^{(k)} \end{bmatrix}, \tag{3.95}$$

$$\left|\boldsymbol{\mathcal{E}}_{n+1}^{(k)}\right| = \left| \begin{bmatrix} \mathbf{K} & \mathbf{G}_1 & -\mathbf{G}_2 \\ \mathbf{G}_1{}^T & \mathbf{0} & \mathbf{0} \\ \mathbf{G}_2{}^T & \mathbf{0} & \mathbf{0} \end{bmatrix} \begin{bmatrix} \mathbf{U}_{m_{n+1}}^{(k)} \\ \boldsymbol{\Lambda}_{n+1}^{(k)} \\ \mathbf{R}_{n+1}^{(k)} \end{bmatrix} - \begin{bmatrix} \mathbf{F}_{p_{n+1}}^{(k)} \\ \bar{\mathbf{U}}_{m_{n+1}} \\ \bar{\mathbf{u}}_{m_{n+1}} \end{bmatrix} \right|. \tag{3.96}$$

3.5.1 Plastic forces and consistent tangent stiffness matrix evaluation

Let us assume that the state variables at time $t_n \in [0, T]$ for any evaluation point of the UC interfaces are known, that is

$$\{[\mathbf{u}_{mi}]_n, [\mathbf{u}_{mi}]_n^p, \xi_n^p\} \qquad \text{given at } t_n. \tag{3.97}$$

The interface constitutive laws have to be integrated in order to update the field variables (3.97) to t_{n+1} in a manner consistent with the interfaces constitutive equations reported in Section 3.2.1

The algorithm is based on a two-step procedure which splits the nonlinear evolution problem defined by (3.18)÷(3.20) in an *elastic trial predictor* stage and in a *plastic corrector* stage [29, 85]. In the elastic predictor stage the increment of the displacement discontinuities is considered fully elastic and the trial contact tractions are used to evaluate the yield functions (3.15) and (3.16). If the limit functions assume a negative value, the trial solution coincides with the actual one, otherwise the corrector stage is activated and the kinematical variables are updated as follows:

$$[\mathbf{u}_{mi}]^p_{n+1} = [\mathbf{u}_{mi}]^p_n + \Delta\,[\mathbf{u}_{mi}]^p_{n+1}\,, \tag{3.98}$$

$$\xi^p_{n+1} = \xi^p_n + \Delta\xi^p_{n+1}, \tag{3.99}$$

where the increments are given by transforming the flow rules (3.18) into a discrete form. Applying the classical implicit backward-Euler difference scheme, we have:

$$\Delta\,[\mathbf{u}_{mi}]^p_{n+1} = \Delta\lambda^{p1}\,\frac{\partial G^p}{\partial\sigma_{mi}}\bigg|_{n+1} + \Delta\lambda^{p2}\,\frac{\partial\phi^{p2}}{\partial\sigma_{mi}}\bigg|_{n+1}, \tag{3.100}$$

$$\Delta\xi^p_{n+1} = -\Delta\lambda^{p1}\,\frac{\partial\phi^{p1}}{\partial\chi^p}\bigg|_{n+1} - \Delta\lambda^{p2}\,\frac{\partial\phi^{p2}}{\partial\chi^p}\bigg|_{n+1}. \tag{3.101}$$

The plastic multipliers are derived imposing the discrete counterpart of loading/unloading conditions (3.19) and (3.20). After the corrector stage the mechanical quantities associated to (3.98) and (3.99) are equal to:

$$\boldsymbol{\sigma}_{mi_{n+1}} = \mathbf{E}_i\left([\mathbf{u}_{mi}]_{n+1} - [\mathbf{u}_{mi}]^p_{n+1}\right) \tag{3.102}$$

$$\chi^p_{n+1} = h^p\,\xi^p_{n+1} \tag{3.103}$$

where

$$[\mathbf{u}_{mi}]_{n+1} = [\mathbf{u}_{mi}]_n + \Delta[\mathbf{u}_{mi}]_{n+1} \tag{3.104}$$

with

$$\Delta[\mathbf{u}_{mi}]_{n+1} = \mathbf{T}_k\left(\boldsymbol{\Phi}_k\,\mathbf{S}_k - \boldsymbol{\Phi}_b\,\mathbf{S}_b\right)\Delta\mathbf{U}_m. \tag{3.105}$$

To obtain a complete quadratic convergency of the Newton-Raphson procedure, the consistent tangent stiffness matrix is also derived at the interfaces

level. The notion of consistent tangent stiffness matrix is here used in the classical way:

$$\mathbf{E}_i^{ct} = \left. \frac{d\boldsymbol{\sigma}_{mi}}{d\left[\mathbf{u}_{mi}\right]} \right|_{n+1}, \tag{3.106}$$

which, in view of Eq. (3.102), can be rewritten as

$$\mathbf{E}_i^{ct} = \mathbf{E}_i \left(\mathbf{I} - \left. \frac{d[\mathbf{u}_{mi}]^p}{d\left[\mathbf{u}_{mi}\right]} \right|_{n+1} \right) \tag{3.107}$$

where $\mathbf{I}$ is the unit matrix.
The total derivatives, taking into account Eqs. (3.98)÷(3.101), can be explicitly calculated as functions of the plastic multipliers, which assume specific expressions on the basis of the plastic mechanism occurring at the interface.
Eq. (3.107) can be replaced in Eq. (3.93) to obtain the following equivalence:

$$\left. \frac{d\mathbf{F}_p}{d\mathbf{U}_m} \right|_{n+1} = \mathbf{K}_i - \mathbf{K}_{i_{n+1}}^{ct} \tag{3.108}$$

where

$$\mathbf{K}_{i_{n+1}}^{ct} = \sum_{k=1}^{4} \int_{\Gamma_k} \left(\boldsymbol{\Phi}_k \, \mathbf{S}_k - \boldsymbol{\Phi}_b \, \mathbf{S}_b \right)^T \mathbf{T}_k^T \mathbf{E}_i^{ct} \mathbf{T}_k \left(\boldsymbol{\Phi}_k \, \mathbf{S}_k - \boldsymbol{\Phi}_b \, \mathbf{S}_b \right) d\Gamma \tag{3.109}$$

is the consistent stiffness matrix including the contribute of all interfaces.
According to Eqs. (3.63) and (3.108) the first partition matrix in Eq. (3.92) can be replaced by the consistent stiffness matrix of the UC:

$$\mathbf{K}_{n+1}^{ct} = \mathbf{K}_b + \mathbf{K}_{i_{n+1}}^{ct}. \tag{3.110}$$

3.6 UC response in pure modes

3.6.1 Linear BCs

In order to validate the nonlinear behavior of the UC, simple numerical examples were carried out under displacement control for the two cases of (i) stretching along x_2 direction, i.e. $[0\,\varepsilon_{x_2}\,0]^T$, and (ii) pure shear, i.e. $[0\,0\,\gamma]^T$. The UC is made up of a clay block with dimensions 204x50 mm, surrounded by 10 mm thick mortar joint. The mechanical parameters adopted are reported in Table 3.1 and coincide with those assumed in other numerical examples [29, 53]. The UC discretization is the one showed in Fig. 3.8. Three Gauss points were located on each interface.

Parameters	$E\ [MPa]$	ν	$c_0\ [MPa]$	$\sigma_0\ [MPa]$	$h_p\ [MPa^-1]$	$\varphi\ [^o]$	$\delta\ [^o]$
Mortar	820	0.14	0.35	0.25	500	37	$1/2\ \varphi$
Blocks	16700	0.15	–	–	–	–	–

Table 3.1: UC pure modes response: elastic and inelastic parameters adopted for the blocks and interfaces constitutive model.

The stress-strain diagrams $\sigma_{x_2} - \varepsilon_{x_2}$ and $\sigma_{x_1} - \varepsilon_{x_2}$ are reported in Fig. 3.10 (a) and (b), respectively. After the elastic stage, tensile plasticity activates at the bed joints, that results in the softening branch. The slope of the same branch changes promptly when plasticity in shear mode appears at the head joints. Therefore, the overall response of the UC is the result of opening of the bed joints and sliding at the head joints. The unloading/loading branches show the effect of progressive accumulation of inelastic displacement discontinuities at the interfaces. The horizontal stress σ_{x_1} is positive in the elastic stage due to the Poisson effect, then it changes its sign in the softening branch due to the dilatancy effect appearing at the head joints.
In the right column of Fig. 3.10, the UC response is illustrated under a cyclic pure mode II. Also in this case, the elastic behavior is followed by plasticity and a crucial role is played by dilatancy appearing at both bed and head joints. The dilatancy effect generates compressive contact tractions that increase the shear strength of the UC, with the result that the shear stress increases during the cyclic load until the interfaces are totally fractured. When the shear stress becomes constant, dilatancy becomes zero and also the normal contact stresses assume a constant value.

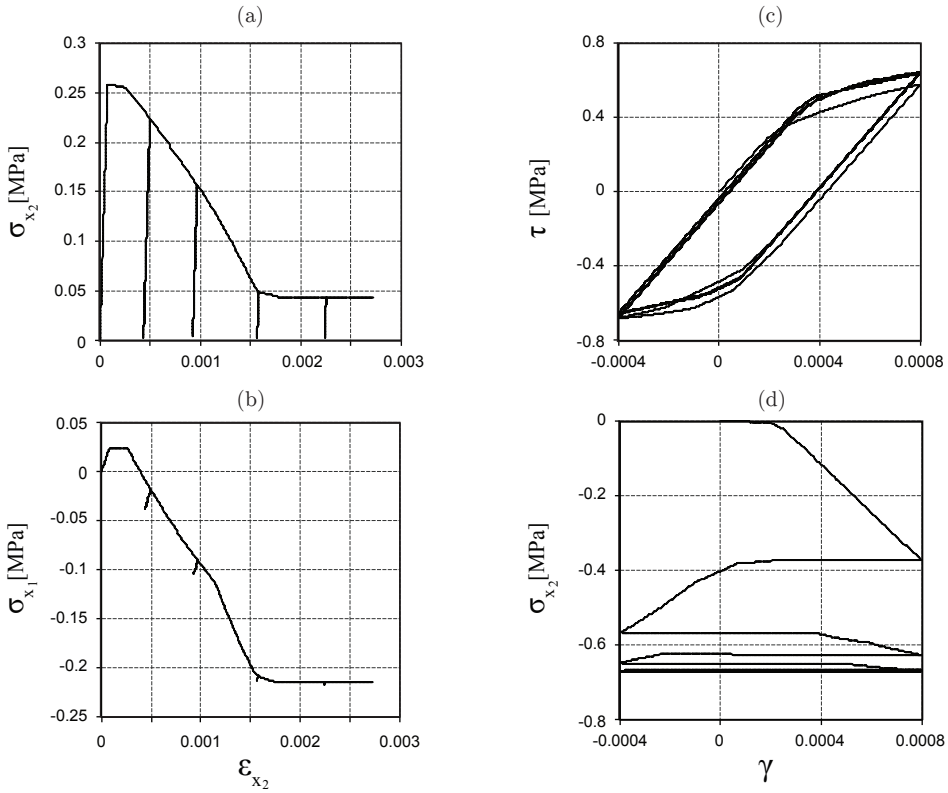

Figure 3.10: UC response in mode I with unloading branches: (a) $\sigma_{x_2} - \varepsilon_{x_2}$ curve; (b) $\sigma_{x_1} - \varepsilon_{x_2}$ curve. UC cyclic response in mode II: (c) $\tau - \gamma$ curve; (d) $\sigma_{x_2} - \gamma$ curve.

3.6.1.1 Choice of the weight function

The shape functions are obtained from the weight function, also called kernel or window function, that is denoted by $w_j(\mathbf{x})$ [66]. Different kinds of weight function may be used. They have always a compact support whose size is defined by the so called dilatation parameter or smoothing length d, see Section 3.4. It plays an important role in the performance of the numerical method and can be regarded as the element size in the finite element method. The weight function should be constructed so that they are positive and that a unique solution is guaranteed. They are monotonic decreasing functions with respect to the distance from $\mathbf{x}$ to $\mathbf{x_j}$.
In Fig. 3.11, the response of the UC in mode I, under the condition of stretching

along x_1 direction, is reported using different weight functions. Specifically the quartic spline

$$w_j(\mathbf{x}) = \begin{cases} 1 - 6\,r_j^2 + 8\,r_j^3 - 3\,r_j^4, & \text{for} \quad 0 \le r_j \le 1 \\ 0, & \text{for} \quad r_j \ge 1 \end{cases} \tag{3.111}$$

the cubic spline

$$w_j(\mathbf{x}) = \begin{cases} \frac{2}{3} - 4r_j^2 + 4r_j^3, & \text{for} \quad r_j \le 2 \\ \frac{4}{3} - 4r_j + 4r_j^2 - \frac{4}{3}r_j^3, & \text{for} \quad \frac{1}{2} < r_j \le 1 \\ 0, & \text{for} \quad r_j > 1 \end{cases} \tag{3.112}$$

and the exponential function

$$w_j(\mathbf{x}) = \begin{cases} e^{-(\frac{r_j}{\alpha})^2}, & \text{for} \quad r_j \le 1 \\ 0, & \text{for} \quad r_j > 1 \end{cases} \tag{3.113}$$

are used, with $r_j = \|\mathbf{x} - \mathbf{x_j}\|/d$, being d the radius of the domain of definition of the point $\mathbf{x}$. In the exponential form (3.113), α is a numerical parameter to adjust the weights that was set equal to 0.4. These results refer to the discretization showed in Fig. 3.8 and the radiuses d associated to the points in the block domain Ω_b or in the interfacial domain Γ_k, are reported in Table 3.2. When using cubic spline, it is noted that the minimum radius to ensure the invertibility of matrix $\mathbf{A}$ (3.50) is d_0 in Table 3.2. Overall, the responses are in good agreement and biggest mismatch is found with the cubic spline associated to the radius d_0.

Weight Function	radius of $\mathbf{x} \in \Omega_b$	radius of $\mathbf{x} \in \Gamma_k$
Quartic spline	$\frac{3}{2}\sqrt{\left(\frac{a}{2}\right)^2 + \left(\frac{b}{2}\right)^2}$	$1.1a$ or $1.1b$
Cubic spline	$d_1 = 4\sqrt{\left(\frac{a}{2}\right)^2 + \left(\frac{b}{2}\right)^2}$	$1.1a$ or $1.1b$
Cubic spline	$d_0 = 3.8\sqrt{\left(\frac{a}{2}\right)^2 + \left(\frac{b}{2}\right)^2}$	$1.1a$ or $1.1b$
Exponential	$\frac{3}{2}\sqrt{\left(\frac{a}{2}\right)^2 + \left(\frac{b}{2}\right)^2}$	$1.1a$ or $1.1b$

Table 3.2: Radiuses of the support of the node belonging to the block or joint domain for different weight functions.

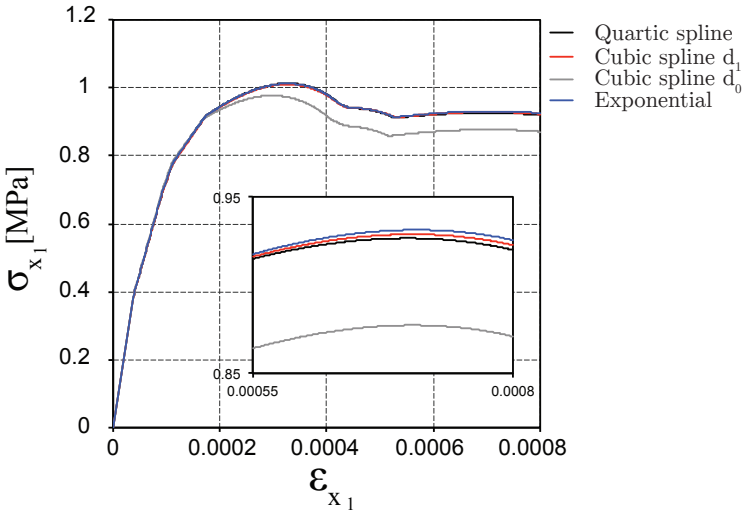

Figure 3.11: UC response in mode I using different weight functions.

Overall, the results presented in this study are obtained using the quartic spline (3.111) whose derivative is

$$\frac{\partial w_j(\mathbf{x})}{\partial \mathbf{x}} = \begin{cases} \frac{\|\mathbf{x}-\mathbf{x}_j\|}{d^2}\left(-12+24r_j-12{r_j}^2\right), & \text{for} \quad r_j \le 1 \\ 0, & \text{for} \quad r_j > 1 \end{cases} \tag{3.114}$$

that satisfies the conditions

$$\begin{gathered} w(0)=1, \qquad w(1)=0 \\ \left.\frac{dw_j}{dr_j}\right|_{r_j=0}=0, \quad \left.\frac{dw_j}{dr_j}\right|_{r_j=1}=0, \quad \left.\frac{d^2w_j}{dr_j^2}\right|_{r_j=1}=0 \end{gathered} \tag{3.115}$$

that ensure continuous first- and second-order derivatives to the weight and shape functions.

3.6.1.2 Meshless *vs* FEM UC response

The accuracy of the UC numerical response obtained by the meshless model has been assessed by making a comparison with the UC responses carried out using a finite element model.
In the FEM formulation, the brick is modelled using four-noded two-dimensional elements while the mortar joints are discretized making use of 4-nodes ZTI elements.
First, a convergence analysis by h-refinement was performed to obtain a proper mesh size ensuring appropriate mesh independency of the results. It was found that the reference mesh could be constituted by 64 two-dimensional elements and 40 interfaces.
In the meshless formulation the refinement can be achieved by increasing the number of nodes. This expedient leads also to an increase of the order of the shape functions. Another refinement involves the Gauss points (GPs) which have to be chosen in a number sufficient for accurately approximating the integrals on the whole domain.
Three different meshless configurations were considered, having 17, 33 and 41 nodes, respectively. In the 17 nodes model, 3, 5 or 7 GPs were associated to each interface, therefore they are named 17_3, 17_5, 17_7 models, respectively. The number of GPs were also incremented in the block domain. In the 33 nodes model, 5 or 7 GPs per interface were used (33_5, 33_7 models), while in the 41 nodes only 7 GPs were employed (41_7 model), see Fig. 3.12.
The mechanical response of the UC in pure mode I (stretching along x_1 and x_2) and II (shear test) is analyzed with the meshless models of Fig. 3.12 and compared with the same responses carried-out by the FE reference model. In Figs. 3.13-3.15 the stress-strain diagrams for each meshless configuration are plotted. In order to compare analytically the results, three error parameters have been calculated, namely the Root Mean Square Deviation (RMSD), the maximum absolute error (Abs err) and the maximum relative error (Rel err). In Tables 3.3, 3.4 and 3.5, the values of the three parameters are reported.
It is remarkable that sometimes, in the Meshless formulation, the increasing in the number of the evaluation points is more efficient than an increasing in the number of nodes, as in the case of 17 nodes with 7 Gauss points compared to the case of 33 nodes with 5 Gauss points. Over all cases, the Meshless model with 33 nodes and 7 evaluation points for each interface reveals to be in perfect agreement with the reference curve, even if responses employing lower parameters could be considered also acceptable.

At the minimum, 66 degrees of freedom are sufficient in the Meshless formulation to obtain the same response of a 250 degrees of freedom FE model. The saving in terms of computational cost is obvious.

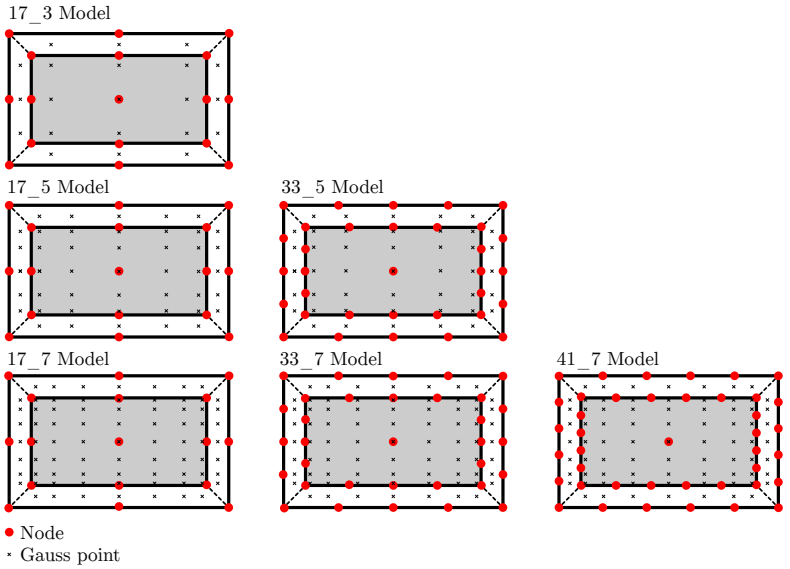

Figure 3.12: Accuracy test: different meshless discretizations.

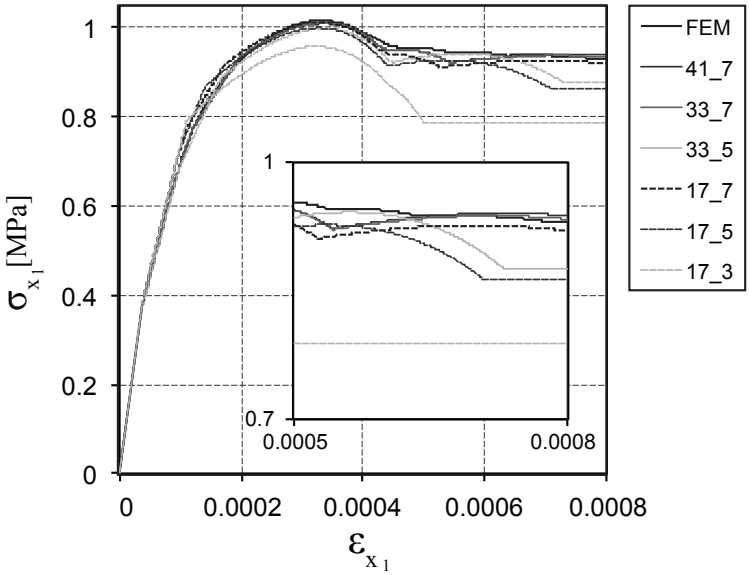

Figure 3.13: FEM vs Meshless UC response: (a) $\sigma_{x_1} - \varepsilon_{x_1}$ trends for the mesoscale Meshless models compared with the 104 elements FE discretization.

Meshless model	*RMSD* [%]	*Abs err* [*MPa*]	*Rel err* [%]
17_3	11.503	0.161	16.993
17_5	3.812	0.070	7.500
17_7	1.980	0.040	5.494
33_5	2.543	0.057	6.150
33_7	0.770	0.023	2.467
41_7	0.773	0.022	2.348

Table 3.3: RMSD, absolute error and relative error in $\sigma_{x_1} - \varepsilon_{x_1}$ curves between Meshless configurations and 104 elements FE model.

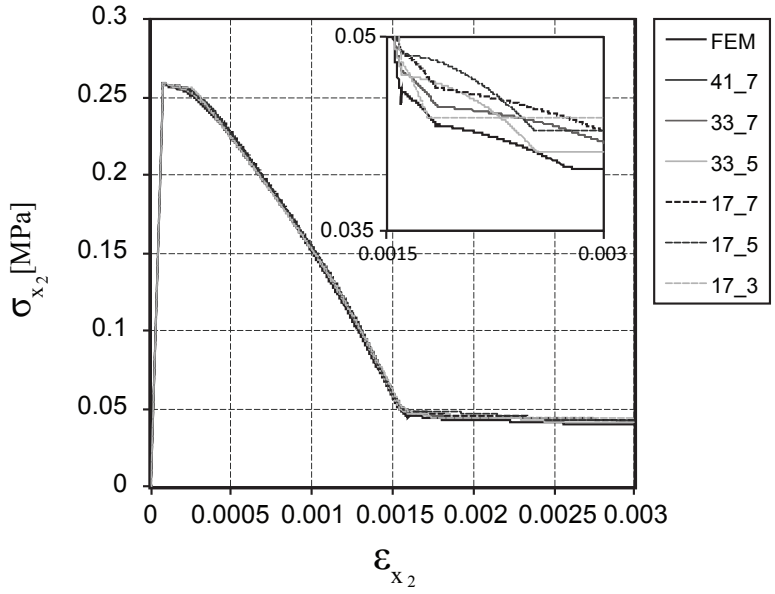

Figure 3.14: FEM vs Meshless UC response: (a) $\sigma_{x_2} - \varepsilon_{x_2}$ trends for the mesoscale Meshless models compared with the 104 elements FE discretization.

Meshless model	$RMSD$ [%]	$Abs\ err\ [MPa]$	$Rel\ err$ [%]
17_3	2.019	0.008	4.316
17_5	1.017	0.004	1.813
17_7	1.110	0.003	1.385
33_5	0.599	0.003	1.353
33_7	0.640	0.002	1.037
41_7	0.537	0.002	0.938

Table 3.4: RMSD, absolute error and relative error in $\sigma_{x_2} - \varepsilon_{x_2}$ curves between Meshless configurations and 104 elements FE model.

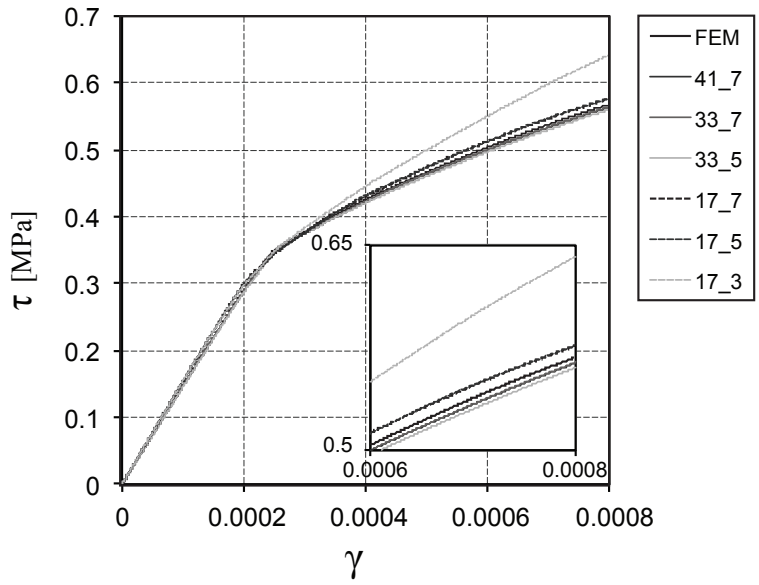

Figure 3.15: FEM vs Meshless UC response: (a) $\tau - \gamma$ trends for the mesoscale Meshless models compared with the 104 elements FE discretization.

Meshless model	$RMSD$ [%]	$Abs\ err$ $[MPa]$	$Rel\ err$ [%]
17_3	9.354	0.078	13.871
17_5	2.428	0.014	2.625
17_7	2.391	0.013	2.508
33_5	0.594	0.004	0.723
33_7	0.144	0.001	0.303
41_7	0.128	0.001	0.261

Table 3.5: RMSD, absolute error and relative error in $\tau - \gamma$ curves between Meshless configurations and 104 elements FE model.

3.6.2 Periodic BCs

In a displacement-based FE analysis, a unique solution is obtained if periodic BCs (3.36) are applied [92]. The solution obtained by applying (3.36) will also meet the traction continuity conditions

$$\sigma_n^+ - \sigma_n^- = 0, \qquad \tau_{nt}^+ - \tau_{nt}^- = 0, \tag{3.116}$$

where $\sigma_n^{+,-}$ and $\tau_{nt}^{+,-}$ are the normal and shear stresses at the corresponding periodic boundary surfaces, respectively. The conditions (3.36) can be introduced by the constraint elimination method [71] or the Lagrange multiplier method [61]. Actually, the numerical solution will be such that the traction boundary conditions will result from the solving process in a weak form. This means that the tractions, defined on the cell boundary through the shape function of the border elements, will generally not be opposite on opposite nodes of the unit cell boundary.
This aspect can be better appreciated with reference to Fig. 3.16, based on a FE analysis in pure shear strain state for the two-phases solids, characterized by a skewed-periodicity proper for running bond masonry. The presence of different continua guarantees a non-homogeneous stress state, to better observe the resulting traction BC. Fig. 3.16 (a) represents the 2D model with the boundaries Γ_1^+, Γ_2^+, Γ_3^+ periodic respectively with Γ_4^-, Γ_5^-, Γ_6^-. Figs. 3.16 (b), (c), (d), (e) show the response in terms of displacements (left column), tangential stress (central column) and absolute value of shear traction (right column) on the boundaries Γ_2^+ and Γ_5^-, for different meshes, consisting of 32, 128, 512, 2048 2D four-noded elements. The adopted meshes are periodic, thus the existence of matching nodes on periodic faces of the UC boundary, allowed to impose directly the periodic BCs by the Lagrange multiplier method. It is remarked that, when periodic BCs are discretized, some of them at the corners $a - c - e$ and $f - d - b$ are not fully independent [49]. The inclusion of dependent equations in the BCs can lead to a not full rank global stiffness matrix. In order to obtain only independent conditions at the corners, a corner should only be considered as a part of one side of two intersection ones. It is observed that the traction BC is satisfied as the mesh becomes finer. It is visible a certain disturbing border effect that tends to vanish with progressive higher refinements.

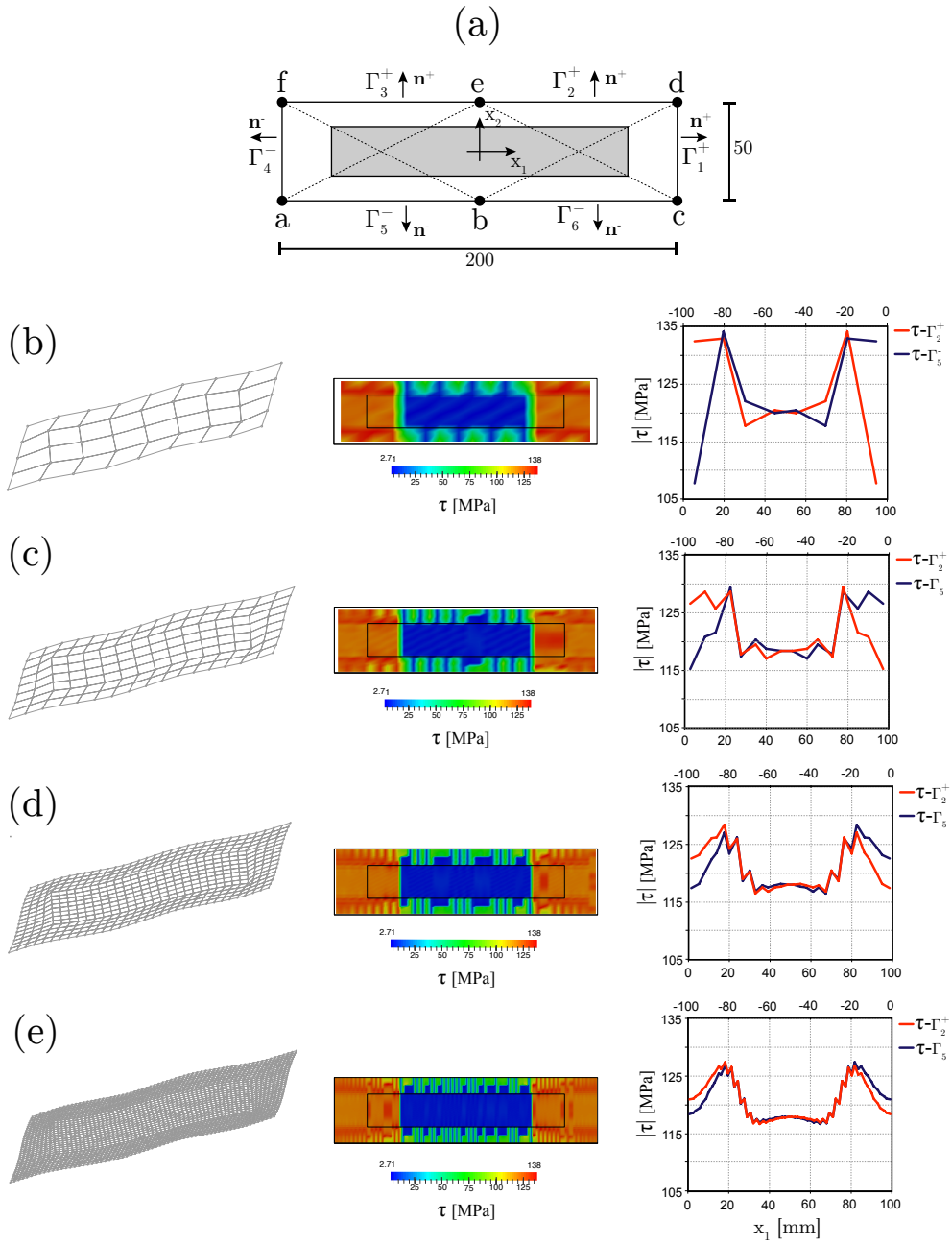

Figure 3.16: FE pure shear elastic response under periodic BCs. (a) Two phases system characterized by skewed periodicity. Deformed shape, map of tangential stress and absolute value of the tangential traction along periodic lines Γ_2^+ and Γ_5^- using (b) 32-elements mesh, (c) 128-elements mesh, (d) 512-elements mesh, (d) 2048-elements mesh.

In a displacement-based meshless analysis, due to the lack of the Kronecker delta property of MMs shape functions, the essential boundary conditions cannot be imposed as easily as in FEM. Several techniques have been proposed, namely (i) methods based on the modification of the weak form and (ii) methods using modified shape functions. For the purpose of satisfying periodic BCs, it has been already showed the application of the Lagrange multiplier method based on the modification of the weak form. This kind of formulation allows the imposition of the conditions over a boundary instead of using Node-by-Node conditions.
The meshless numerical response in pure shear strain state was analyzed for the UC showed in Fig. 3.9, constituted by a thirteen-noded block and six interfacial domains characterized by the same skewed periodicity presented in Section 3.3. Totally 25 nodes realize the meshless discretization. It was found that periodicity was strictly satisfied from the kinematic point of view, conversely tractions BCs was somehow not respected (Fig. 3.17). In particular, it is visible an opposite trend in terms of values on periodic bed joints both for the normal (Fig. 3.17 (a)) and shear (Fig. 3.17 (b)) tractions. An opposite trend in terms of sign is observable on periodic head joints for the normal tractions. The same response in terms of tractions was obtained by performing a FE analysis with a 20 elements mesh, i.e. 8 elements block surrounded by 12 four-noded interfaces. Lagrangian multiplier method was also adopted to impose periodic BCs in the FE model.

Based on these results, the following expedient in the meshless analysis was adopted. The shape functions that approximate the displacement of the upper interfacial domain were constructed in terms of nodes strictly belonging to the domain. Therefore, no common nodes on adjacent interfacial upper boundaries were used. The resulting meshless discretization is presented in Fig. 3.18 where totally 18 nodes are located in the UC boundary with respect to the previous 12 nodes. Differently from the results obtained using the discretization in Fig. 3.17, tractions BC appears adequately satisfied. Moreover, we found that the FE response that better approximates the obtained meshless tractions response is the one associated to 2240 elements mesh. Basically, in a FE framework, a classical h-refinement leads to the tendency of exactness of the traction BC, while the same result may be obtained in a meshless framework if there are no boundary nodes belonging to adjacent periodic lines. Undesired spurious oscillation zones are however visible in the FE response in correspondence to the intersection points of adjacent periodic boundaries.

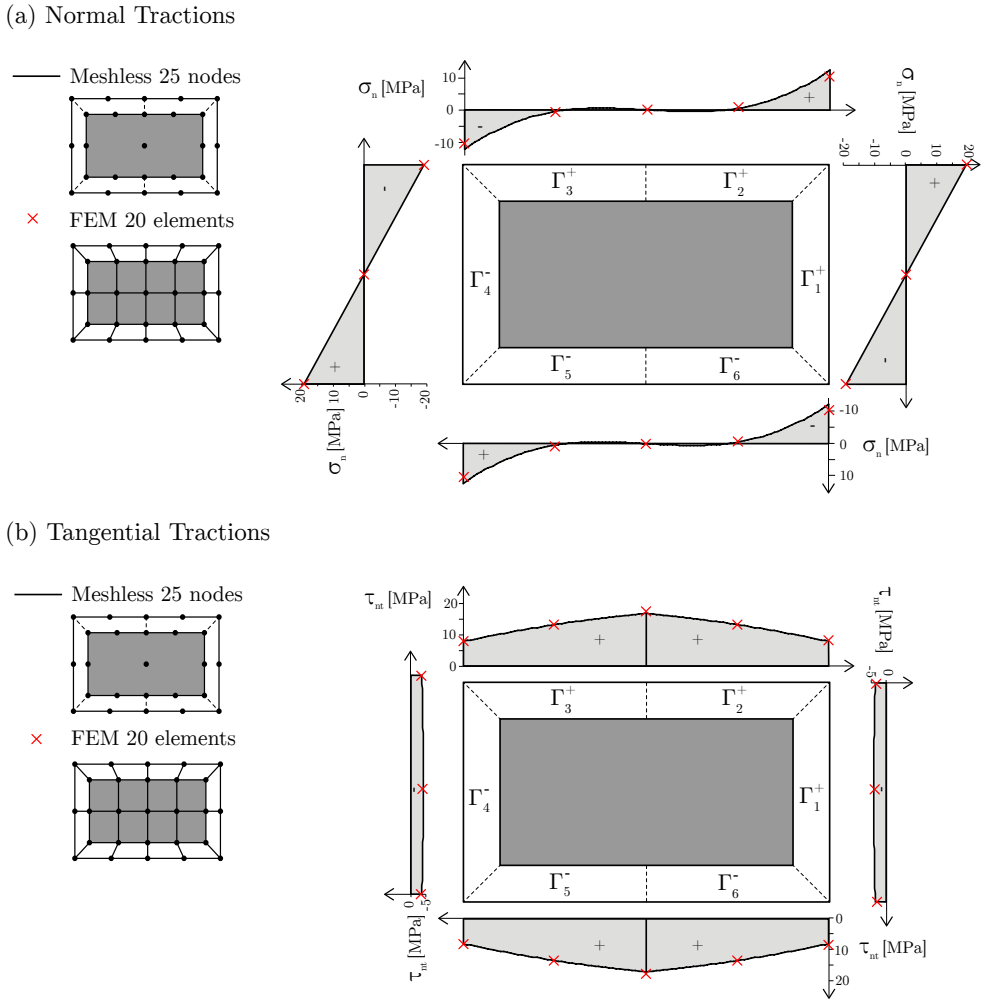

Figure 3.17: Meshless and FE pure shear elastic response of the UC. Common nodes exist between the upper boundary of different interfaces in the mesh-free discretization (a) Normal traction trend, (b) Tangential traction trend.

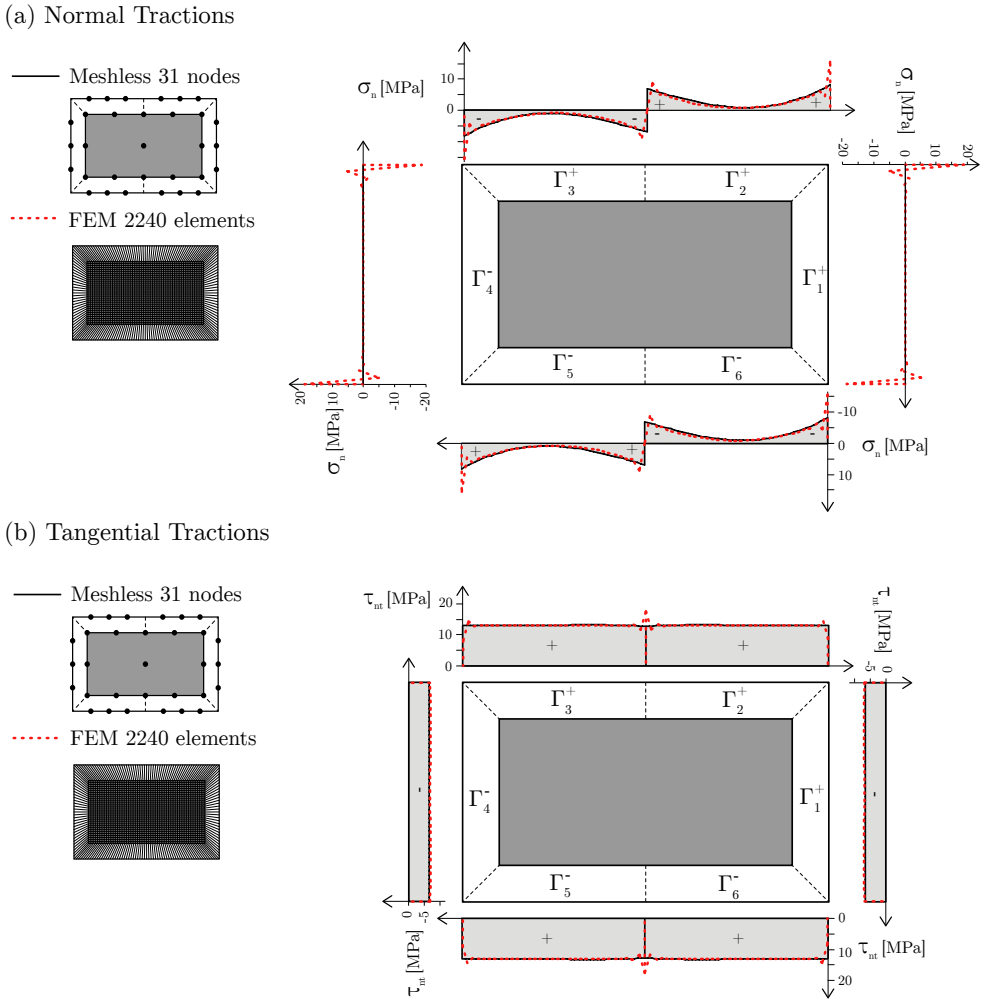

Figure 3.18: Meshless and FE pure shear elastic response of the UC. No common nodes exist between the upper boundary of different interfaces in the mesh-free discretization (a) Normal traction trend, (b) Tangential traction trend.

In Fig. 3.19 the same aspect is emphasized. The difference of the modulus of the normal (Fig. 3.19 (a)) and shear (Fig. 3.19 (b)) tractions is reported along the periodic boundaries Γ_2^+ and Γ_5^-. In a FE periodic response, the portion of the boundary where the natural BC is respected is alway centered in the domain and its width increases with finer meshes. Instead, at the ends of

each sub-domain a not negligible oscillation in the value of traction is recorded and its value in the normal component increases with the h-refinement. A very good compromise between the effectiveness of the natural BCs and the number of degrees of freedom employed is instead obtained with the meshless method if interfacial upper boundaries have no nodes in common. It may be argued that traction BC could also be satisfied by adopting a finer meshless discretization, in light of the FE results (Figs. 3.16 and 3.19), however it is remarked that increasing the number of nodes imply the increasing of the order of the shape function, therefore the integration over the domains may resulted costly in terms of number of Gauss Points. Being the periodicity respected both form the kinematic and mechanical point of view, the discretization in Fig. 3.18 was adopted to obtain the nonlinear UC meshless response.

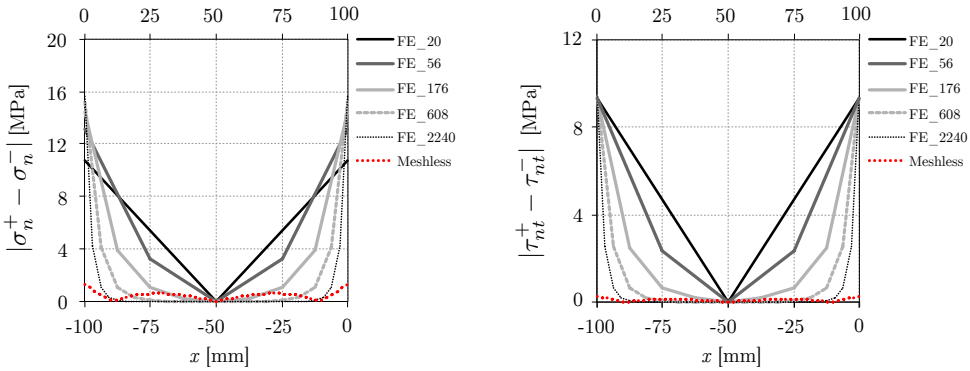

(a) Normal Traction. **(b)** Shear Traction.

Figure 3.19: Modulus difference of the tractions over the periodic boundaries Γ_2^+ and Γ_5^- obtained with FE and Meshless methods.

Figure 3.20 contains the results in terms of average stress versus average strain for the stretching test along x_1 (Fig. 3.20 (a)), x_2 (Fig. 3.20 (b)) and a shear strain test (Fig. 3.20 (c)). The results obtained by using periodic BCs is overlapped to the ones obtained by adopting linear BCs. The behavior is qualitatively the same in the three pure modes, however the responses obtained using periodic BCs underestimate the linear results by about 20% in the modes I and up to 40% in mode II. It is thought that the mismatch between the results from linear and periodic BCs can become smaller as the number of inclusions, i.e. blocks and mortar joints, inside the UC increases. On the other hand, a

bigger UC involves some drawbacks in terms of principle of separation of scales and computational efforts at the mesoscale level.
The influence of the choice of the BCs is left over to a general multi-scale CH procedure.

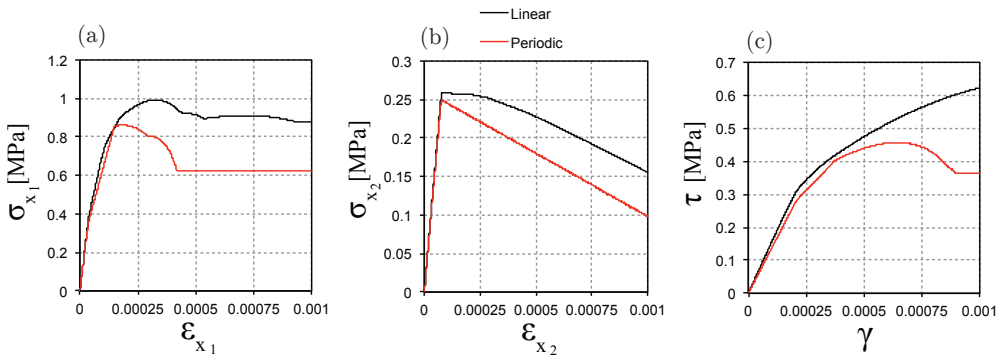

Figure 3.20: Macroscopic stress - strain diagrams for stretching (a) along x_1, (b) along x_2, (c) shear test. Trends obtained by using linear and periodic BCs are overlapped.

Chapter 4

Strain Localization analysis at the macroscopic level

4.1 Introduction

Strain localization occurs when a material is subjected to a high level of mechanical solicitations and inelastic strain develop in relatively narrow zone, generally called *process zone*, *plastic band* or *damaged zone*. Localization of strain in quasi-brittle materials is characterized by a gradual development of stress-free cracks. In ductile materials strain typically localizes into zones of intense shearing, called *shear bands*. Example of strain localization occurring for tensile loads in low-carbon steel samples is shown in Fig. 4.1 (a). Necking is the first mode occurring in the dog-bone-shaped strip shown in the top Fig. 4.1 (a). Later, shear banding (with a 45°inclination) develops within the necked zone which eventually degenerates into a fracture. Necking in a cylindrical bar under tension is visible in the bottom Fig. 4.1 (a).
Formation of shear bands is observed also in granular materials such as gravel, sands or soil, this is the case example of the cylindrical soil sample subjected to compressive axial loads in Fig. 4.1 (b). The intact sample before triaxial compression test is shown on the left. A sample tested with a free top is reported at the centre (in which a single shear band has developed), whereas a fixed top was used for the sample on the right (in which two twin shear bands have developed).

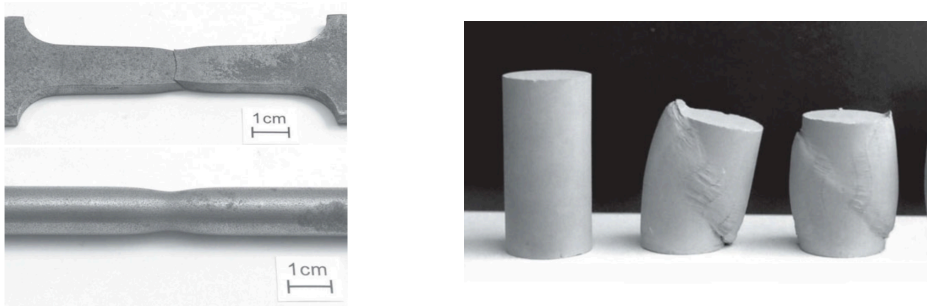

(a) Tensile tests. **(b)** Compressive tests.

Figure 4.1: Examples of strain localization. (Adapted from Bigoni [12]).

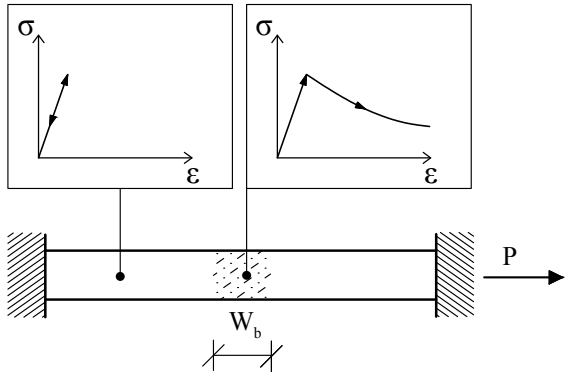

Figure 4.2: Uniaxial test: localization of inelastic strain.

In general, the process zone behaves in a different way with respect to the surrounding zones. In fact, the localized zone is generally associated to a faster growth of strain and it is characterized by inelastic phenomena such as opening and propagation of cracks, initiation and growth of voids. Conversely, outside from this zone, the material unloads elastically because the strain remains elastic. The simple example schematized in Fig. 4.2 shows the aforementioned aspect.

The localization zone is generally characterized by some specific width and inclination angle, which are governed by the material micro-structure and the boundary conditions. Some researchers have attempted to empirically link the

band width with the microstructure of the material, finding for instance 8-20 mean grain diameters d50 [1] in granular materials [25], or 3 times the maximum aggregate diameter in concrete [8].
From the theoretical point of view, extensive research has been carried out to address issues related to the modelling of localized deformation. A brief classification of models for localized failure is given in the next Section 4.2 on the basis of a kinematic description, material models and numerical approximation techniques.
In a multi-scale approach strain localization occurs both at the mesoscopic and macroscopic scale. The equivalence between the macroscopic strain localization and the mesoscopic decohesion and fracture zones can be established on the basis of the so-called spectral analysis of the acoustic tensor, built with the tangent stiffness matrix resulting from the UC BVP.
In the present study, strain discontinuities defining a localization band are introduced to represent the behavior of the physical volume associated with a Gauss point. The model is characterized by the presence of a weak discontinuity and the strain is smeared over the Gauss point volume. The fundamental hypotheses for the localization detection are reported in Section 4.3 followed by a 1D application. The process of regularization of the strain is presented in Section 4.4 and is named *smeared band model*. A 1D application that involves the smearing operation of strain is also included. The localization band width can be extracted from the UC dimensions as illustrated in Section 4.5. Numerical aspects and the localization response obtained for a UC in mode I and mixed mode, are provided in Section 4.6.

4.2 Material models

Following the classification provided by Jirásek [38], strain localization zones can be represented according to a kinematic description. Generally, three types of models can be distinguished:

- models characterized by strong discontinuities;
- models characterized by weak discontinuities;

[1] Scientists typically use the d50 as representative grain size for sediment. D50 is the median grain size used to represent the coarse fraction (50% of the sediment is finer than d50).

- models characterized by regularized localization zones.

In Fig. 4.3 the three models are represented. The strong discontinuities (Fig. 4.3 (a)) correspond to opening cracks or to slip along lines. The second model is instead identified by the presence of a plastic band or process zone with finite thickness, where a certain density of inelastic phenomena are concentrated, and separated from the remaining part of the body by two weak discontinuities. The regularized localization zones are characterized by higher concentration of defects across the center of the process zones with a transition to smaller strains in the surrounding parts of the continuum.
The models differ in the displacement and strain profiles, as shown in the second and third rows of Fig. 4.3. These profiles can be considered as arising from different choices of constitutive law for the cracking material.

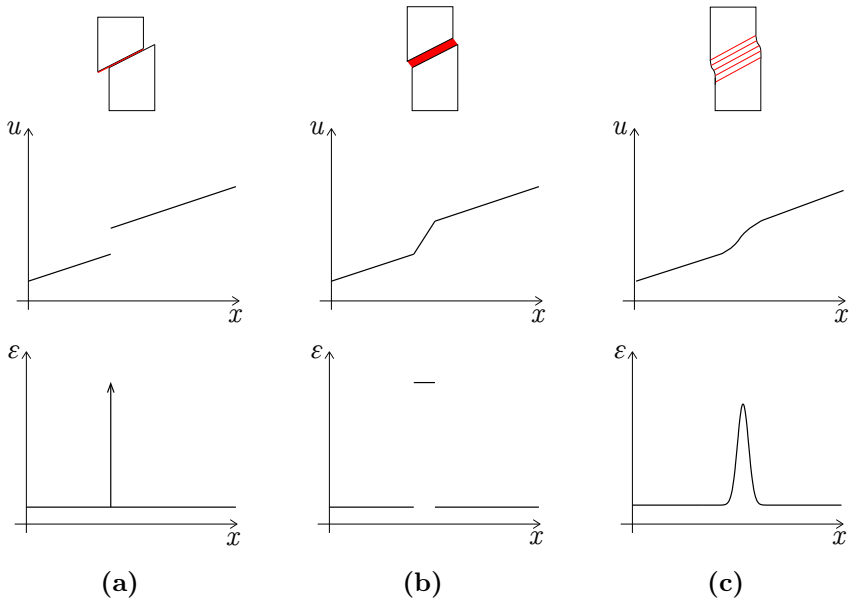

Figure 4.3: Kinematic classification of models for strain localization according to the admittance of (a) strong discontinuities (b) weak discontinuities and (c) regularized localization zones. (Adapted from [38]).

The first model is characterized by a jump in the displacement field in correspondence of the crack (Fig. 4.3 (a)). The strain field, as a consequence,

consists of the differentiation of the displacement field having a singular part, multiple of the Dirac delta distribution in correspondence of the displacement jump. In the simplest case, the strong discontinuity can be considered as stress-free and the criterion for crack propagation is formulated in terms of the stress intensity factors characterizing the singular part of the stress field. This is the approach of the linear elastic fracture mechanics, applicable at very large scales, when the process zone is negligible with respect to the characteristic dimensions of the body. Models assuming strong discontinuities usually assume that the cohesive tractions transmitted by the discontinuity depends only on the displacement jump in the direction normal to the discontinuity, even though the evolution of the process zone is in general affected also by strains (or stresses) in the tangential plane (*cohesive crack models*). Generally two independent constitutive laws are necessary to describe the behavior of the bulk material and the narrow localization zone, the former formulated as stress-strain law and the latter as a traction-separation law. In order to describe strong discontinuities, interface elements can be inserted between the finite elements of the discretized continuum whenever the discontinuity path is known in advance and is considered in the mesh generation [93]. In a general case, when the discontinuity propagates across the body along an unknown path, the kinematics of finite elements are usually enriched. In particular, standard shape functions can be enriched by special discontinuous functions. Typical examples in this sense include the *extended finite elements* [10, 20, 86] and the *elements with embedded strong discontinuities* [22, 44, 81], which allow displacement jumps on arbitrary position.

Differently, models with localization bands bounded by weak discontinuities are represented by the continuity of the displacement while the strain components have a jump (Fig. 4.3 (b)). In this case, it is possible to distribute the inelastic strain uniformly across the width of a band of a finite thickness, instead of lumping all the inelastic effects into a line or a surface. This naturally leads to the smeared crack models, which transform the traction-separation law into a law that links the stress transmitted by the localization band to the average inelastic strain in that band, obtained dividing the normal component of the displacement jump by the thickness of the band. In this framework special elements with *embedded localization bands* permit the modeling of bands of an arbitrary direction with respect to the basic mesh, and also of an arbitrary thickness [11, 82].

Lastly, regularized localization zones are featured by a continuously differentiable displacement field so the strain field remains continuous after the onset

of localization (Fig. 4.3 (c)). These approaches generally consider constitutive enrichments with an internal length scale related to the width of the localization zone. Nonlocal and gradient theories that relate the constitutive behavior of a material point with those in the neighboring region, the size of which is governed by the width of the localization zone, fall into this category [41, 70].

4.3 Continuous and Discontinuous bifurcation

In the context of multi-scale analysis, it is necessary to determine the conditions for the onset of the band formation process at the macro-scale. For that reason, all the tensors mentioned in this and in the following sections have to be considered as macroscopic quantities. The localization process is governed by the inelastic phenomena occurring at the UC level. According to the general localization theory, when the inelastic strain increments localize in one or more narrow bands, weak discontinuity surfaces exist. Across such surfaces, the displacement field remains continuous but the strain field can have a jump. Supposing that after loading a specimen, a process zone develops (Fig. 4.4). Considering an infinitesimal volume extracted in correspondence of the discontinuity surface identified by the unit vector normal $\mathbf{n}$, two different subdomains Ω^+ and Ω^- can be distinguished. At the incipient weak discontinuity, the material of Ω^+ and Ω^- is the same but the strain and stress rates of the two subdomains cannot be the same. In this context, quantities denoted by symbol " $+$ " are referred to the material outside the localization band, while negative quantities denoted by symbol " $-$ " are referred to the material inside the localization band.
The first fundamental hypotheses is the traction continuity condition:

$$\dot{\boldsymbol{\sigma}}_M^+ \cdot \mathbf{n} = \dot{\boldsymbol{\sigma}}_M^- \cdot \mathbf{n}. \tag{4.1}$$

If the macroscopic stress tensor $\dot{\boldsymbol{\sigma}}_M$ is decomposed into the in-plane components ($\dot{\sigma}_{tt}$; $\dot{\sigma}_{ss}$; $\dot{\sigma}_{ts}$) and out-of-plane components ($\dot{\sigma}_{nn}$; $\dot{\sigma}_{nt}$; $\dot{\sigma}_{ns}$) with respect to the plane tangent to the discontinuity surface, the traction continuity condition means that the out-of-plane stress rates must be continuous. Jumps can appear in the in-plane components, as emphasized for the normal component $\dot{\sigma}_{tt}$ in Fig. 4.4.
The second set of equations are the compatibility conditions which require

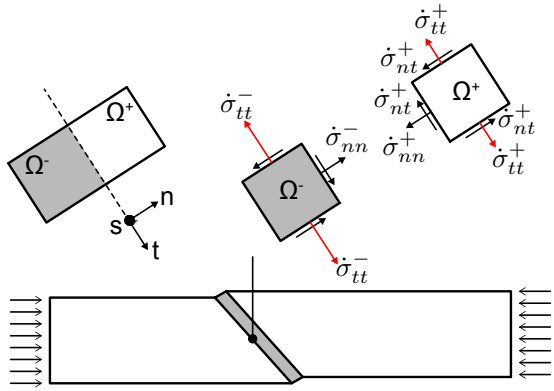

Figure 4.4: Continuum split by a potential discontinuity surface (on the bottom); Infinitesimal volume extracted on the discontinuity (on the top) - red arrows indicate that stress jump can appear in some components, in particular in the out of discontinuity plane components.

the continuity of the displacement rate derivative with respect to the in-plane coordinates of the discontinuity plane (s, t) and the discontinuity of the displacement rate with respect to the normal coordinate (n):

$$\frac{\partial \dot{\mathbf{u}}^+}{\partial t} = \frac{\partial \dot{\mathbf{u}}^-}{\partial t} \tag{4.2}$$

$$\frac{\partial \dot{\mathbf{u}}^+}{\partial s} = \frac{\partial \dot{\mathbf{u}}^-}{\partial s} \tag{4.3}$$

$$\frac{\partial \dot{\mathbf{u}}^+}{\partial n} = \frac{\partial \dot{\mathbf{u}}^-}{\partial n} + \mathbf{g} \tag{4.4}$$

where $\mathbf{g}$ represents a vector measuring the jump.
The spatial gradient of the displacement rate corresponds to its derivative with respect to the position vector $\mathbf{x}$ which, by applying the transformation rules between the local and global coordinates system can be written as:

$$\frac{\partial \dot{\mathbf{u}}^+}{\partial \mathbf{x}} = \frac{\partial \dot{\mathbf{u}}^+}{\partial t} \otimes \frac{\partial t}{\partial \mathbf{x}} + \frac{\partial \dot{\mathbf{u}}^+}{\partial s} \otimes \frac{\partial s}{\partial \mathbf{x}} + \frac{\partial \dot{\mathbf{u}}^+}{\partial n} \otimes \frac{\partial n}{\partial \mathbf{x}} \tag{4.5}$$

which, by considering Eqs. (4.2-4.4), becomes:

$$\frac{\partial \dot{\mathbf{u}}^{+}}{\partial \mathbf{x}} = \frac{\partial \dot{\mathbf{u}}^{-}}{\partial \mathbf{x}} + \mathbf{g} \otimes \mathbf{n}. \tag{4.6}$$

The symmetric part of Eq. (4.6) represents the strain rate in the positive domain, which expression leads to the general form of the compatibility condition in presence of incipient discontinuity:

$$\dot{\boldsymbol{\varepsilon}}_M^{+} = \left(\frac{\partial \dot{\mathbf{u}}^{+}}{\partial \mathbf{x}} \right)_{sym} = \left(\frac{\partial \dot{\mathbf{u}}^{-}}{\partial \mathbf{x}} + \mathbf{g} \otimes \mathbf{n} \right)_{sym} = \dot{\boldsymbol{\varepsilon}}_M^{-} + (\mathbf{g} \otimes \mathbf{n})_{sym}\,. \tag{4.7}$$

The vector $\mathbf{g}$ can be written in the form $\mathbf{g} = \dot{g}\mathbf{m}$ where $\dot{g} = ||\mathbf{g}||$ is the magnitude of the jump term and $\mathbf{m} = \mathbf{g}/\dot{g}$ is a unit first-order tensor called the polarization vector.
The stress and strain rates have to be linked by the constitutive law. Since the strain rates on both sides of the discontinuity are different (imaging, for instance, elastic unloading on the positive side and plastic loading on the negative one), the tangent stiffness tensors can be different as well, thus:

$$\dot{\boldsymbol{\sigma}}_M^{+} = \mathbf{E}_M^{t+} : \dot{\boldsymbol{\varepsilon}}_M^{+} \tag{4.8}$$

$$\dot{\boldsymbol{\sigma}}_M^{-} = \mathbf{E}_M^{t-} : \dot{\boldsymbol{\varepsilon}}_M^{-} \tag{4.9}$$

with $\mathbf{E}_M^{t+}$ and $\mathbf{E}_M^{t-}$ representing the tangent stiffness tensors in the sound region and in the process zone, respectively.
Starting from the traction continuity condition (4.1) and using the compatibility condition (4.7) and the material laws (4.8-4.9), exploiting also the symmetry of the stress rate tensors ($\dot{\boldsymbol{\sigma}}_M \cdot \mathbf{n} = \mathbf{n} \cdot \dot{\boldsymbol{\sigma}}_M$), the following relation is obtained:

$$\mathbf{n} \cdot \mathbf{E}_M^{t+} : \dot{\boldsymbol{\varepsilon}}_M^{-} + \mathbf{n} \cdot \mathbf{E}_M^{t+} : (\mathbf{g} \otimes \mathbf{n})_{sym} = \mathbf{n} \cdot \mathbf{E}_M^{t-} : \dot{\boldsymbol{\varepsilon}}_M^{-}. \tag{4.10}$$

Since $\mathbf{n} \cdot \mathbf{E}_M^{t+} : (\mathbf{g} \otimes \mathbf{n})_{sym} = (\mathbf{n} \cdot \mathbf{E}_M^{t+} \cdot \mathbf{n}) \cdot \mathbf{g}$, Eq. (4.10) can be written in the general form that describes incipient weak discontinuity:

$$\left(\mathbf{n} \cdot \mathbf{E}_M^{t+} \cdot \mathbf{n}\right) \cdot \mathbf{m}\dot{g} = \mathbf{n} \cdot \left(\mathbf{E}_M^{t-} - \mathbf{E}_M^{t+}\right) : \dot{\boldsymbol{\varepsilon}}_M^{-}. \tag{4.11}$$

Considerable simplification is achieved if the tangent stiffness tensors on both sides of the discontinuity are the same, $\mathbf{E}_M^{t+} = \mathbf{E}_M^{t-} = \mathbf{E}_M^{t}$. In this case

the right-hand side in (4.11) vanishes and, since a true discontinuity is obtained only with $\dot{g} \neq 0$, the equation reduces to:

$$\left(\mathbf{n} \cdot \mathbf{E}_M^t \cdot \mathbf{n}\right) \cdot \mathbf{m} = \mathbf{0}. \tag{4.12}$$

The second-order tensor

$$\mathbf{L} = \mathbf{n} \cdot \mathbf{E}_M^t \cdot \mathbf{n} \tag{4.13}$$

is called the *acoustic tensor*. The Eq. (4.12), corresponding to the *continuous bifurcation*, admits a non-trivial solution $\mathbf{m}$ for a direction $\mathbf{n}$ if the acoustic tensor is singular:

$$\det\left(\mathbf{L}\right) = 0. \tag{4.14}$$

From the mathematical point of view, the onset of strain localization coincides with the so-called *loss of ellipticity* of governing equations. In the CH scheme proposed, the tangent stiffness $\mathbf{E}_M^t$ is evaluated at the mesoscale, therefore the strain localization is equivalent to the decohesion phenomena and fractures developing at the block-joint interfaces. The equality to zero guarantees that the tangent stiffness is the elasto-plastic one in both subdomains and the solution is of the loading/loading type.
From Eq. (4.13), it is evident that the acoustic tensor $\mathbf{L}$ depends on the tangent stiffness tensor $\mathbf{E}_M^t$ and on the unit normal to the discontinuity surface $\mathbf{n}$. The former can be considered as dependent on the current state only and thus known. The latter, instead, is not given in advance. Therefore, localization analysis consists in searching for a unit vector $\mathbf{n}$ for which the acoustic tensor becomes singular. If such a vector does not exist, the strains must remain continuous in space. Singularity of the acoustic tensor for a certain vector $\mathbf{n}$ indicates that strain jump can develop across a surface with normal $\mathbf{n}$.
The polarization vector $\mathbf{m}$ reflects the failure mode. If $\mathbf{m}$ is aligned with the normal vector $\mathbf{n}$, the difference between the strain rates inside the band and outside of it corresponds to stretching of the band in the normal direction (Fig. 4.5 (a)). This discontinuous mode is a precursor to splitting failure and is denoted as Mode I. On the other hand, if the polarization vector is normal to vector $\mathbf{n}$, i.e. parallel with the discontinuity planes, the failure occurs by shear slip and this is referred to as Mode II (Fig. 4.5 (b)). For general vectors $\mathbf{m}$,

failure is of a mixed type, and the angle between **m** and **n** indicates whether the failure mode is closer to tensile splitting or to shear slip.

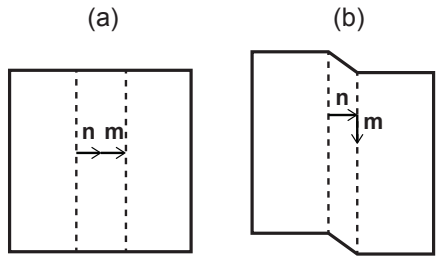

Figure 4.5: Body with a localized band, a) tensile splitting (Mode I), b) shear slip (Mode II).

After plastic band localization, the two portions of the body can be assumed as two different materials, having own tangent stiffnesses. This situation is even called elastic/plastic bifurcation or *discontinuous bifurcation*. The material is loading on one side of the discontinuity plane and unloading on the other side.

4.3.1 1D strain localization problem

The one dimensional example described by Jirásek in [39], consisting in the bar of Fig. 4.6, loaded in tension by a displacement u applied at one of the supports, is considered. The response remains linearly elastic up to $u = u_0 = L\varepsilon_0$ (Fig. 4.7 (a)). At this state, the force F transmitted by the bar reaches its maximum value, $F_0 = A\sigma_0$. After that, in the zone of length L_s (defect), the material shows a softening elasto-plastic response. At each cross section, the stress decreases either at increasing strain, by softening in the process zone with length L_s, or at decreasing strain, by elastic unloading in the sound region, with length L_u equal to $L - L_s$.

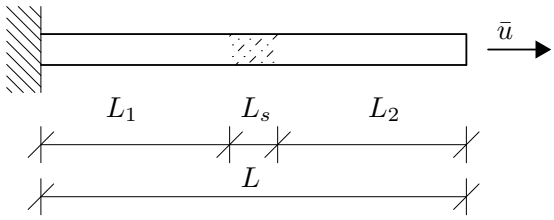

Figure 4.6: Bar under uniaxial tension.

In order to analyze the principal characteristics of the strain localization phenomenon, let us consider the constitutive behavior described by the following linear relations:

$$\sigma = \begin{cases} E\varepsilon & \text{if } 0 \leq \varepsilon \leq \varepsilon_0 \\ S(\varepsilon_f - \varepsilon) & \text{if } \varepsilon_0 \leq \varepsilon \leq \varepsilon_f \\ 0 & \text{if } \varepsilon \geq \varepsilon_f \end{cases} \tag{4.15}$$

where E is Young's modulus of elasticity, S is the parameter governing softening, ε_f is the ultimate strain at which the stress vanishes. The stress distribution is uniform along the bar, however, any stress $\bar{\sigma}$ between zero and σ_0 can be generated by infinitely many strain paths that are in between the two cases - elastic unloading from the peak to strain ε_u, and softening up to strain ε_s (Fig. 4.7 (b)). This means that the strain distribution needs not be uniform and any constant strain distribution that jumps between the two extreme strain values ε_u and ε_s, represents a valid solution. The displacement u_f at the beam end in the post-peak behavior is:

$$u_f = L_u\varepsilon_u + L_s\varepsilon_s \tag{4.16}$$

where the length L_s can be considered a variable assuming any value between zero and L. This means that the problem has infinitely many solutions, and the corresponding post-peak branches of the load-displacement diagram fill the fan shown in Fig. 4.7 (a). Any solution between the one with uniform softening ($u_f = L\varepsilon_f$) and the one with uniform unloading ($u_f = 0$) represents a possible process. It is not immediately obvious which of these solutions is the correct one and reflects the actual failure process. The ambiguity is removed if imperfections are taken into account. In fact the material properties together with the cross sectional dimensions are actually not perfectly uniform along

the bar, and a small region with slower strength can exists. This leads to the conclusion that the size of the softening region is dictated by the size of the region with minimum strength.

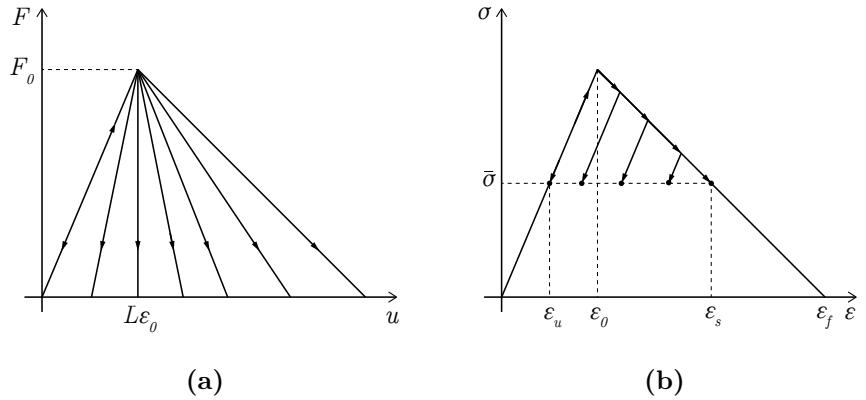

Figure 4.7: Bar under uniaxial tension (a) load-displacement diagram (b) stress-strain diagram with linear softening.

This central issue on the uniqueness of solution in the formulation of strain-softening continuum is related to the so-called *loss of ellipticity* of the governing differential equation. In the present one-dimensional system, loss of ellipticity occurs when the tangent modulus ceases to be positive. The boundary value problem becomes ill-posed, i.e. any change in the data can cause a change in the solution.
Numerically, load-displacement curves for strain localization problems in softening continua display a well documented, pathological mesh-dependence.
In the examined problem, since the stress distribution is uniform, the elastic line equation gives a linear displacement distributions on each of the three domains $\Omega_1 : [0 \leq x \leq L_1]$, $\Omega_2 : [L_1 \leq x \leq L_1 + L_s]$, $\Omega_3 : [L_1 + L_s \leq x \leq L_1 + L_s + L_2]$:

$$u_i(x) = C_{2i-1}\, x + C_{2i} \qquad \text{on}\, \Omega_i \,\text{with}\, i = 1, 2, 3 \tag{4.17}$$

The linear system of Eqs. (4.17) can be solved by considering the following six boundary conditions:

$$u_1(0) = 0 \tag{4.18}$$
$$u_3(L) = \bar{u} \tag{4.19}$$
$$u_1(L_1) = u_2(L_1) \tag{4.20}$$
$$u_2(L_1 + L_s) = u_3(L_1 + L_s) \tag{4.21}$$
$$\sigma_1(L_1) = \sigma_2(L_1) \tag{4.22}$$
$$\sigma_2(L_1 + L_s) = \sigma_3(L_1 + L_s) \tag{4.23}$$

where in Eq. (4.19) $\bar{u}$ is the displacement imposed at the free end of the bar. Equations (4.20), (4.21) and Eqs. (4.22), (4.23) represent the continuity of displacement field and the uniformity of stress distribution, respectively. The Eqs. (4.18-4.22) together with the constitutive Eqs. (4.15) lead to a set of six linear equations, from which it is possible to determine:

$$\varepsilon_1 = \varepsilon_3 = \frac{S(\bar{u} - L_s\varepsilon_f)}{SL_u - EL_s} \qquad \text{on}\,\Omega_1,\,\Omega_3 \tag{4.24}$$

$$\varepsilon_2 = \frac{SL_u\varepsilon_f - E\bar{u}}{SL_u - EL_s} \qquad \text{on}\,\Omega_2 \tag{4.25}$$

which lead to the definition of the strain jump by subtracting Eq. (4.23) from Eq. (4.25):

$$[\varepsilon] = \frac{SL\varepsilon_f - \bar{u}(E + S)}{SL_u - EL_s}. \tag{4.26}$$

Since

$$E\varepsilon_0 = S\left(\varepsilon_F - \varepsilon_0\right), \tag{4.27}$$

it is possible to write the strain jump (4.26) as

$$[\varepsilon] = \frac{\left(\frac{\bar{u}}{L} - \varepsilon_0\right)}{\beta\varepsilon_f - \varepsilon_0}\,\varepsilon_0 \tag{4.28}$$

where β is a coefficient in the range $0 \leqslant \beta \leqslant 1$ equal to $\frac{L_s}{L}$.
The stress evaluated at the end of the bar reads as

$$\sigma = \frac{\beta\varepsilon_f - \frac{\bar{u}}{L}}{\beta\varepsilon_f - \varepsilon_0}\,\sigma_0 \tag{4.29}$$

and it is expected to be a positive quantity. From Eq. (4.29), the tangent modulus of the descending branch in the load displacement diagram can be easily deduced as

$$\frac{dF}{d\bar{u}} = -\frac{F_0}{(\beta\varepsilon_f - \varepsilon_0)\,L}. \tag{4.30}$$

In this sense, two conditions, related to the sign of the slope (4.30), can be distinguished.
Adopting the position that $\bar{\beta} = \frac{\varepsilon_0}{\varepsilon_f}$, to ensure the positivity of σ (Eq. 4.29), the following condition has to hold

$$\text{if } \beta > \bar{\beta}, \Rightarrow \beta\varepsilon_f - \frac{\bar{u}}{L} > 0, \tag{4.31}$$

that is equal to $\bar{u} < L_s\varepsilon_f$, i.e. $L_s\varepsilon_f$ is the limit superior of $\bar{u}$ (see Fig. 4.8 (a)). In this case the tangent modulus (4.30) is negative and the load-displacement diagram is the one shown in Fig. 4.8 (a). Conversely

$$\text{if } \beta < \bar{\beta}, \Rightarrow \beta\varepsilon_f - \frac{\bar{u}}{L} < 0, \tag{4.32}$$

condition that implies the positivity of the slope (4.30), i.e. the load-displacement diagram exhibits a snapback, as shown in Fig. 4.8 (b).
From the two diagrams in Fig. 4.8, it is observed that, when $\beta > \bar{\beta}$, it follows that $\bar{u} > \varepsilon_0 L$. Also, when $\beta < \bar{\beta}$, it follows that $\bar{u} < \varepsilon_0 L$. As a consequence,

Remark 1 *The strain jump* $[\varepsilon]$ *between the process zone and the sound zone is always positive.*

The two coefficients β and $\bar{\beta}$ represent the geometrical and the constitutive parameters that governs the response, $\beta = \bar{\beta}$ represents an undetermined

case correspondent to the situation in which the strain-softening slope becomes vertical.

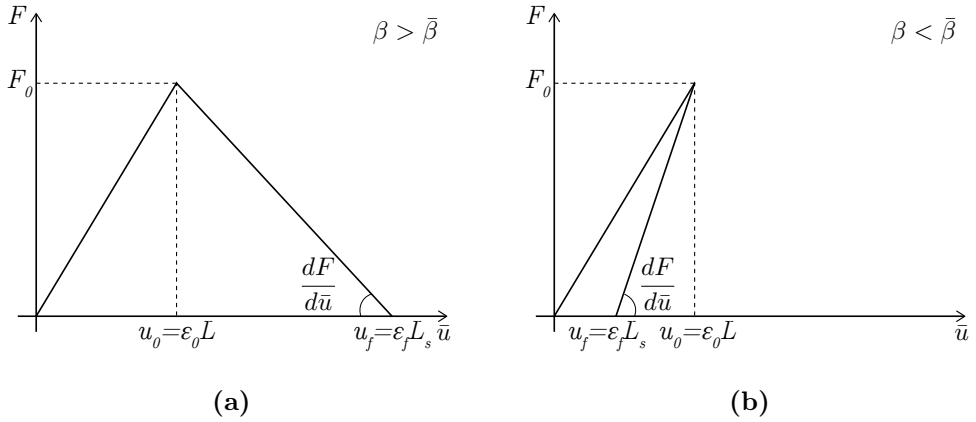

Figure 4.8: Load-displacement diagram in the cases (a) $\beta > \bar{\beta}$ and (b) $\beta < \bar{\beta}$

4.4 Smeared band model

A sort of approximate embedded band model is here considered. The approach is based on the work of Pietruszczak and Mróz [72] who introduced the characteristic dimension of a smeared shear band and its ratio to the finite element dimension, to obtain a certain independence to the discretization in load-displacement response of elasto-plastic strain-softening materials.
The Gauss point volume is split into a localized band of volume Ω^- and the surrounding sound region Ω^+, see Fig. 4.9. Each sub-region is characterized by its volume fraction, f^+ and f^-, with $f^+ + f^- = 1$.

Since the strains in the localized and in the non localized regions are considered homogeneous, the macroscopic strain rate $\dot{\boldsymbol{\varepsilon}}_M$ is the weighted-average of the two strains:

$$\dot{\boldsymbol{\varepsilon}}_M = f^+ \, \dot{\boldsymbol{\varepsilon}}_M^+ + f^- \, \dot{\boldsymbol{\varepsilon}}_M^- . \tag{4.33}$$

It should be noted that the averaging expression (4.33) find its roots in the work of Belytschko et al. [11]. Moreover, Evers et al. [23] computed the macroscopic deformation gradient of a crystal grain by volume-averaging two

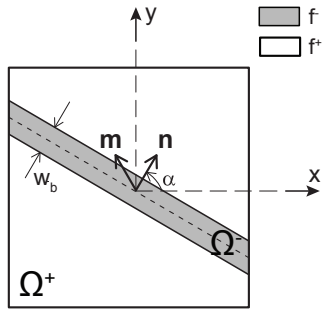

Figure 4.9: Localization in a macroscopic Gauss point, Ω^+ and Ω^- are the volumes of the plastic band and the sound region, f^+ and f^- indicates the two volume fractions, $\mathbf{n}$ is the unit vector normal to the discontinuity plane, $\mathbf{m}$ is the polarization vector, w_b is the band width.

individually uniform deformation gradients relative to the grain core and its boundaries. Massart et al. [58] re-called the work of Evers et al. [23] in their formulation. More recently, Nguyen et al. [64] introduced the same expression and referred to it as an enhancement in the constitutive kinematics. However, it is here emphasized that a correct description of the material behavior in post-localization regime can be obtained.
The strain jump rate can be evaluated as a function of the macroscopic strain rate using Eq. (4.11) and exploiting the strain decomposition (Eq. (4.33)), thus

$$\mathbf{m}\dot{g} = \left[\mathbf{n}\cdot\left(f^-\,\mathbf{E}_M^+ + f^+\,\mathbf{E}_M^{t-}\right)\cdot\mathbf{n}\right]^{-1}\cdot\left(\mathbf{E}_M^{t-} - \mathbf{E}_M^+\right) : \dot{\boldsymbol{\varepsilon}}_M\cdot\mathbf{n}. \tag{4.34}$$

It is noted that $\mathbf{E}_M^{t+} = \mathbf{E}_M^+$, that is the elastic stiffness of the material. As demonstrated by Borré and Maier [13] and Ottosen and Runesson [69], the necessary and sufficient condition for the discontinuous bifurcation is:

$$\det\left[\mathbf{n}\cdot\left(f^-\mathbf{E}_M^+ + f^+\,\mathbf{E}_M^{t-}\right)\cdot\mathbf{n}\right] = \det\left(\mathbf{L}^*\right) \leq 0 \tag{4.35}$$

where $\mathbf{L}^*$ is the acoustic tensor of the loading/unloading solution type, which corresponds to elasto-plastic stiffness tangent $\mathbf{E}_M^{t-}$ on one side of the discontinuity, and elastic stiffness $\mathbf{E}_M^+$ on the other side.
The expression of the strain jump (4.34) can be used to evaluate the strains in the two regions, thus

$$\dot{\boldsymbol{\varepsilon}}_M^- = \left[\mathbf{I} - f^+ \left(\mathbf{n} \otimes \mathbf{L}^{*\,-\mathbf{1}} \otimes \mathbf{n}\right) : \left(\mathbf{E}_M^{t-} - \mathbf{E}_M^+\right)\right] : \dot{\boldsymbol{\varepsilon}}_M \tag{4.36}$$

$$\dot{\boldsymbol{\varepsilon}}_M^+ = \left[\mathbf{I} + f^- \left(\mathbf{n} \otimes \mathbf{L}^{*\,-\mathbf{1}} \otimes \mathbf{n}\right) : \left(\mathbf{E}_M^{t-} - \mathbf{E}_M^+\right)\right] : \dot{\boldsymbol{\varepsilon}}_M \tag{4.37}$$

where $\mathbf{I}$ is the fourth-order unit tensor.
The macro stress can be described by an average form following the mixture theory as for the macro strain [64]

$$\dot{\boldsymbol{\sigma}}_M = f^+ \, \dot{\boldsymbol{\sigma}}_M^+ + f^- \, \dot{\boldsymbol{\sigma}}_M^-. \tag{4.38}$$

Substituting the constitutive Eqs. (4.8) and (4.9) (where $\mathbf{E}_M^{t+} = \mathbf{E}_M^+$) and the obtained expression of the strains in the two regions (4.36) and (4.37) into Eq. (4.38), we can write the constitutive equation at the macroscopic level in the presence of a plastic band equivalent to the fractures developed at the mesoscopic level:

$$\dot{\boldsymbol{\sigma}}_M = \mathbf{E}_M^t : \dot{\boldsymbol{\varepsilon}}_M \tag{4.39}$$

where $\mathbf{E}_M^t$ is the macroscopic tangent stiffness expressed in the following form

$$\begin{aligned} \mathbf{E}_M^t = [&f^+ \, \mathbf{E}_M^+ + f^- \, \mathbf{E}_M^{t-} + \\ &- f^+ \, f^- \left(\mathbf{E}_M^{t-} - \mathbf{E}_M^+\right) : \left(\mathbf{n} \otimes \mathbf{L}^{*\,-\mathbf{1}} \otimes \mathbf{n}\right) : \left(\mathbf{E}_M^{t-} - \mathbf{E}_M^+\right)]. \end{aligned} \tag{4.40}$$

4.4.1 1D smeared strain localization problem

The 1D problem presented in Section 4.3.1 is here particularized considering that the average strain can be expressed as a combination of the inside-band and outside-band strain, following expression (4.33):

$$\varepsilon = \beta \varepsilon_2 + (1 - \beta) \, \varepsilon_1, \tag{4.41}$$

where β is equal to the length fraction of the localized region $\frac{L_s}{L}$, ε_1 and ε_2 represent the inside-band and outside-band strain, respectively. Following the compatibility condition (4.4) the strain jump reads

$$\varepsilon_2 - \varepsilon_1 = \frac{[u]}{L}, \tag{4.42}$$

with $[u]$ representing the displacement jump between the sound and the process zone. From the expressions (4.41) and (4.42), ε_1 and ε_2 can be obtained as a function of the average strain

$$\varepsilon_1 = \varepsilon - \frac{[u]}{L}, \tag{4.43}$$

$$\varepsilon_2 = \varepsilon + \frac{[u]\,(1-\beta)}{\beta L}. \tag{4.44}$$

The stress can be also expressed as the weighted-average of the inside-band and outside-band stresses (Eq. 4.38)

$$\sigma = \beta\sigma_2 + (1-\beta)\,\sigma_1, \tag{4.45}$$

being valid the constitutive conditions of linear elasticity and softening inside and outside the localized zone

$$\sigma_1 = E\varepsilon_1, \tag{4.46}$$

$$\sigma_2 = S\,(\varepsilon_f - \varepsilon_2) \tag{4.47}$$

Substituting the values of ε_1 and ε_2 (4.43-4.44) and the constitutive relations (4.46-4.47) into the condition (4.45), the stress reads

$$\sigma = \beta S\varepsilon_f - [\beta S - (1-\beta)]\,\varepsilon - (1-\beta)\,(E+S)\,\frac{[u]}{L}. \tag{4.48}$$

Using the stress continuity relation $\sigma_1 = \sigma_2$ together with Eqs. (4.43-4.44) and (4.46-4.47), the strain jump can be obtained as

$$\frac{[u]}{L} = \frac{\beta \left[S\varepsilon_f - (E+S)\,\varepsilon \right]}{S\,(1-\beta) - E\beta}, \tag{4.49}$$

and may be introduced in (4.48), yielding

$$\sigma = \frac{ES\,(\varepsilon - \beta\varepsilon_f)}{S - \beta\,(E+S)}. \tag{4.50}$$

In this case the elastic line equation gives a linear displacement distribution on the whole domain $\Omega : [0 \leqslant x \leqslant L]$, under the boundary conditions (4.18-4.19):

$$u(x) = \frac{\bar{u}}{L} x \quad \text{on}\,\Omega. \tag{4.51}$$

Combining relations (4.27), (4.50), and the derivative of (4.51) allows to define the stress along the bar according to

$$\sigma = \frac{\beta\varepsilon_f - \frac{\bar{u}}{L}}{\beta\varepsilon_f - \varepsilon_0}\,\sigma_0 \tag{4.52}$$

that coincides with Eq. (4.29) found for the not regularized strain case. The finding of Eq. (4.52) refers to a 1D case, however it confirms that the smeared band model may lead to a correct prediction of the stress state. Comparison of the displacement and strain solutions for the classical and smeared strain 1D localization problem is provided in Fig. 4.10.

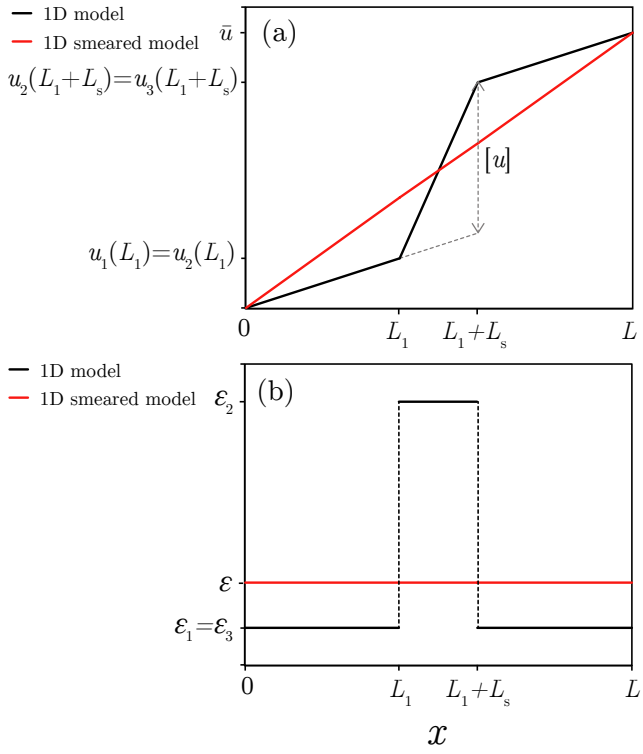

Figure 4.10: Illustration of (a) displacement and (b) strain profiles across the localization band for the 1D models presented in Sections 4.3.1 and 4.4.1.

4.5 Criteria for the assessment of localized band width

In a standard FE localization problem, the simplest way for band width estimation is based on the FE size [40]. If the element is of a square or cubic shape and the band is horizontal or vertical, the square root of the element area in 2D or the cubic root of the element volume in 3D, can be computed. Clearly, this represents a numerical width, not a physical one.
A more sophisticated technique that takes into account the not a priori known orientation of the crack band and can be applied to elements of an arbitrary shape is the so-called *projection method* [9]. The method predicts the band width by projecting the element size in the direction perpendicular to the direction of propagation of the crack, which can be assumed coincident with the direction of the principal maximum strain (Fig. 4.11 (a)).
Another technique was developed by Oliver [68] and is illustrated in Fig. 4.11 (b). The band width w_b is calculated as the reciprocal value of the normal derivative of the function ϕ in the direction $\mathbf{n}$ normal to the band:

$$w_b(\mathbf{x}_j) = \left[\frac{\partial \phi(\mathbf{x}_j)}{\partial n_j}\right]^{-1}, \tag{4.53}$$

where ϕ is a function evaluated at each Gauss point j estimated as:

$$\phi(\mathbf{x}) = \sum_{I=1}^{4} \phi_I N_I(\mathbf{x}) \tag{4.54}$$

with ϕ_I indicating the nodal value and N_I is the FE shape function associated with the node I. The nodal values ϕ_I are assigned when the first Gauss point of the FE is active in terms of localization. The element is hence cut by a straight line passing through the element center and aligned with the expected crack band, perpendicular to the direction $\mathbf{n}_c$ associated with the major principal strain, evaluated at the element center. The function ϕ is set to 0 at the nodes on the side of this line and to 1 on the other side.

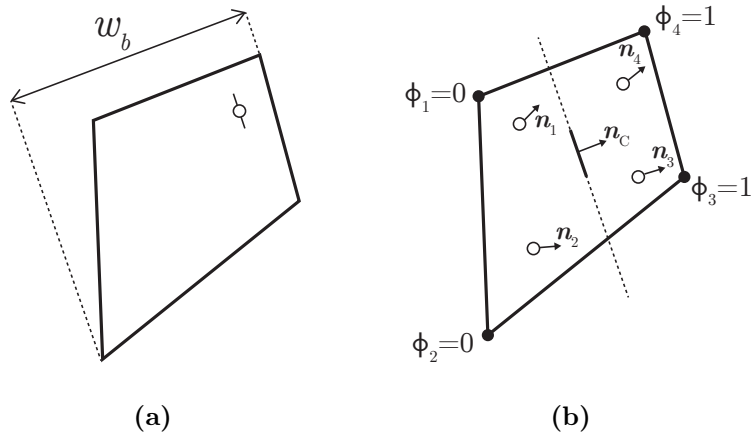

Figure 4.11: Assessment of localized band width w_b based on (a) Projection method [9] (b) Oliver's method [68].

In the case of masonry material, the width of the band depends on the material texture [19, 58]. In a manner consistent with the hypotheses assumed at the mesoscale level, i.e. the fractures propagate along the joints, three reference failure modes are considered. If the fracture propagates along the header and half of the bed joints, proceeding with a square form, the average direction of the plastic band **n** is parallel to the bed joints and its width is equal to half of the UC width, i.e. $w_b = \frac{a}{2}$, with a representing the UC width (Fig. 4.12 (a)). If the fracture propagates along the header and half of the bed joints proceeding with a zigzag form, the average direction of the plastic band corresponds to the direction β resulting from the ratio between half of the UC width, a, and the UC height, b. In this case the band width w_b results equal to $w_b = \frac{ab}{\sqrt{a^2+4b^2}}$ (Fig. 4.12 (b)). Lastly, if the fracture propagates along the bed joints, the direction of the band is the same of the header joints and its width corresponds to the thickness of the mortar joints, h, i.e. $w_b = h$ (Fig. 4.12 (c)).
For numerical purposes, the band width needs to be evaluated also in the positions intermediate with respect to the three reference ones. Thus, a linear interpolation of the band width as a function of the band direction is considered, as shown in Fig. 4.13.

$$w_b = \begin{cases} \frac{a}{2} & \text{if } \alpha = 0° \\ \frac{ab}{\sqrt{a^2+4b^2}} & \text{if } \alpha = \beta = \arctan\left(\frac{a}{2b}\right) \\ h & \text{if } \alpha = 90° \end{cases} \tag{4.55}$$

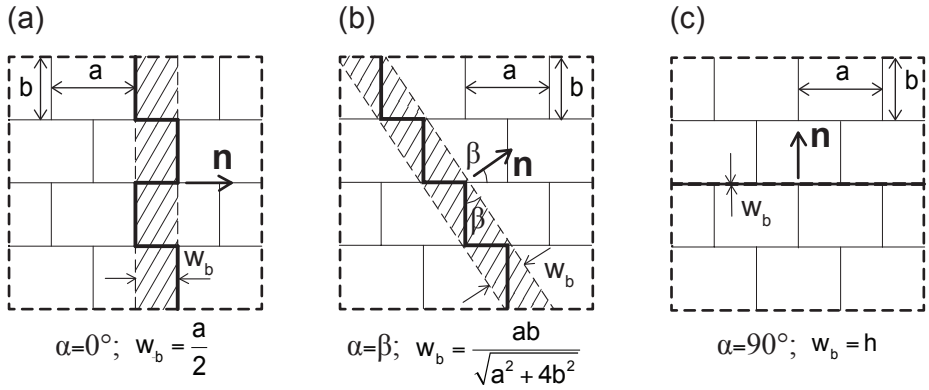

Figure 4.12: Values of the band width as a function of the band direction **n**.

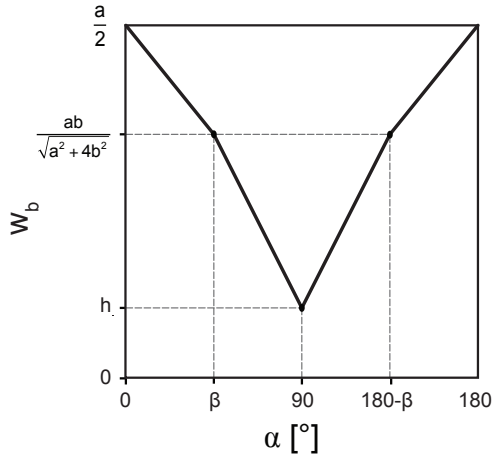

Figure 4.13: Average crack directions defined by their normal **n** and related band width w_b for three fundamental failure patterns: (a) square form crack involving both bed and header joints (b) zigzag form crack involving both bed and header joints (c) linear form crack involving the bed joints.

4.6 Computational aspects

4.6.1 Not localized deformation

The value of the macroscopic stress increment at the sample point of the FE model is calculated by applying the meso-to-macro transition Eq. (2.11) which in matrix notation takes the following form:

$$\boldsymbol{\sigma}_{M_{n+1}} = \frac{1}{\Omega_{UC}} \int\limits_{\Gamma_{UC}} \mathbf{D}_m^T \mathbf{r}_{n+1}\, d\Gamma = \frac{1}{\Omega_{UC}} \sum_{k=1}^{4} \int\limits_{\Gamma_k} \mathbf{D}_m^T \boldsymbol{\Phi}_i \bar{\mathbf{S}}_i d\Gamma\, \mathbf{R}_{n+1} = \frac{1}{\Omega_{UC}} \mathbf{Q}\, \mathbf{R}_{n+1}. \tag{4.56}$$

If in the considered time step the UC response is purely elastic recalling Eq. (3.71), taking in to account the condition $\Delta \mathbf{F}_p = \mathbf{0}$ and the compatibility Eq. (3.82), we obtain the stress-strain relation at the macro-level

$$\boldsymbol{\sigma}_{M_{n+1}} = \frac{1}{\Omega_{UC}} \mathbf{Q}\, \mathbf{B}_{22} \mathbf{Q}^T \boldsymbol{\varepsilon}_{M_{n+1}}, \tag{4.57}$$

and the elastic matrix of the homogenized material is:

$$\mathbf{E}_M = \frac{1}{\Omega_{UC}} \mathbf{Q}\, \mathbf{B}_{22} \mathbf{Q}^T. \tag{4.58}$$

Otherwise in the presence of the UC elasto-plastic response, the substitution of Eq. (3.71) in Eq. (4.56), taking into account the compatibility Eq. (3.82), gives

$$\boldsymbol{\sigma}_{M_{n+1}} = \frac{1}{\Omega_{UC}} \mathbf{Q}\, \mathbf{B}_{22} \mathbf{Q}^T \boldsymbol{\varepsilon}_{M_{n+1}} + \frac{1}{\Omega_{UC}} \mathbf{Q}\, \mathbf{B}_{21}\, \mathbf{F}_{p_{n+1}}. \tag{4.59}$$

The consistent tangent stiffness can be evaluated in the classical way:

$$\left.\frac{\mathrm{d}\boldsymbol{\sigma}_M}{\mathrm{d}\boldsymbol{\varepsilon}_M}\right|_{n+1} = \frac{1}{\Omega_{UC}} \mathbf{Q}\, \mathbf{B}_{22} \mathbf{Q}^T + \frac{1}{\Omega_{UC}} \mathbf{Q}\, \mathbf{B}_{21}\, \left.\frac{\mathrm{d}\mathbf{F}_p}{\mathrm{d}\boldsymbol{\varepsilon}_M}\right|_{n+1}. \tag{4.60}$$

Considering the definition (3.65) of the plastic forces and using the chain rule, we have

$$\left.\frac{\mathrm{d}\mathbf{F}_p}{\mathrm{d}\boldsymbol{\varepsilon}_M}\right|_{n+1} = \sum_{k=1}^{4} \int\limits_{\Gamma_k} \left(\boldsymbol{\Phi}_i \mathbf{S}_i - \boldsymbol{\Phi}_b \mathbf{S}_b\right)^T \mathbf{T}_i^T \mathbf{E}_i\, \left.\frac{\mathrm{d}\left[\mathbf{u}_{mi}\right]^p}{\mathrm{d}\left[\mathbf{u}_{mi}\right]}\right|_{n+1} \left.\frac{\mathrm{d}\left[\mathbf{u}_{mi}\right]}{\mathrm{d}\boldsymbol{\varepsilon}_M}\right|_{n+1} \mathrm{d}\Gamma \tag{4.61}$$

and it can be simplified considering the interface compatibility conditions $(3.56)_b$ and the definition of interface consistent tangent (3.109), thus

$$\left.\frac{\mathrm{d}\mathbf{F}_p}{\mathrm{d}\boldsymbol{\varepsilon}_M}\right|_{n+1} = \left(\mathbf{K} - \mathbf{K}^{ct}_{i_{n+1}}\right) \left.\frac{\mathrm{d}\mathbf{U}_m}{\mathrm{d}\boldsymbol{\varepsilon}_M}\right|_{n+1}. \tag{4.62}$$

Finally, differentiating the solution of the meso-model in terms of nodal displacements (3.70) with respect to the macro-strain, substituting the derivative in the expression (4.62) and inserting the results in Eq. (4.60) we obtain the consistent tangent stiffness for the case of non localized deformation:

$$\mathbf{E}^{ct}_M = \mathbf{E}_M + \frac{1}{\Omega_{UC}} \mathbf{Q}\,\mathbf{B}_{21} \left[\mathbf{I} - \left(\mathbf{K} - \mathbf{K}^{ct}_{i_{n+1}}\right)\mathbf{B}_{11}\right]^{-1} (\mathbf{K} - \mathbf{K}^{ct}_{i_{n+1}})\mathbf{B}_{12}\mathbf{Q}^T. \tag{4.63}$$

4.6.2 Localized deformation

Let us consider the case of localized deformation occurred at the time step $[t_n, t_{n+1}] \subset [0, T]$, so that at the beginning of the time step at the macro level the following variables are known

$$\left\{\boldsymbol{\varepsilon}^-_{M_n},\, \mathbf{g}_n,\, \mathbf{E}^{t-}_{M_n},\, \mathbf{C}^T_{n_n},\, f^-_n\right\}, \tag{4.64}$$

where $\mathbf{C}^T_{n_n}$ is the matrix projecting the stress state on the plastic band plane having normal $\mathbf{n}_n$.The state of stress in the plastic band and in the sound material and the macroscopic stress can be regarded as dependent variables evaluated from Eqs. (4.8), (4.9) and (4.39).
Assigned the increment of the macroscopic deformation $\Delta\boldsymbol{\varepsilon}_M$, the basic problem is to update the variables (4.64) at t_{n+1} in a manner consistent with the response of the UC. The equilibrium equations (4.1), the compatibility equations (4.6), the constitutive laws (4.8-4.9), resulting in the incipient weak discontinuity condition (4.11), define a rate nonlinear evolution problem with initial conditions (4.64) that can be transformed into a discrete form applying the typical procedures of computational inelasticity.
In particular, integrating in the time step the two conditions (4.1) and (4.6) we obtain

$$\mathbf{C}^T_{n_{n+1}} \left(\boldsymbol{\sigma}^-_{M_{n+1}} - \boldsymbol{\sigma}^+_{M_{n+1}}\right) = \mathbf{0}, \tag{4.65}$$

$$\Delta\boldsymbol{\varepsilon}^+_M - \Delta\boldsymbol{\varepsilon}^-_M = \mathbf{C}_{n_{n+1}} \Delta\mathbf{g}. \tag{4.66}$$

Exploiting the constitutive Eqs. (4.8)-(4.9) and the Taylor condition (4.11) written in an incremental form, the increment of strain jump can be evaluated:

$$\Delta\mathbf{g} = \mathbf{L}^{*\,-1}_{n+1}\,\mathbf{C}^{T}_{n_{n+1}}\left(\mathbf{E}^{t-}_{M_{n+1}} - \mathbf{E}^{+}_{M}\right)\left(\Delta\boldsymbol{\varepsilon}_M + \Delta\widehat{\boldsymbol{\varepsilon}}_M\right), \tag{4.67}$$

where the following position has been introduced

$$\boldsymbol{\sigma}^{-}_{M_n} - \boldsymbol{\sigma}^{+}_{M_n} = \left(\mathbf{E}^{t-}_{M_{n+1}} - \mathbf{E}^{+}_{M}\right)\Delta\widehat{\boldsymbol{\varepsilon}}_M. \tag{4.68}$$

The term $\Delta\widehat{\boldsymbol{\varepsilon}}_M$ appearing in (4.68) has the mechanical meaning of a fictitious increment of the macroscopic strain which results from the tractions continuity at the plastic band-sound material interface in the presence of a rotating band. It is to remark that the concept of plastic band equivalent to the mesoscopic fracture pattern admits the possibility of changing its direction and the rotation avoids locking phenomena along the loading process.
The strain increments can be therefore calculated for the two regions as:

$$\Delta\boldsymbol{\varepsilon}^{-}_{M} = \Delta\boldsymbol{\varepsilon}_M - f^{+}_{n+1}\left(\mathbf{C}_{n_{n+1}}\mathbf{L}^{*-1}_{n+1}\mathbf{C}^{T}_{n_{n+1}}\right)\left(\mathbf{E}^{t-}_{M_{n+1}} - \mathbf{E}^{+}_{M}\right)\left(\Delta\boldsymbol{\varepsilon}_M + \Delta\widehat{\boldsymbol{\varepsilon}}_M\right) \tag{4.69}$$

$$\Delta\boldsymbol{\varepsilon}^{+}_{M} = \Delta\boldsymbol{\varepsilon}_M + f^{-}_{n+1}\left(\mathbf{C}_{n_{n+1}}\mathbf{L}^{*-1}_{n+1}\mathbf{C}^{T}_{n_{n+1}}\right)\left(\mathbf{E}^{t-}_{M_{n+1}} - \mathbf{E}^{+}_{M}\right)\left(\Delta\boldsymbol{\varepsilon}_M + \Delta\widehat{\boldsymbol{\varepsilon}}_M\right) \tag{4.70}$$

The Eqs. set (4.65÷4.68) is iteratively solved making use of the Newton-Raphson procedure until Eq. (4.65) is satisfied. At the end of each iteration, the response of the UC, the plastic band direction, the respective volume fraction, the tangent stiffness and the macroscopic stress are evaluated.
At the end of the iterative procedure, the total macroscopic stress increment can be calculated integrating Eq. (4.38) in the time step and substituting the result (4.67), thus

$$\begin{aligned}\Delta\boldsymbol{\sigma}_M = &\left(f^{+}_{n+1}\mathbf{E}^{+}_{M} + f^{-}_{n+1}\mathbf{E}^{t-}_{M_{n+1}}\right)\Delta\boldsymbol{\varepsilon} + \\ -f^{+}_{n+1}f^{-}_{n+1}&\left(\mathbf{E}^{+}_{M} - \mathbf{E}^{t-}_{M_{n+1}}\right)\mathbf{C}_{n_{n+1}}\mathbf{L}^{*-1}_{n+1}\mathbf{C}^{T}_{n_{n+1}}\left(\mathbf{E}^{+}_{M} - \mathbf{E}^{t-}_{M_{n+1}}\right)\left(\Delta\boldsymbol{\varepsilon}_M + \Delta\widehat{\boldsymbol{\varepsilon}}_M\right).\end{aligned} \tag{4.71}$$

The expression of the linearized macroscopic tangent stiffness is adopted in the present study and it is evaluated from the Eq. (4.71) considering the material parameters and the fictitious strain increment independent on the macroscopic increment of strain:

$$\mathbf{E}^{t}_{M_{n+1}} = \left(f^{+}_{n+1}\mathbf{E}^{+}_{M} + f^{-}_{n+1}\mathbf{E}^{t-}_{M_{n+1}} \right) \Delta\boldsymbol{\varepsilon}_{M} + \\ - f^{+}_{n+1} f^{-}_{n+1} \left(\mathbf{E}^{+}_{M} - \mathbf{E}^{t-}_{M_{n+1}} \right) \mathbf{C}_{n_{n+1}} \mathbf{L}^{*-1}_{n+1} \mathbf{C}^{T}_{n_{n+1}} \left(\mathbf{E}^{+}_{M} - \mathbf{E}^{t-}_{M_{n+1}} \right). \quad (4.72)$$

The iterative procedure is illustrated in detail in Fig. 4.14. If the Taylor condition of Eq. (4.35) is satisfied, a weak discontinuity surface, characterized by the unit vectors $\mathbf{n}$ and $\mathbf{m}$, crosses the Gauss point volume, i.e. $0 < f^{-} \leq 1$, and the macroscopic strain increment is divided in $\Delta\boldsymbol{\varepsilon}^{+}_{M}$ (outside the plastic band) and $\Delta\boldsymbol{\varepsilon}^{-}_{M}$ (inside the plastic band). The stress increment inside the process zone $\Delta\boldsymbol{\sigma}^{-}_{M}$ is evaluated solving the BVP with imposed $\Delta\boldsymbol{\varepsilon}^{-}_{M}$ strain increment. The stress increment $\Delta\boldsymbol{\sigma}^{+}_{M}$ is instead obtained considering the elastic unloading in the sound region. The macroscopic stress increment $\Delta\boldsymbol{\sigma}_{M}$ and the material tangent stiffness matrix $\mathbf{E}^{t}_{M}$ can be evaluated on the basis of Eqs. (4.71) and (4.72). The iterations are kept until satisfying traction continuity condition:

$$\left| \mathbf{C}^{T}_{n_{n+1}} \left(\boldsymbol{\sigma}^{-}_{M_{n+1}} - \boldsymbol{\sigma}^{+}_{M_{n+1}} \right) \right| < tol. \quad (4.73)$$

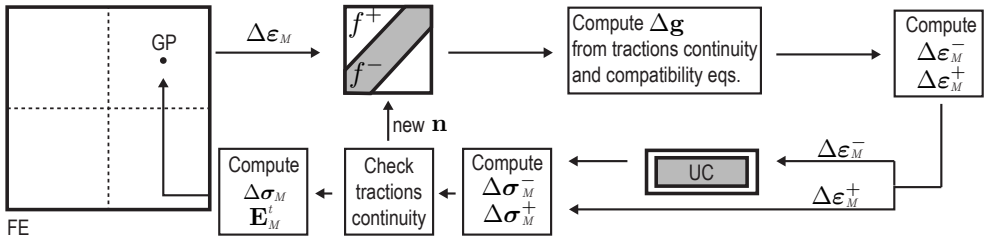

Figure 4.14: Flowchart of macroscopic strain localization at the quadrature point.

4.7 Numerical examples

4.7.1 UC stretching test

The response of the UC under the two displacement conditions showed in Fig. 4.15 is analyzed. The UC is composed by a brick having length equal to 204 mm and height equal to 50 mm, surrounded by a mortar layer of thickness equal to 5 mm. The mechanical parameters adopted for the two materials are reported in Tab. 4.1, where E is the Young's modulus, ν is the Poisson's ratio, c_0 and σ_0 are the cohesive and tensile strength, h_p is the hardening-softening parameter, φ and δ are the friction and dilatancy angles.

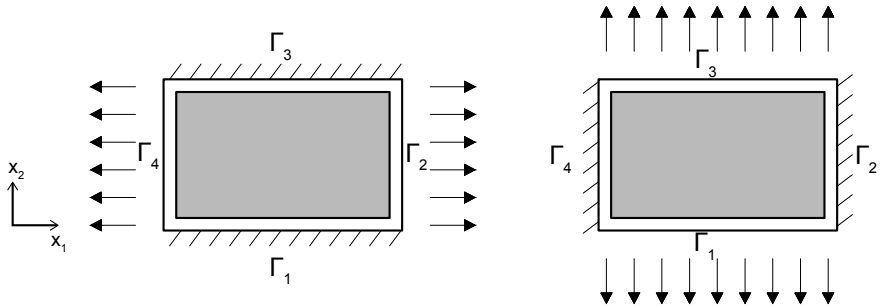

Figure 4.15: Boundary conditions imposed to the UC for the stretching tests.

Parameters	$E\ [MPa]$	ν	$c_0\ [MPa]$	$\sigma_0\ [MPa]$	$h_p\ [MPa^-1]$	$\varphi\ [^o]$	$\delta\ [^o]$
Mortar	820	0.14	0.35	0.25	5	37	$2/3\ \varphi$
Blocks	16700	0.15	–	–	–	–	–

Table 4.1: Block and mortar mechanical properties.

In the first case, showed in the left side of Fig. 4.15, the boundaries Γ_2 and Γ_4 are forced to move along the x_1 direction. As a consequence, the inner block is stretched and this condition results in a biaxial tensile stress condition. Similar mode is applied on the boundaries Γ_1 and Γ_3 along the x_2 direction (right side of Fig. 4.15). In Fig. 4.16 (a) the UC average stress versus average strain is reported for the stretching test along x_1. Different stages can be distinguished. At the beginning the response is elastic. The slope of curve changes at around 0.8 MPa (point 1). This stage corresponds with the development of plasticity on the vertical interfaces. By increasing the strain, plasticity develops also

on the horizontal interfaces until maximum stress is reached (point 2). After point 2, a softening branch is observable until point 4, where a residual stress is recorded due to the UC confinement. The anisotropic behavior of the UC is readable for the stress-strain diagram obtained for the tensile strength along x_2 direction Fig. 4.16 (b). The elastic phase is kept until 0.18 MPa (point 1). At this stage, plasticity starts developing on the horizontal interfaces. After reaching the maximum stress at about 0.25 MPa, softening residual stresses are recorded. The top array of Fig. 4.17 describes the evolution of plasticity in the Gauss points of the UC. A color map is associated to the value of χ_p in the range 0 to 1 and it is displayed for the mortar joints, as the brick behaves elastically. The directions and the orientations of vectors $\mathbf{n}$ and $\mathbf{m}$ show that in the case of pure horizontal or vertical strain applied, the localization occurs in mode I.

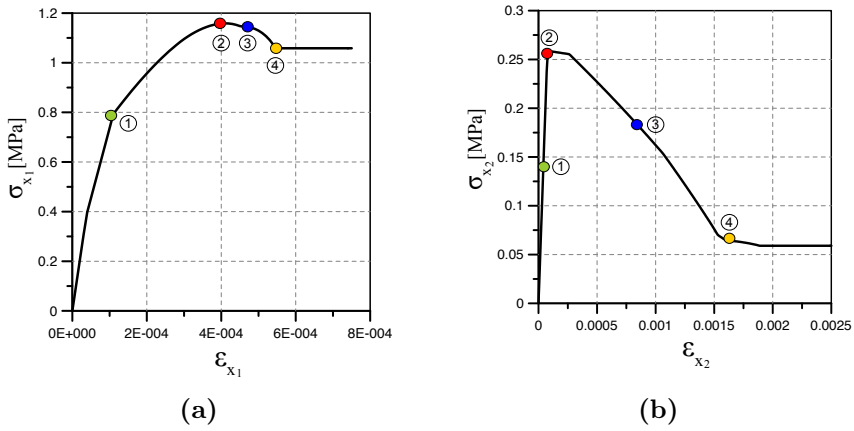

Figure 4.16: Macroscopic stress - strain diagrams for stretching test (a) along x_1 and (b) along x_2.

The results of the localization procedure is also showed in Fig. 4.18. Figure 4.18(a) and (b) refers to the determinant of the acoustic tensor and to the associated minimum eigenvalue, as a function of the possible direction of $\mathbf{n}$, α, when the applied strain is in the horizontal direction x_1. Different colors are referring to the different stress stages, indicated in Fig. 4.16. The acoustic tensor keeps a positive determinant until the maximum stress is reached and no localization can be detected before that value. Once the maximum load is reached, the Tay-

lor condition (4.35) is satisfied for $0° \leqslant \alpha \leqslant 60° \div 65°$. However the minimum eigenvalue is obtained for $\alpha = 0°$ (Fig. 4.18(b)). Eigenvector analysis of (L) matrix furnishes a polarization vector aligned with $\mathbf{n}$, that confirms the mode I failure of the UC.
Figure 4.18(c) and (d) provide the same plots in the case of applying strain along the vertical direction x_2.

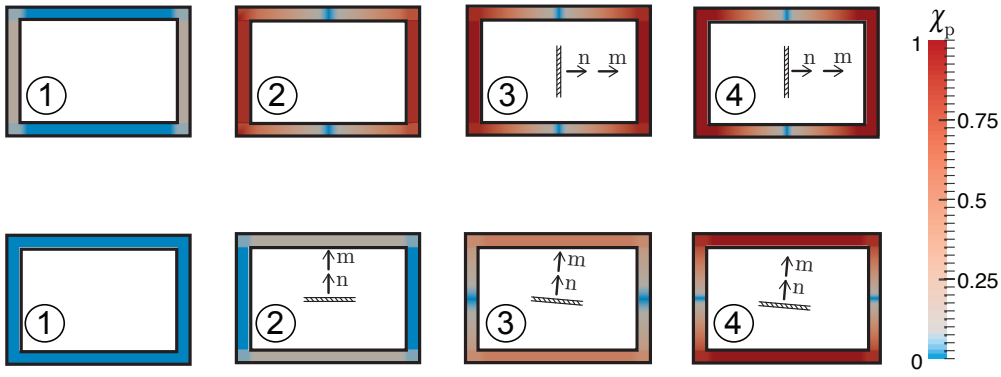

Figure 4.17: Stretching test: map of the static internal variable χ_p in correspondence to the interfacial gauss points. Top array refers to the stretching test along x_1, bottom array refers to the stretching test along x_2.

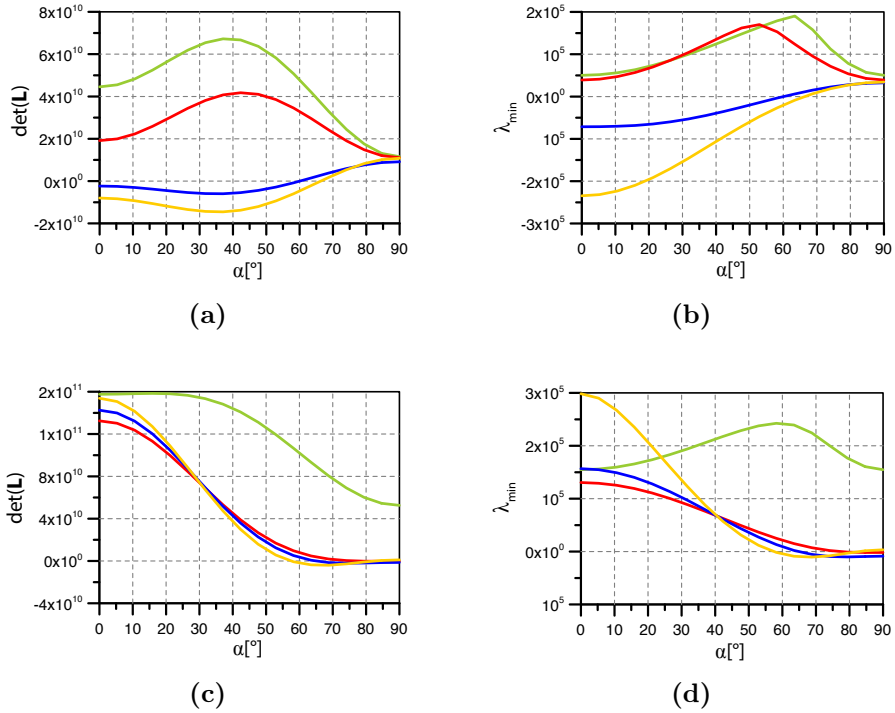

Figure 4.18: Stretching test along x_1: (a) Determinant of the acoustic tensor and (b) minimum eigenvalue for different configurations of **n** vector. Stretching test along x_2: (c) Determinant of the acoustic tensor and (d) minimum eigenvalue for different configurations of **n** vector.

4.7.2 UC shear test

When subjected to a monotonically increasing shear strain (Fig. 4.19), plasticity appears at the two opposite corners of the UC due to shear stresses developing at each interfacial Gauss point. The average stress-strain response is nonlinear and evolves from an elastic stage towards a residual line governed by Mohr-Coulomb limit condition and dilatancy angle (Fig. 4.20). It is important to highlight that after the localization procedure the **n** direction is close to the one of the diagonal of the UC, while the polarization vector **m** evolves as the strain increases. In particular, at the first stages the direction of **m** is closer to the direction of **n**, while at later stages the two vectors are almost perpendicular. In this case, the failure mode can be classified as a mixed type

with a tendency to become mode II (Fig. 4.21 (a)-(d)). The angles of **n** and **m** vectors with respect to the x_1 axis at configuration 4 of Fig. 4.20 are equal to 15.9° and 86.4°, respectively. In Fig. 4.22, the determinant of the acoustic tensor and the minimum eigenvalue *vs.* the orientation of the plastic band α are reported.

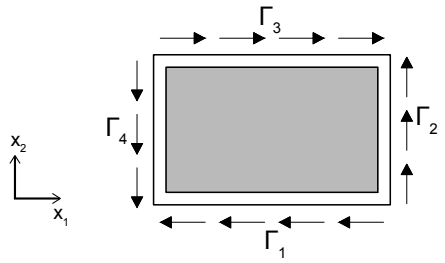

Figure 4.19: Boundary conditions imposed to the UC for the shear test.

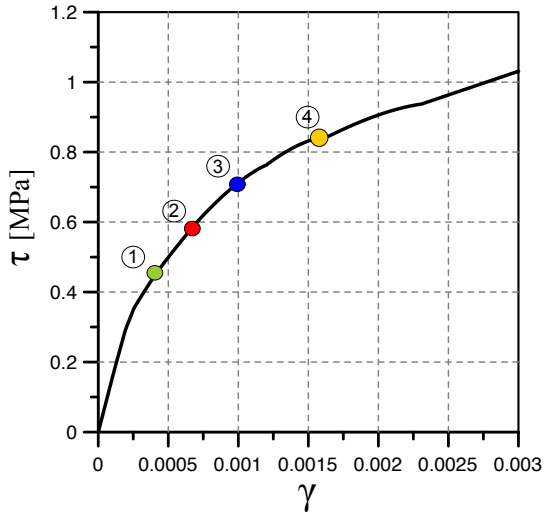

Figure 4.20: Macroscopic stress - strain diagram for shear test.

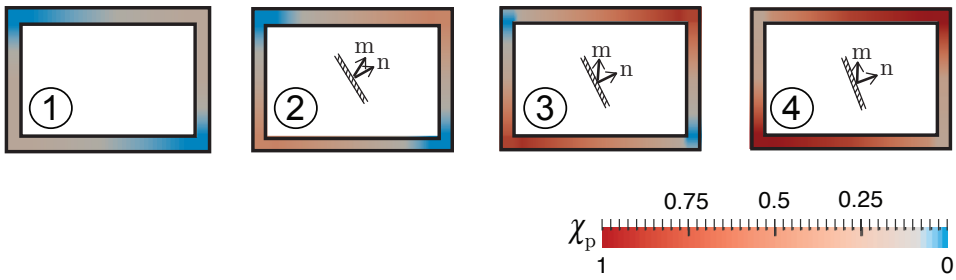

Figure 4.21: Shear test: map of the static internal variable χ_p in correspondence to the interfacial gauss points.

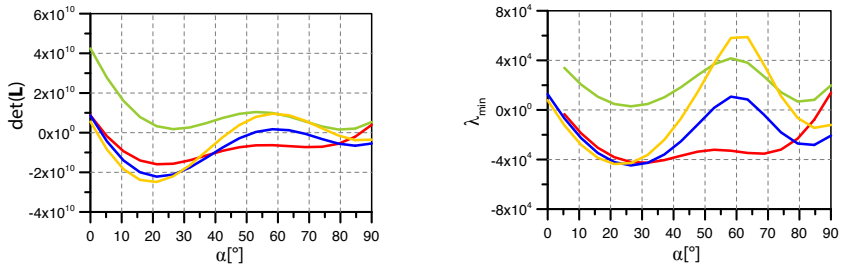

(a) **(b)**

Figure 4.22: Shear test: (a) Determinant of the acoustic tensor and (b) minimum eigenvalue for different configurations of **n** vector.

Chapter 5

Applications

5.1 Introduction

The following chapter is focused on the numerical applications performed by considering the whole FE·Meshless computational strategy. The analyses are circumscribed to those masonry structures where the hypotheses of plane-stress is valid.
The complete numerical procedure is summarized in Section 5.2. Section 5.3 reproduces the numerical example proposed by Massart et al. [58] regarding the in-plane shear response of a hollow masonry panel. The aim of the this example is to test the proposed formulation with respect to a numerical case study available in the literature.
Section 5.4 and 5.5 replicate the experimental tests on a solid and hollow masonry element carried out by Raijmakers and Vermeltfoort et al. [74], as additional validation tests with well-known experimental results. It should be remarked that most of the masonry specimens subjected to experimental tests reported in literature have characteristic dimensions smaller than the ones effectively adopted in the common engineering practice. For this reason, the principle of separation of scales may be easily violated unless opportunely modifying the masonry texture. Hence, block and joint dimensions were sometimes opportunely scaled with respect to the effective ones, in order to properly apply the multi-scale analysis. The results are discussed from the qualitative and quantitative point of view, considering this adjustment. Section 5.6 shows an analysis performed on a wall of a valuable building to estimate a foundation settlement that caused a failure.
All the numerical examples have been carried out using an open source research

oriented finite element analysis program (FEAP). 2D solid element has been adopted for the macroscopic discretization and a new "user material" subroutine has been introduced to solve the UC BVP.
All the examples employ the UC of Fig. 3.8 associated to the minimal discretization, i.e. 17 nodes, with linear BCs.

5.2 Numerical procedure

The complete numerical procedure is summarized in the Box 1. Three nested iterative procedures are employed: one for the macroscopic classical finite element solution, one for the macroscopic strain localization at the quadrature point, one for the UC response evaluation.
With reference to the macroscopic level loop, at $t = 0$, the elastic stiffness matrix of the homogenized material is evaluated. At the generic time step $[t_n, t_{n+1}] \subset [0, T]$, the increment of the macroscopic strain at a single Gauss point of the homogenized structure is obtained. In the quadrature point loop, if localization does not occur, the entire macroscopic strain increment is imposed to the UC and the resultant stress increment is attributed to the macroscopic Gauss point. In case of activation of localization a weak discontinuity surface crosses the Gauss point volume and the macroscopic strain increment is divided in the two portions associated to the plastic band and to the surrounding bulk material, respectively. The stress increments are therefore calculated for the two regions and the macroscopic stress is evaluated by averaging on the volume pertaining to the macroscopic Gauss point.
In the mesoscopic level loop, in particular, the stress increment of the localized zone is evaluated solving the BVP with the imposition of the appropriate strain increment relative to the portion inside the band. The stress increment outside the band is instead obtained considering the elastic unloading in the sound region. At the same time, the solution of the BVP on the UC permits to derive the updated macroscopic tangent stiffness matrix $\mathbf{E}^t_{M_{n+1}}$ at the Gauss point.
At the macroscopic level loop the consistent finite element tangent stiffness matrix and the internal force vector is obtained up to global convergence.

MACROSCOPIC LEVEL LOOP

1. Macro-level FE mesh initialization: evaluate $\mathbf{E_M}$ matrix (Eq. (4.58)).
2. Meso-level UC Meshless initialization: evaluate $\mathbf{K}$ and $\mathbf{G}$ matrices (Eqs. (3.63)-(3.64)).
3. Evaluate the increment of nodal displacements.
4. Evaluate $\Delta\boldsymbol{\varepsilon}_M$ at the Gauss point.

QUADRATURE POINT LOOP

5. Evaluate $\Delta\boldsymbol{\varepsilon}_M^-$ and $\Delta\boldsymbol{\varepsilon}_M^+$ (Eqs. (4.69-4.70)).
6. Macro-to-meso transition (UC in the plastic band): $\Delta\bar{\mathbf{U}}_m = \mathbf{Q}^T\Delta\boldsymbol{\varepsilon}_M^-$.

MESOSCOPIC LEVEL LOOP

7. BVP solution for a purely elastic load step. Elastic predictor stage.
8. Plasticity activation check: if activated continue, otherwise go to 17.
9. Plastic corrector stage. Evaluate $\boldsymbol{\mathcal{E}}$ and $\mathbf{K}^t$ matrix.
10. BVP solution for a plastic load step. Evaluate $\Delta\mathbf{d}$.
11. Repeat steps 8 to 10 until $|\boldsymbol{\mathcal{E}}| < tol$.
12. Extrapolate the UC consistent tangent stiffness matrix $\mathbf{K}^{ct}$ (Eq. (3.110)).

13. Check localization condition (Eq. (4.35)). If it is verified, continue, otherwise go to Step 17.
14. Activate the localization procedure. Look for $\mathbf{n}$ and $\mathbf{m}$ vectors.
15. Calculate w_b, l_b and f^- .
16. Repeat steps 5 to 15 until $\left|\mathbf{C}_{n_{n+1}}^T\left(\boldsymbol{\sigma}_{M_{n+1}}^- - \boldsymbol{\sigma}_{M_{n+1}}^+\right)\right| < tol$.
17. Evaluate average stress vector $\Delta\boldsymbol{\sigma}_M$ and material tangent stiffness matrix $\mathbf{E}_M^t$. (Eqs. (4.71-4.72)).

18. Calculate finite element tangent stiffness matrix and internal force vector.
19. Repeat steps 3 to 18 until convergence of macro-model Newton-Raphson procedure.

Box 1: Numerical procedure.

5.3 Hollow masonry wall - numerical comparison

The masonry wall analyzed by Massart et al. [58] has dimensions 2500× 3000 × 100 mm. An opening with dimensions 800 × 1200 mm is located around the centre as shown in Fig. 5.1. Masonry material is composed by bricks 90 × 30 × 100 mm with 10 mm thick mortar joints. The top and bottom boundaries of the wall are clamped. The load is applied in two stages. In the first stage, the wall is compressed by a uniformly distributed load imposed on the top boundary of the wall. In the second one, maintaining constant the distributed compressive load, a monotonically increasing horizontal shear force is applied at the top right corner.

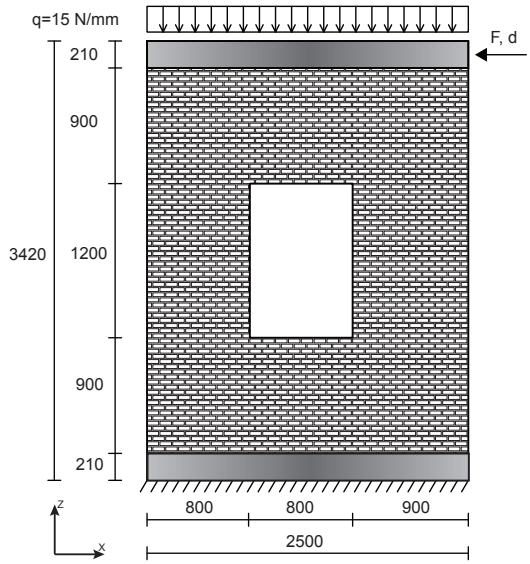

Figure 5.1: Hollow masonry wall - numerical comparison: geometry and boundary conditions of the masonry specimen analyzed by Massart et al. [58]. Geometrical dimensions are expressed in millimeters.

The procedure used in [58] belongs to the FE^2 approach and a maximum principal stress criterion is used for the brick material and a Drucker-Prager criterion with a compressive cap is used for mortar at the mesoscale. The multi-scale analysis is performed under the plane stress condition and the results provided consist in the shear load F - horizontal displacement d history and in

the stress maps with the positions of the embedded cracks.
In the present example the macroscopic finite element model reproduces the one adopted in [58] making use of 48 two-dimensional eight-noded elements with four Gauss integration points. The UC is mesh-free with 17 nodes, leading to a strong reduction of the degrees of freedom with respect to those involved in the Massart's et al. [58] mesoscopic model. As mentioned in the previous chapters, the brick is assumed elastic while the mortar joints have an elastic-plastic behavior. The values of elastic and inelastic properties of the block and of the joints are reported in Table 5.1.
The numerical results obtained in terms of shear load F as a function of the horizontal displacement d are shown in Fig. 5.2. A linear elastic behavior is observed until F reaches the value of 16.5 kN, after that a nonlinear behavior is recorded, which results in the prompt variation of the slope. The results obtained according to the proposed procedure are overlapped to the ones found in [58]. A very good agreement is observed both for the linear and nonlinear branches. It should be noted that the computation performed by Massart et al. [58] was continued until loss of convergence, as a consequence the post peak behavior was not traced. Differently, in the present procedure convergence is always kept and the slope remains unchanged since masonry failure does not take place around the corners of the wall where relevant compression stresses occur and the overall behavior becomes indefinitely elastic.
In Fig. 5.3 the vertical stresses, σ_z, and the plastic bands position related to the steps named A, B, C (Fig. 5.2) are presented. The macroscopic stresses plot is associated to the wall deformed shape, which is amplified by a factor of 500. The presence of the opening strongly influences the distribution of the stresses, hence the tensile stresses appear and gradually increase at the bottom left and top right corners of the hole, and at the bottom right and top left corners of the wall. These areas correspond to the critical zones of the wall for crack openings. The wall response in terms of plastic bands localization reveals that an increasing number of bands are associated to the Gauss points of the wall from step A to C.

Parameters	$E\ [MPa]$	ν	$c_0\ [MPa]$	$\sigma_0\ [MPa]$	$h_p\ [MPa^-1]$	$\varphi\ [^o]$	$\delta\ [^o]$
Mortar	3900	0.20	0.18	0.13	4000	37	$1/2\ \varphi$
Blocks	16700	0.15	–	–	–	–	–

Table 5.1: Hollow masonry wall - numerical comparison: elastic and inelastic parameters adopted for the blocks and interfaces constitutive model.

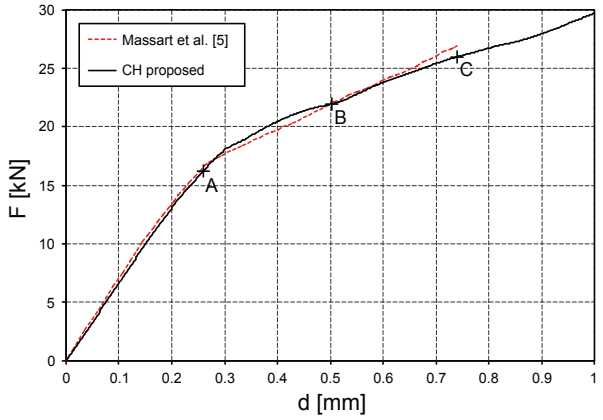

Figure 5.2: Hollow masonry wall - numerical comparison: shear load F as a function of the horizontal displacement d.

Their location is coherent with respect to the resulting stresses. Numbers indicate the progressive order of the initiation of the plastic bands in the panel. On the basis of the direction of the strain jumps, bands are also distinguished between splitting tensile mode (mode I) and mixed mode. It is also noted that at the step B a second failure mechanism initiates with the development of horizontal cracks at the two vertical sides of the wall. Overall, all the embedded bands evolve in a mixed mode due to the simultaneous effect of vertical and shear stresses, with the exception of the aforementioned bands which propagate in mode I. The bottom array of Fig. 5.3 describes the evolution of plasticity in the UC for the Gauss points named 3 and 16. A color map is associated to the value of χ_p in the range 0 to 1 and is displayed in correspondence with the mortar joints, as the brick behaves elastically. Red and blue colors indicate a stronger and a weaker decohesion, respectively. As expected, a typical zig-zag evolution of plasticity characterizes point 3, while typical bed joint cracking for tensile stress is clearly showed at point 16.
The obtained response and failure mechanisms reflect the initiation and propagation of wall cracks observed during experimental tests on similar kind of wall specimens [74].

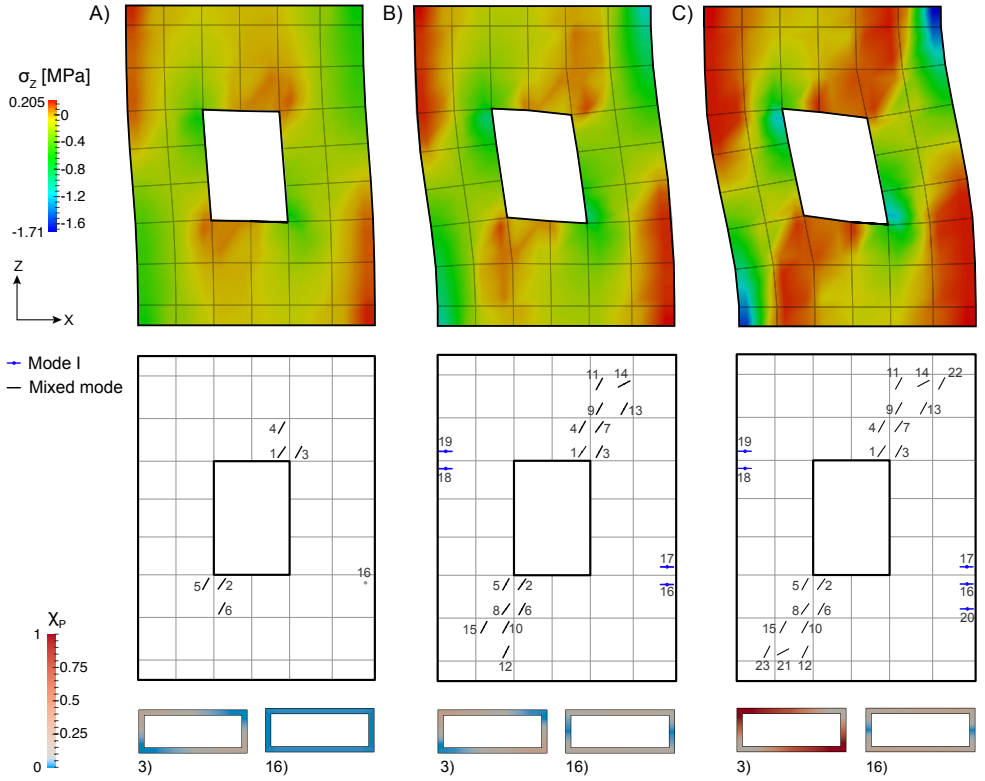

Figure 5.3: Hollow masonry wall - numerical comparison: vertical stress maps on deformed shape, macroscopic localizations relative to the steps A, B, C, mesoscopic localizations relative to the GPs named 3 and 16.

5.4 Solid masonry wall

The masonry wall shown in Fig. 5.4 was analyzed. Experimental results for this example were provided by the work of Raijmakers and Vermeltfoort [74]. The dimensions of the wall are: width 990 mm, height 1080 mm, thickness T = 100 mm. It is build up with 18 courses of clay bricks (dimensions 204 × 50 × 98 mm), whose the first and last were clamped in steel beams, assembled with 10 mm thick mortar joints. The geometry of the model and the boundary condition adopted are shown in Fig. 5.4. The wall was experimentally subjected initially to a vertical compressive load uniformly applied at the top side q, subsequently, the vertical translation and the rotation of the top side was restrained and a horizontal leftward displacement d monotonically increasing until the value of 4 mm was applied. The values of elastic and inelastic properties of the block and of the joints are reported in Table 5.2. It should be noted that the adopted values are coincident with those assumed in other numerical examples [29, 53].

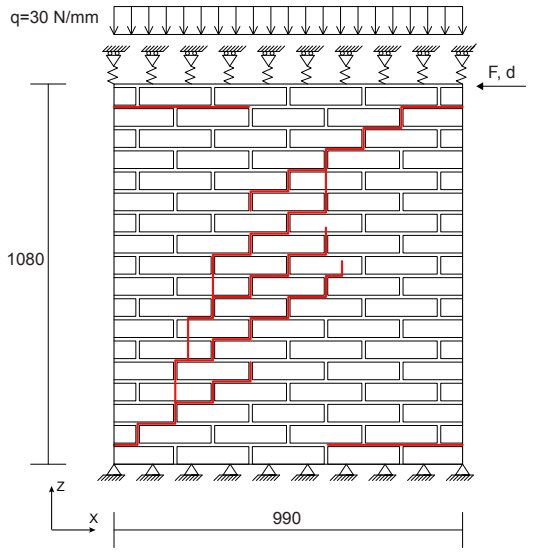

Figure 5.4: Solid masonry wall - experimental validation: geometry, boundary conditions and damage pattern of the masonry specimen considered by Raijmakers and Vermeltfoort [74]. Geometrical dimensions are expressed in millimeters.

Parameters	$E\ [MPa]$	ν	$c_0\ [MPa]$	$\sigma_0\ [MPa]$	$h_p\ [MPa^-1]$	$\varphi\ [^o]$	$\delta\ [^o]$
Mortar	820	0.14	0.35	0.25	500	37	$1/2\ \varphi$
Blocks	16700	0.15	–	–	–	–	–

Table 5.2: Solid masonry wall - experimental validation: elastic and inelastic parameters adopted for the blocks and interfaces constitutive model.

The comparison between the numerical and the experimental load-displacement curves is illustrated in Fig. 5.5. The simulation was performed by considering a UC with effective dimensions, i.e. width 204 mm, height 50 mm, and with the ones used in the previous Section by Massart et al. [58], i.e. i.e. width 90 mm, height 30 mm. The response shows in both cases an initial elastic branch which is followed by a non-linear behavior due to the formation of tensile cracks on the left-top side of the wall and on the bottom-right side of the wall. The two load-displacement curves show a UC dimension dependence, with the best numerical-experimental matching obtained applying the effective size of the UC. A slightly diverging of the numerical response is visible from 2.5 mm, however this was an expected result because of the missed compression failure of the interface model.
With respect to a classic finite element analysis, where a finer mesh guarantees better results, in the multi-scale analysis this cannot be guaranteed, since it may depend on UC dimensions. It seems that, even though the effective UC has questionable dimensions if one follows the principle of separation of scales, the experimental response is better estimated adopting the effective dimension of the UC. Effectively, although the principle of separation of scales is not strictly respected, the smeared band model seems to allow obtaining reasonable load-displacement response.
The macroscopic stress component is mapped in Fig. 5.6 for three different load steps named A, B, C in Fig. 5.5. At the same steps the localization bands are visible for the Gauss points where localization actives. At the stage A, before reaching the peak load, the tensile zones are evident at the two corners where the horizontal cracks appear. Figure 5.6 (b) shows how the tensile zones expand more in the vertical direction. In Fig. 5.6 (c) the two cracks at the corners and the diagonal crack are perfectly formed. Two zones in compression are distinguishable, they confine the diagonal cracked area and are responsible of the indefinite elastic response observed after the flat branch.
Although the localization map appears coarse in the sense that the fractures lines are not easily recognizable, it should be noted that not all the Gauss points

activate the localization bands at the same time, therefore the dissipated energy cannot be the same for the bands visible at the step A, B, C.

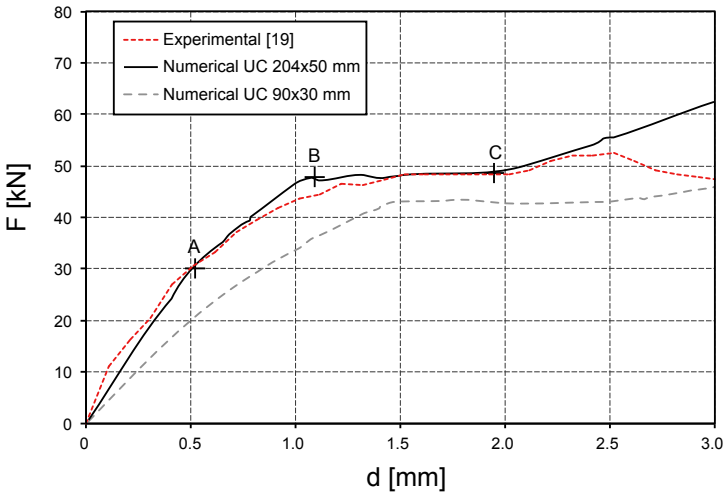

Figure 5.5: Solid masonry wall - experimental validation: shear load F as a function of the horizontal displacement d.

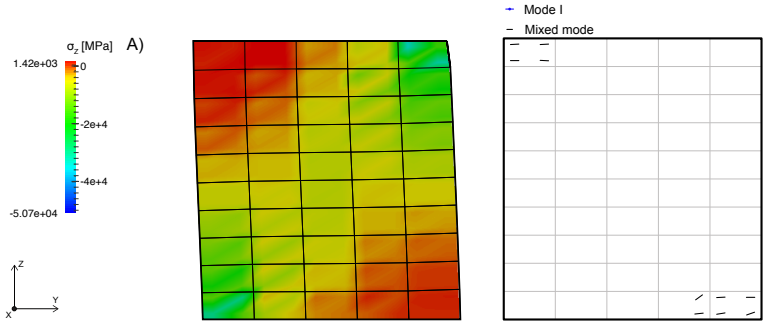

(a)

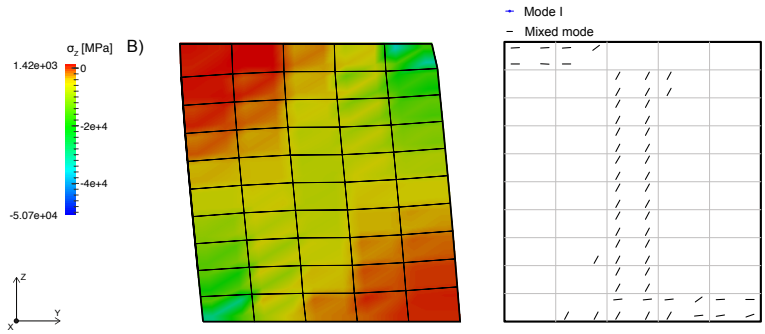

(b)

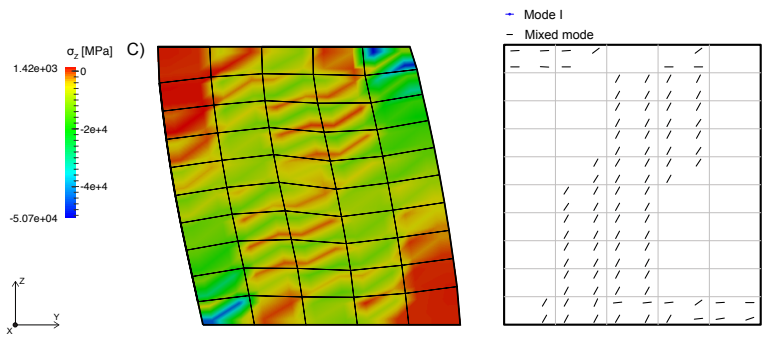

(c)

Figure 5.6: Solid masonry wall - experimental validation: vertical stress maps on deformed shape and macroscopic localization results relative to the steps (a) A, (b) B, (c) C.

5.5 Hollow masonry wall - experimental validation

The specimen subjected to the experimental shear test performed by Raijmakers and Vermeltfoort [74] consists of a single wythe masonry wall 990 × 1100 mm built up with 18 courses (16 active courses and two courses clamped to steel beams) of solid clay bricks (dimensions 204 × 98 × 50 mm) and 10 mm thick mortar joints. The wall has an opening in the middle obtained by eliminating a portion equal to one brick per six consecutive courses. The top and bottom boundaries of the wall are clamped. The wall is subjected to a compressive uniformly distributed load q before a horizontal load F is monotonically increased under top displacement control d. Figure 5.7 illustrates the geometry of the specimen with the damage pattern observed after performing the experimental test.
The values of elastic and inelastic properties of the block and of the joints are reported in Table 5.2.

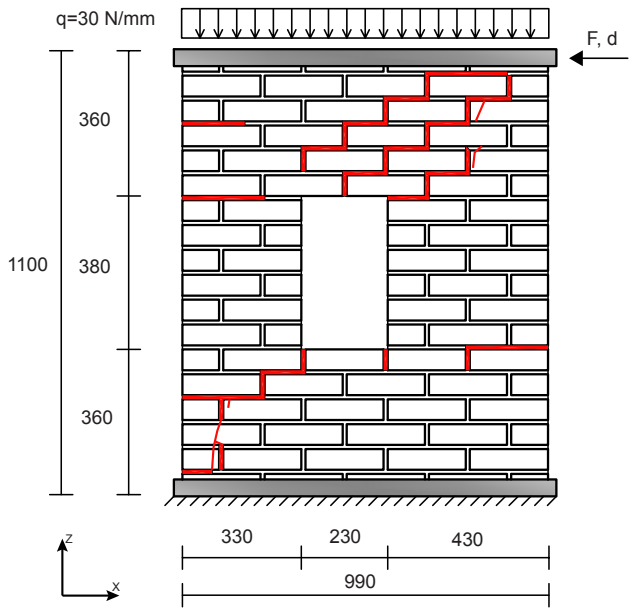

Figure 5.7: Hollow masonry wall - experimental validation: geometry, boundary conditions and damage pattern of the masonry specimen considered by Raijmakers and Vermeltfoort [74]. Geometrical dimensions are expressed in millimeters.

The characteristic dimensions of the masonry wall and of the bricks are of the same order. For instance the ratio between the width of the brick and the width of the panel is 0.2 and this ratio increases to 1 if the window width is considered as a characteristic structure dimension. This geometrical fact indicates that the correct approach for the structural study is the mesoscopic one [53]. The multi-scale approach has been applied to this structure by reducing the dimensions of the UC in order to satisfy the principle of scale separation. Therefore, the actual brick-joints dimensions in the numerical simulation have been downscaled by a factor of 2.5, which results in the brick 80 mm wide, 20 mm tall, 20 mm thick and in the joint 4 mm thick. It is observed that the downscaling operation maintains constant the volume ratio of the two constituents. Nonetheless, the effective UC dimensions were also considered.
The macroscopic model was discretized by means of 150 two dimensional four-noded elements with four Gauss integration points. As in the previous example, the UC is mesh-free with 17 nodes.

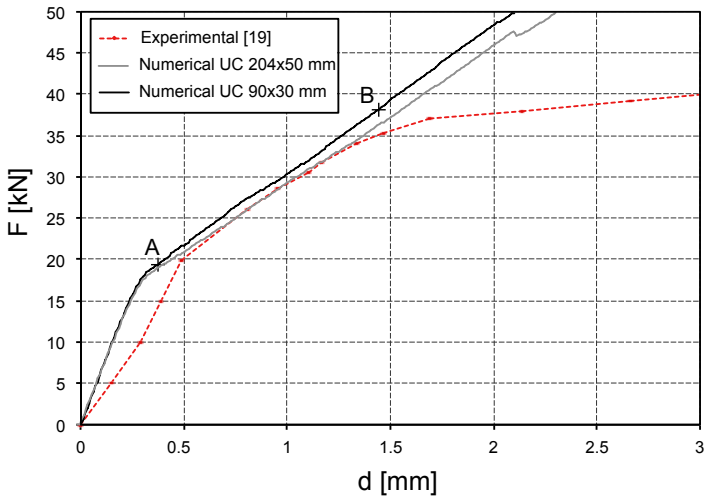

Figure 5.8: Hollow masonry wall - experimental validation: shear load F as a function of the horizontal displacement d.

The numerical results are reported in Figs. 5.8 and 5.9. The shear load F vs. the horizontal displacement d diagram (Fig. 5.8) shows that for both UCs

the masonry panel behaves elastically up to the force value of 18 kN where a prompt variation of the diagram slope indicates the onset of inelastic phenomena. The comparison between the numerical and the experimental results shows a good agreement both in the elastic and in the post-elastic stage. As observed in the previous example, the numerical response after point B maintains the same slope, diverging from the experimental trend, since masonry compression failure is inhibited due to the indefinitely elastic compressive behavior of bricks and mortar. Moreover, also in this case, the experimental response seems better estimated adopting the effective dimension of the UC.

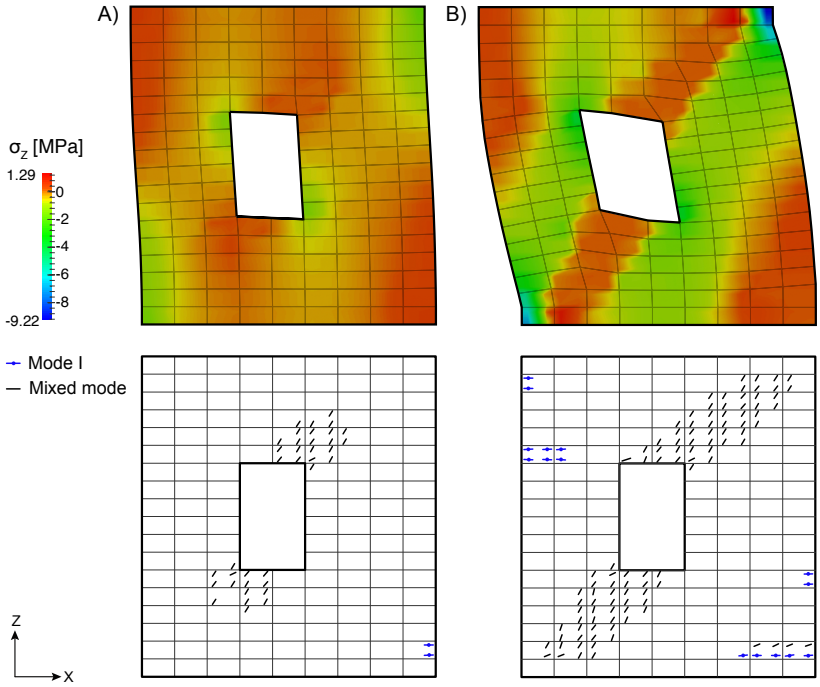

Figure 5.9: Hollow masonry wall - experimental validation: vertical stress maps on deformed shape and macroscopic localization results relative to the steps A and B.

The vertical normal stress and the directions and modes of the plastic bands at the Gauss points are represented both for point A and B of the load-displacement curve (Fig. 5.9). Overall, the CH analysis well captures the experimental fracture pattern (Fig. 5.9), as it is possible to observe from the

stress maps. At point A, two diagonal strain localizations arise from the corners of the opening. These zones propagate towards the corners of the masonry specimen (Point B). In addition, horizontal localization bands, corresponding to opening mode fractures caused by bending, appear and propagate between point A and B in correspondence of top left and bottom right corners. Similar localization bands appear at the two vertical boundaries at the level of the top and bottom sides of the window.
The quantitative and qualitative match of the real masonry specimens and the one simulated with a smaller UC can be commented as follows. On the one hand, since the volume ratios of the two phases, brick and mortar, are the same, the elastic properties of the two masonry texture are the same. On the other hand, the masonry texture difference does not strongly influence the fracture patterns, hence the damaged/sound material ratio, as deduced from the quite well overlapping of the numerical branch A-B with the experimental data.

5.6 Baglio Granatelli wall

This example is relative to a masonry wall part of a historical courtyard house located in Mazara Del Vallo (TP). The traditional Sicilian courtyard house is usually referred to as *Baglio*. This building dates back to the first years of the eighteenth century and was property of Granatelli Prince. The whole structure is made-up by block of yellow calcarenite, one of the most famous historic Mediterranean stones, assembled by means of mortar joints. In order to apply the CH procedure developed, a wall belonging to the south-east façade was chosen, see Fig. 5.10.

Figure 5.10: Baglio Granatelli wall: south-east façade.

Figure 5.11: Baglio Granatelli wall: south-east façade survey.

This wall was characterized by an arch-shaped failure that suggests a masonry collapse caused by a foundation settlement. Figure 5.11 shows the façade geometrical survey with a red line underlying the blocks originally at the interface with the collapsed ones. The material properties, deduced from experimental data on similar traditional materials, are reported in Table 5.3. The UC dimensions were deduced by averaging the two main dimensions (the width and the height) of all the blocks in the façade. The results of these averages led to a UC 388 mm wide and 236 mm tall, surrounded by 10 mm of mortar joint. The macroscopic model was constituted by 303 four-noded elements and 344 nodes. The analysis was conducted with a maximum vertical displacement imposed per step equal to 0.05 mm.
The results in terms of the evolution of the vertical stress and localization bands are reported in Figs. 5.12 and 5.13. Four steps were considered, each step was associated to a maximum value of stress and vertical displacement. The step 500 was chosen as the one were the bands of the Gauss points re-create the arch-shaped failure, therefore the maximum displacement equal to 25 mm was considered as a reasonable value of the foundation settlement.

Parameters	$E\ [MPa]$	ν	$c_0\ [MPa]$	$\sigma_0\ [MPa]$	$h_p\ [MPa^-1]$	$\varphi\ [^o]$	$\delta\ [^o]$
Mortar	208	0.15	0.028	0.007	1000	37	$1/2\ \varphi$
Blocks	1364	0.2	–	–	–	–	–

Table 5.3: Baglio Granatelli wall: elastic and inelastic parameters adopted for the blocks and interfaces constitutive model.

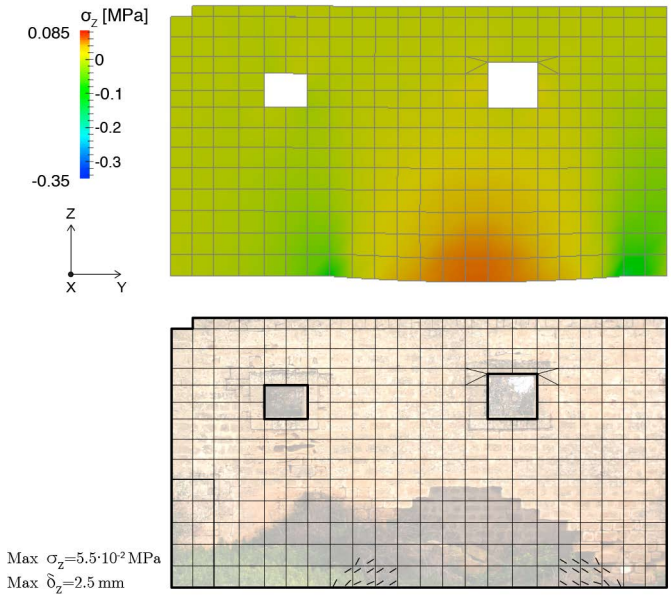

(a) Step 50

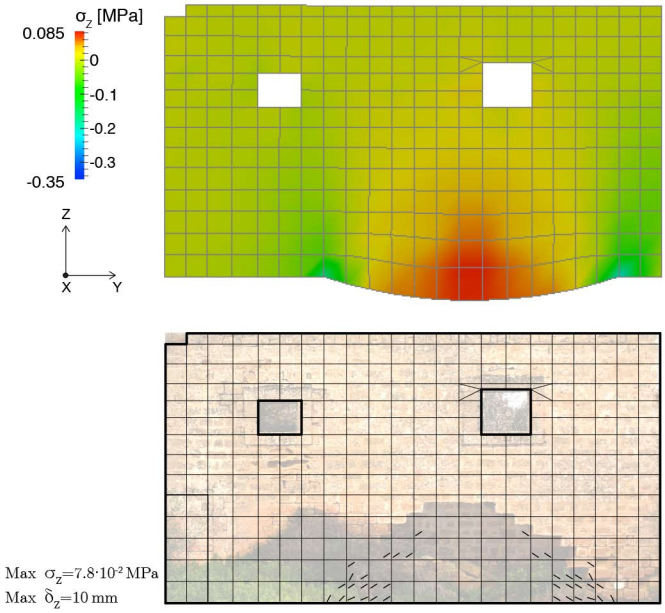

(b) Step 200

Figure 5.12: Baglio Granatelli masonry wall: vertical stress maps on deformed shape and macroscopic localization results.

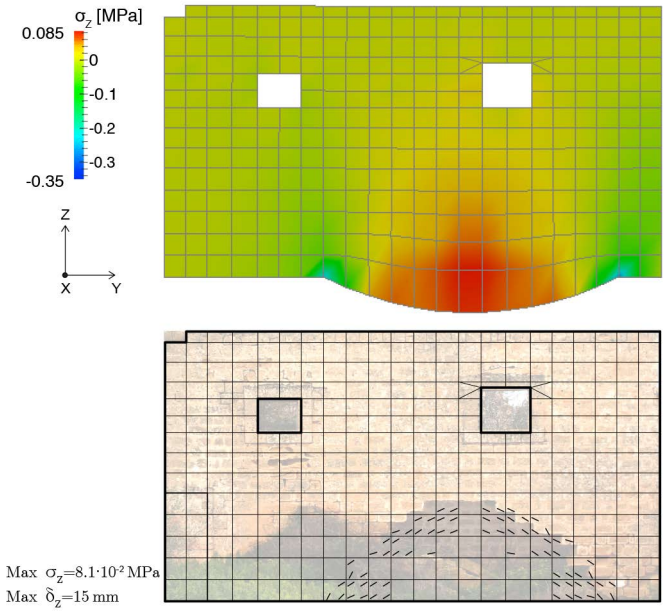

(a) Step 300

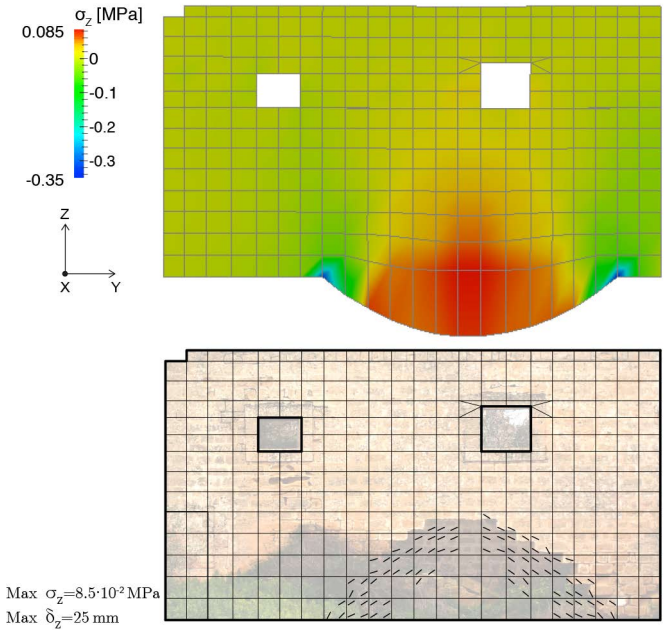

(b) Step 500

Figure 5.13: Baglio Granatelli masonry wall: vertical stress maps on deformed shape and macroscopic localization results.

Chapter 6

Conclusions and remarks

In the last few decades, the development of multi-scale CH techniques to evaluate the response of structures made-up by heterogeneous materials, regarded as an assembly of units or aggregates interacting by adhesive/cohesive joints, as masonry material, has been increasing. The reason lies in the compromise that this technique represents with respect to the macroscopic and mesoscopic approaches. Actually, the macroscopic behavior is strongly influenced by the kinematical and static phenomena occurring at the mesoscopic level. In particular, anisotropy, stiffness degradation and irreversible displacement observed at the macro-scale are the results of the opening-closing, sliding and dilatancy occurring in the joints. The multi-scale CH allows to overcome the formulation of closed-form constitutive laws that should be identified on the basis of costly and difficult macroscopic experimental procedure that should be reproduced for every new microstructure. According to this technique, the macroscopic material response is obtained from the solution of a mesoscopic BVP formulated for a representative volume element or unit cell. Suitable transition-scales laws have to be used.
The goal of the research reported in this dissertation is to add some new input elements for those who apply the first-order homogenization technique to masonry structures, with the perspective to expand and support this computational tool. As a matter of fact, it does not still exist a univocal line tested as the most efficient one for the formulation of the multi-scale CH procedure for masonry material.
It is well-known that the solution of the mesoscopic BVP is the key-point of the multi-scale procedure and its computational cost strongly influences the overall cost for a given structural problem [59]. Therefore, the UC is chosen as

the minimum portion of the structure that contains the constituents and whose repetition along specific periodic directions builds the entire masonry assembly. Specifically, it is constituted by a block surrounded by half-thickness mortar joints. To improve the overall efficiency two aspects are focused, as presented in Chapter 3.

Firstly the numerical solution, in fact the UC BVP is solved making use of a meshless computation procedure. Analyzing the UC response in pure modes and comparing it with a standard FE response, it has been proved that (i) reliability of the macroscopic UC behavior is obtained, (ii) meshless discretization may offer a computational gain in terms of degrees of freedom by optimizing the number of nodes together with the number of GPs. Since the equilibrium problem of the global structure is solved by means of a classical FE discretization, the presented approach can be classified as a *FE·Meshless* CH approach. In addition, an elasto-plastic zero-thickness interface model is applied to model the mortar joints mechanical behavior while the block behaves elastically. Since, at the UC level, the displacement field is discontinuous along the decohesion process, while at the macro-scale it remains continuous, the approach may be classified as a *discontinuous-continuous* CH approach.

Chapter 3 shows also the response of the UC under periodic and linear boundary conditions. In spite of the fact that periodic boundary conditions are the most commonly used conditions, suggested by the initial periodicity of the material and realistic, if smoothly varying macroscopic fields are considered, they may be questioned when strain localization occurs. On the other hand, linear boundary conditions seems to overestimate the global response. The observations emphasize the importance of making a suitable choice for the macro-to-meso transition law. It was also observed that, under periodic BCs, the natural traction BCs may be obtained by decoupling the degrees of freedom of points common to adjacent boundaries, avoiding the spurious oscillations recorded in the same points using FEM.

Chapter 4 illustrates that the decohesion phenomena, the crack formation and propagation, simulated at the mesoscopic level, are taken into account at the macro level in a smeared mode, introducing a strain localization band as a weak discontinuity. The smearing of the macroscopic strain over the Gauss point volume represents a sort of regularization that is expected to make the solution mesh-independent. The smeared band model is proved in 1D with respect to the closed-form 1D solution obtained with the standard localization hypotheses. The equivalence between the macroscopic strain localization band and the mesoscopic decohesion and fracture zones is established on the basis of

a spectral analysis of the acoustic tensor, built with the tangent stiffness matrix resulting from the UC BVP.
The FE·Meshless strategy has been validated through numerical examples, presented in Chapter 5. It is proved the capability of the model to achieve the same results of the enhanced multi-scale model of Massart et al. [58], based on a FE^2 numerical strategy. It is confirmed also the capability of the model to reproduce experimental findings [74]. Overall, the results demonstrated that a good prediction of a structure stiffness and cracking patterns may be obtained. Lastly, the model is resulted able to predict the foundation settlement that caused a masonry wall collapse in a historical building. Analysis like the last one represents the goal of this dissertation, to have an efficient computational tool for masonry structures.
From the perspective of future developments, this strategy may introduce some additional refinements at both mesoscopic and macroscopic scales. A nonlinear behavior for the units and failure in compression for the joints may be considered. Besides, the problem of crack formation and propagation inside the block can be easily treated since the solution refinement requires only the increment of the nodes number. Also, more efficient and sophisticated regularization strategies can be adopted for strain localization at the macro-scale. Many authors have observed the strong mesh dependency of the macroscopic response exhibited by the first-order technique. In addition, many authors have been stating that the technique cannot be applied if the principle of separation of scale is violated. These aspects should not be neglected and deeply investigated when dealing with bock failure. Extension of the CH to include a higher-order continuum at the mesoscopic level is also possible.
The extension of the presented technique towards the computation of different heterogeneous material represents a prompt step, both for 2D and 3D analyses. The perspective is collecting several implementations of UCs, associated to as many material laws, to build a series of new meso-structures suitable for global structures. In this respect, Fig. 6.1 represents a first attempt with the elastic response of a possible simplified statistical representative UC for concrete. It is constituted by a 2D circular aggregate inside the solid of matrix. The map of the elastic energy for a shear test points out that the aggregate-matrix interface may play a major role in the fracture mechanism. A meshless discretization was used (Fig.6.1 (b)) and validated with the FE one (Fig. 6.2).
Overall, the findings of this dissertation these may represent a complement to other CH models for structural masonry computations.

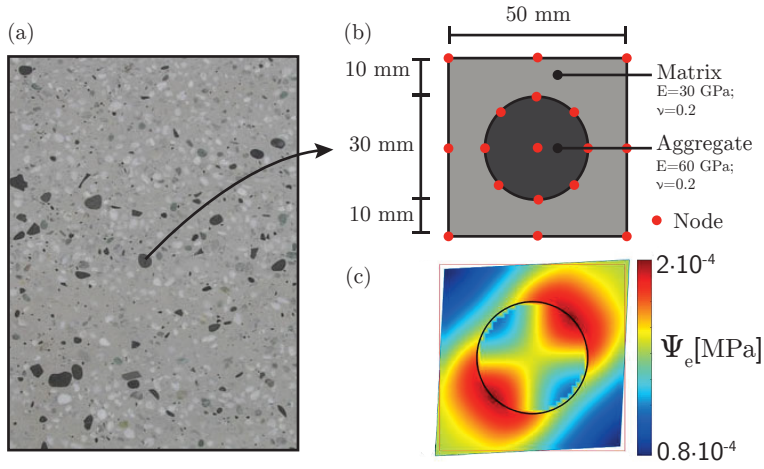

Figure 6.1: Multi-scale CH for concrete: (a) macroscopic level, (b) mesoscopic level with a possible statistical representative UC, (c) elastic energy density associated to the UC.

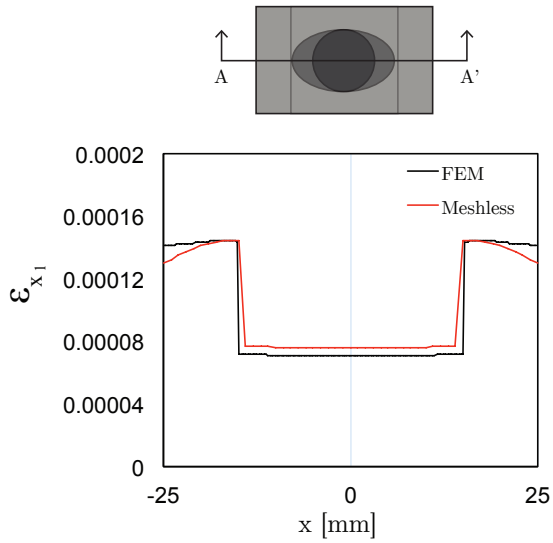

Figure 6.2: Stretching test along x_1: elastic response in terms of deformation along section AA'.

Bibliography

[1] N. Abolfathi, A. Naik, G. Karami, and C. Ulven. A micromechanical characterization of angular bidirectional fibrous composites. *Computational Materials Science*, 43(4):1193–1206, 2008.

[2] D. Addessi and E. Sacco. A multi-scale enriched model for the analysis of masonry panels. *International Journal of Solids and Structures*, 49(6):865–880, 2012.

[3] D. Addessi, E. Sacco, and A. Paolone. Cosserat model for periodic masonry deduced by nonlinear homogenization. *European Journal of Mechanics-A/Solids*, 29(4):724–737, 2010.

[4] G. Alfano and M. Crisfield. Finite element interface models for the delamination analysis of laminated composites: mechanical and computational issues. *International journal for numerical methods in engineering*, 50(7):1701–1736, 2001.

[5] A. Anthoine. Derivation of the in-plane elastic characteristics of masonry through homogenization theory. *International Journal of Solids and Structures*, 32(2):137–163, 1995.

[6] A. Bacigalupo and L. Gambarotta. Computational two-scale homogenization of periodic masonry: characteristic lengths and dispersive waves. *Computer Methods in Applied Mechanics and Engineering*, 213:16–28, 2012.

[7] Z. P. Bažant and B. H. Oh. Crack band theory for fracture of concrete. *Matériaux et construction*, 16(3):155–177, 1983.

[8] Z. P. Bazant and G. Pijaudier-Cabot. Measurement of characteristic length of nonlocal continuum. *Journal of Engineering Mechanics*, 115(4):755–767, 1989.

[9] Z. P. Bazant and J. Planas. *Fracture and size effect in concrete and other quasibrittle materials*, volume 16. CRC press, 1997.

[10] T. Belytschko and T. Black. Elastic crack growth in finite elements with minimal remeshing. *International journal for numerical methods in engineering*, 45(5):601–620, 1999.

[11] T. Belytschko, J. Fish, and B. E. Engelmann. A finite element with embedded localization zones. *Computer methods in applied mechanics and engineering*, 70(1):59–89, 1988.

[12] D. Bigoni. *Nonlinear solid mechanics: bifurcation theory and material instability*. Cambridge University Press, 2012.

[13] G. Borré and G. Maier. On linear versus nonlinear flow rules in strain localization analysis. *Meccanica*, 24(1):36–41, 1989.

[14] E. Bosco, V. Kouznetsova, and M. Geers. Multi-scale computational homogenization–localization for propagating discontinuities using x-fem. *International Journal for Numerical Methods in Engineering*, 102(3-4):496–527, 2015.

[15] Y. Chen, J. Lee, and A. Eskandarian. *Meshless methods in solid mechanics*. Springer Science & Business Media, 2006.

[16] T. Christman, A. Needleman, and S. Suresh. An experimental and numerical study of deformation in metal-ceramic composites. *Acta Metallurgica*, 37(11):3029–3050, 1989.

[17] E. Coenen, V. Kouznetsova, E. Bosco, and M. Geers. A multi-scale approach to bridge microscale damage and macroscale failure: a nested computational homogenization-localization framework. *International journal of fracture*, 178(1-2):157–178, 2012.

[18] M. L. De Bellis and D. Addessi. A cosserat based multi-scale model for masonry structures. *International Journal for Multiscale Computational Engineering*, 9(5):543, 2011.

[19] M. Dhanasekar, A. Page, and P. Kleeman. The failure of brick masonry under biaxial stresses. *Proceedings of the Institution of Civil Engineers*, 79(2):295–313, 1985.

[20] J. Dolbow and T. Belytschko. A finite element method for crack growth without remeshing. *International journal for numerical methods in engineering*, 46(1):131–150, 1999.

[21] W. Drugan and J. Willis. A micromechanics-based nonlocal constitutive equation and estimates of representative volume element size for elastic composites. *Journal of the Mechanics and Physics of Solids*, 44(4):497–524, 1996.

[22] E. N. Dvorkin, A. M. Cuitiño, and G. Gioia. Finite elements with displacement interpolated embedded localization lines insensitive to mesh size and distortions. *International journal for numerical methods in engineering*, 30(3):541–564, 1990.

[23] L. Evers, D. Parks, W. Brekelmans, and M. Geers. Crystal plasticity model with enhanced hardening by geometrically necessary dislocation accumulation. *Journal of the Mechanics and Physics of Solids*, 50(11):2403–2424, 2002.

[24] F. Feyel and J.-L. Chaboche. Fe 2 multiscale approach for modelling the elastoviscoplastic behaviour of long fibre sic/ti composite materials. *Computer methods in applied mechanics and engineering*, 183(3):309–330, 2000.

[25] R. Finno, W. Harris, M. A. Mooney, and G. Viggiani. Shear bands in plane strain compression of loose sand. *Geotechnique*, 47(1):149–165, 1997.

[26] P. Fuschi, G. Giambanco, and S. Rizzo. Nonlinear finite element analysis of no-tension masonry structures. *Meccanica*, 30(3):233–249, 1995.

[27] M. G. Geers, V. G. Kouznetsova, and W. Brekelmans. Multi-scale computational homogenization: Trends and challenges. *Journal of computational and applied mathematics*, 234(7):2175–2182, 2010.

[28] G. Giambanco, E. La Malfa Ribolla, and A. Spada. Ch of masonry materials via meshless meso-modeling. *Frattura ed Integrita Strutturale*, (29):150, 2014.

[29] G. Giambanco, S. Rizzo, and R. Spallino. Numerical analysis of masonry structures via interface models. *Computer methods in applied mechanics and engineering*, 190(49):6493–6511, 2001.

[30] G. Giambanco, G. F. Scimemi, and A. Spada. The interphase finite element. *Computational Mechanics*, 50(3):353–366, 2012.

[31] R. E. Goodman, R. L. Taylor, and T. L. Brekke. A model for the mechanics of jointed rocks. *Journal of Soil Mechanics & Foundations Div*, 1968.

[32] D. Griffiths. Numerical modeling of interfaces using conventional finite elements. In *Fifth international conference on numerical methods in geomechanics, Nagoya*, pages 837–844, 1985.

[33] V. Gulizzi, A. Milazzo, and I. Benedetti. An enhanced grain-boundary framework for computational homogenization and micro-cracking simulations of polycrystalline materials. *Computational Mechanics*, 56(4):631–651, 2015.

[34] L. R. Herrmann. Finite element analysis of contact problems. *Journal of the Engineering Mechanics Division*, 104(5):1043–1057, 1978.

[35] R. Hill. Elastic properties of reinforced solids: some theoretical principles. *Journal of the Mechanics and Physics of Solids*, 11(5):357–372, 1963.

[36] R. Hill. A self-consistent mechanics of composite materials. *Journal of the Mechanics and Physics of Solids*, 13(4):213–222, 1965.

[37] J. R. Jain and S. Ghosh. Damage evolution in composites with a homogenization-based continuum damage mechanics model. *International Journal of Damage Mechanics*, 18(6):533–568, 2008.

[38] M. Jirásek. Modeling of localized damage and fracture in quasibrittle materials. In *Continuous and Discontinuous Modelling of Cohesive-Frictional Materials*, pages 17–29. Springer, 2001.

[39] M. Jirásek. Objective modeling of strain localization. *Revue française de génie civil*, 6(6):1119–1132, 2002.

[40] M. Jirásek and M. Bauer. Numerical aspects of the crack band approach. *Computers & Structures*, 110:60–78, 2012.

[41] M. Jirásek and J. Zeman. Localization study of a regularized variational damage model. *International Journal of Solids and Structures*, 69:131–151, 2015.

[42] Ł. Kaczmarczyk, C. J. Pearce, N. Bićanić, and E. de Souza Neto. Numerical multiscale solution strategy for fracturing heterogeneous materials. *Computer Methods in Applied Mechanics and Engineering*, 199(17):1100–1113, 2010.

[43] T. Kanit, S. Forest, I. Galliet, V. Mounoury, and D. Jeulin. Determination of the size of the representative volume element for random composites: statistical and numerical approach. *International Journal of solids and structures*, 40(13):3647–3679, 2003.

[44] M. Klisinski, K. Runesson, and S. Sture. Finite element with inner softening band. *Journal of Engineering Mechanics*, 117(3):575–587, 1991.

[45] W. T. Koiter. Stress-strain relations, uniqueness and variational theorems for elastic-plastic materials with a singular yield surface. *Quarterly of applied mathematics*, 11(3):350–354, 1953.

[46] V. Kouznetsova, M. G. Geers, and W. M. Brekelmans. Multi-scale constitutive modelling of heterogeneous materials with a gradient-enhanced computational homogenization scheme. *International Journal for Numerical Methods in Engineering*, 54(8):1235–1260, 2002.

[47] J. Lemaitre and J.-L. Chaboche. *Mechanics of solid materials*. Cambridge university press, 1994.

[48] S. Li. On the unit cell for micromechanical analysis of fibre-reinforced composites. In *Proceedings of the Royal Society of London A: Mathematical, Physical and Engineering Sciences*, volume 455, pages 815–838. The Royal Society, 1999.

[49] S. Li. General unit cells for micromechanical analyses of unidirectional composites. *Composites Part A: applied science and manufacturing*, 32(6):815–826, 2001.

[50] S. Li. Boundary conditions for unit cells from periodic microstructures and their implications. *Composites Science and Technology*, 68(9):1962–1974, 2008.

[51] S. Li. On the nature of periodic traction boundary conditions in micromechanical fe analyses of unit cells. *IMA Journal of Applied Mathematics*, 77(4):441–450, 2011.

[52] P. B. Lourenço. Sensitivity analysis of masonry structures. In *Proc. 8th Canadian Masonry Symp*, pages 563–574, 1998.

[53] P. B. Lourenço and J. G. Rots. Multisurface interface model for analysis of masonry structures. *Journal of engineering mechanics*, 123(7):660–668, 1997.

[54] R. Luciano and E. Sacco. Variational methods for the homogenization of periodic heterogeneous media. *European Journal of Mechanics-A/Solids*, 17(4):599–617, 1998.

[55] G. Maier and A. Nappi. A theory of no-tension discretized structural systems. *Engineering structures*, 12(4):227–234, 1990.

[56] J. Mandel. *Plasticité Classique et Viscoplasticité*, volume CISM Courses and Lectures No 97. Springer-Verlag, Berlin, 1972.

[57] T. Massart, R. Peerlings, and M. Geers. Mesoscopic modeling of failure and damage-induced anisotropy in brick masonry. *European Journal of Mechanics-A/Solids*, 23(5):719–735, 2004.

[58] T. Massart, R. Peerlings, and M. Geers. An enhanced multi-scale approach for masonry wall computations with localization of damage. *International journal for numerical methods in engineering*, 69(5):1022–1059, 2007.

[59] T. J. Massart. *Multi-scale modeling of damage in masonry structures*. PhD thesis, Université libre de Bruxelles, 2003.

[60] B. Mercatoris, P. Bouillard, and T. Massart. Multi-scale detection of failure in planar masonry thin shells using computational homogenisation. *Engineering fracture mechanics*, 76(4):479–499, 2009.

[61] C. Miehe and A. Koch. Computational micro-to-macro transitions of discretized microstructures undergoing small strains. *Archive of Applied Mechanics*, 72(4-5):300–317, 2002.

[62] S. Nemat-Nasser and M. Hori. Universal bounds for overall properties of linear and nonlinear heterogeneous solids. *Journal of engineering materials and technology*, 117(4):412–432, 1995.

[63] S. Nemat-Nasser and M. Hori. Micromechanics: overall properties of heterogeneous solids. *Elsevier, Amsterdam*, 1999.

[64] G. D. Nguyen, C. T. Nguyen, V. P. Nguyen, H. H. Bui, and L. Shen. A size-dependent constitutive modelling framework for localised failure analysis. *Computational Mechanics*, 58(2):257–280, 2016.

[65] V. P. Nguyen, O. Lloberas-Valls, M. Stroeven, and L. J. Sluys. On the existence of representative volumes for softening quasi-brittle materials–a failure zone averaging scheme. *Computer Methods in Applied Mechanics and Engineering*, 199(45):3028–3038, 2010.

[66] V. P. Nguyen, T. Rabczuk, S. Bordas, and M. Duflot. Meshless methods: a review and computer implementation aspects. *Mathematics and computers in simulation*, 79(3):763–813, 2008.

[67] V. P. Nguyen, M. Stroeven, and L. J. Sluys. Multiscale continuous and discontinuous modeling of heterogeneous materials: a review on recent developments. *Journal of Multiscale Modelling*, 3(04):229–270, 2011.

[68] J. Oliver. A consistent characteristic length for smeared cracking models. *International Journal for Numerical Methods in Engineering*, 28(2):461–474, 1989.

[69] N. S. Ottosen and K. Runesson. Properties of discontinuous bifurcation solutions in elasto-plasticity. *International Journal of Solids and Structures*, 27(4):401–421, 1991.

[70] B. Patzák and M. Jirásek. Process zone resolution by extended finite elements. *Engineering Fracture Mechanics*, 70(7):957–977, 2003.

[71] D. Perić, E. de Souza Neto, R. Feijóo, M. Partovi, and A. Molina. On micro-to-macro transitions for multi-scale analysis of non-linear heterogeneous materials: unified variational basis and finite element implementation. *International Journal for Numerical Methods in Engineering*, 87(1-5):149–170, 2011.

[72] S. Pietruszczak and Z. Mroz. Finite element analysis of deformation of strain-softening materials. *International Journal for Numerical Methods in Engineering*, 17(3):327–334, 1981.

[73] S. Pietruszczak and X. Niu. A mathematical description of macroscopic behaviour of brick masonry. *International journal of solids and structures*, 29(5):531–546, 1992.

[74] T. Raijmakers and A. Vermeltfoort. *Deformation controlled tests in masonry shear walls: report B-92-1156*. TNO-Bouw, Delft, The Netherlands, 1992.

[75] P. Roca, J. González, E. Oñate, and P. Lourenço. Experimental and numerical issues in the modelling of the mechanical behaviour of masonry. *Structural Analysis of Historical Constructions II. CIMNE, Barcelona*, 1998.

[76] J. G. Rots. *Structural masonry: an experimental/numerical basis for practical design rules*. AA Balkema, 1997.

[77] E. Sacco. A nonlinear homogenization procedure for periodic masonry. *European Journal of Mechanics-A/Solids*, 28(2):209–222, 2009.

[78] S. Saeb, P. Steinmann, and A. Javili. Aspects of computational homogenization at finite deformations: A unifying review from reuss' to voigt's bound. *Applied Mechanics Reviews*, 68(5):050801, 2016.

[79] G. Sfantos and M. Aliabadi. Multi-scale boundary element modelling of material degradation and fracture. *Computer Methods in Applied Mechanics and Engineering*, 196(7):1310–1329, 2007.

[80] H. Shen and L. C. Brinson. A numerical investigation of the effect of boundary conditions and representative volume element size for porous titanium. *Journal of Mechanics of Materials and Structures*, 1(7):1179–1204, 2006.

[81] J. Simo and J. Oliver. A new approach to the analysis and simulation of strain softening in solids. *Fracture and damage in quasibrittle structures*, pages 25–39, 1994.

[82] L. Sluys. Discontinuous modeling of shear banding. *Computational plasticity: Fundamentals and applications*, pages 735–744, 1997.

[83] R. Smit, W. Brekelmans, and H. Meijer. Prediction of the mechanical behavior of nonlinear heterogeneous systems by multi-level finite element modeling. *Computer Methods in Applied Mechanics and Engineering*, 155(1):181–192, 1998.

[84] A. Spada, G. Giambanco, and E. La Malfa Ribolla. A fe-meshless multiscale approach for masonry materials. *Procedia Engineering*, 109:364–371, 2015.

[85] A. Spada, G. Giambanco, and P. Rizzo. Damage and plasticity at the interfaces in composite materials and structures. *Computer Methods in Applied Mechanics and Engineering*, 198(49):3884–3901, 2009.

[86] N. Sukumar, N. Moës, B. Moran, and T. Belytschko. Extended finite element method for three-dimensional crack modelling. *International Journal for Numerical Methods in Engineering*, 48(11):1549–1570, 2000.

[87] P. Suquet. Elements of homogenization for inelastic solid mechanics. *Homogenization techniques for composite media*, 272:193–278, 1987.

[88] K. Terada, M. Hori, T. Kyoya, and N. Kikuchi. Simulation of the multi-scale convergence in computational homogenization approaches. *International Journal of Solids and Structures*, 37(16):2285–2311, 2000.

[89] O. Van der Sluis, P. Schreurs, W. Brekelmans, and H. Meijer. Overall behaviour of heterogeneous elastoviscoplastic materials: effect of microstructural modelling. *Mechanics of Materials*, 32(8):449–462, 2000.

[90] G. Vasconcelos and P. B. Lourenço. In-plane experimental behavior of stone masonry walls under cyclic loading. *Journal of structural engineering*, 135(10):1269–1277, 2009.

[91] X. Wei and H. Hao. Numerical derivation of homogenized dynamic masonry material properties with strain rate effects. *International Journal of Impact Engineering*, 36(3):522–536, 2009.

[92] Z. Xia, C. Zhou, Q. Yong, and X. Wang. On selection of repeated unit cell model and application of unified periodic boundary conditions in micro-mechanical analysis of composites. *International Journal of Solids and Structures*, 43(2):266–278, 2006.

[93] X.-P. Xu and A. Needleman. Numerical simulations of fast crack growth in brittle solids. *Journal of the Mechanics and Physics of Solids*, 42(9):1397–1434, 1994.

[94] G. Zavarise, P. Wriggers, and B. Schrefler. A method for solving contact problems. *International Journal for Numerical Methods in Engineering*, 42(3):473–498, 1998.

[95] A. Zucchini and P. Lourenço. A micro-mechanical model for the homogenisation of masonry. *International Journal of Solids and Structures*, 39(12):3233–3255, 2002.

[96] A. Zucchini and P. B. Lourenço. A coupled homogenisation–damage model for masonry cracking. *Computers & structures*, 82(11):917–929, 2004.

[97] A. Zucchini and P. B. Lourenço. A micro-mechanical homogenisation model for masonry: Application to shear walls. *International Journal of Solids and Structures*, 46(3):871–886, 2009.

Appendix A

Essentials of thermodynamics

The first principle of thermodynamics accounts for the conservation of energy over a volume domain Ω. It can be mathematically expressed by

$$\frac{d}{dt}\left(I + K_{in}\right) = P + Q, \tag{A.1}$$

being I and K_{in}, the internal and kinematic energy in the volume Ω, respectively, P the work of external forces and Q the heat added to the system. under the assumption of small strains, the first principle of thermodynamics reads [47]:

$$\rho\,\dot{e} = \boldsymbol{\sigma} : \dot{\boldsymbol{\varepsilon}} + r - \operatorname{div}\mathbf{q} \tag{A.2}$$

with ρ the material density, e the specific internal energy, r the volumetric density of the internal heat production and $\vec{q}$ the heat flux vector through the boundary $\partial\Omega$.
It is also noted that the variation of temperature inside a volume Ω produces a variation of the total entropy S. According to the second principle of thermodynamics, the entropy rate is always higher or at least equal to the heat rate Q divided by the temperature T

$$\frac{dS}{dt} \geqslant \frac{Q}{T}. \tag{A.3}$$

Equation (A.3) can be rewritten as

$$\rho\frac{ds}{dt} + \operatorname{div}\frac{\mathbf{q}}{T} - \frac{r}{T} \geqslant 0, \tag{A.4}$$

where s is the specific entropy per unit mass.
Combining Eqs. (A.2) and (A.4) and after some mathematical manipulations, the following inequality is obtained

$$\boldsymbol{\sigma} : \dot{\boldsymbol{\varepsilon}} - \rho \left(\dot{\Psi} + s\dot{T} \right) - \mathbf{q} \cdot \frac{\nabla T}{T} \geqslant 0, \tag{A.5}$$

that is known as the fundamental *Clausius-Duhem inequality*. In Eq. (A.5), Ψ is named *Helmholtz free energy*, defined as

$$\Psi = e - T\, s. \tag{A.6}$$

This function has the characteristic to be scalar, concave with respect to the temperature T and convex with respect to the other variables. The Helmholtz free energy depends on a set of observable state variables and internal variables

$$\Psi = \Psi \left(\boldsymbol{\varepsilon}, T, \boldsymbol{\varepsilon}_p, \mathbf{V}_k \right), \tag{A.7}$$

where $\boldsymbol{\varepsilon}$ and T are the observable or directly measurable variables, while $\boldsymbol{\varepsilon}_p$ and $\mathbf{V}_k$ are the internal or not directly measurable variables used to describe irreversible mechanisms developing inside the volume Ω. Since the total deformation $\boldsymbol{\varepsilon}$ can be decomposed into the sum of elastic and plastic deformations, $\boldsymbol{\varepsilon}_e$ and $\boldsymbol{\varepsilon}_p$, the Helmholtz free energy can be derived and substituted into Eq. (A.5) to obtain

$$\left(\boldsymbol{\sigma} - \rho \frac{\partial \Psi}{\partial \boldsymbol{\varepsilon}_e} \right) : \dot{\boldsymbol{\varepsilon}}_e + \boldsymbol{\sigma} : \dot{\boldsymbol{\varepsilon}}_p - \rho \left(s + \frac{\partial \Psi}{\partial T} \right) \dot{T} - \rho \frac{\partial \Psi}{\partial \mathbf{V}_k} : \dot{\mathbf{V}}_k - \frac{\mathbf{q}}{T} \cdot \nabla T \geqslant 0. \tag{A.8}$$

The previous equation has to hold for any thermo-mechanical process. For instance, if the constitutive behavior is elastic ($\dot{\boldsymbol{\varepsilon}}_p = \mathbf{0}$), the temperature is constant and uniform ($\dot{T} = 0$, $\nabla T = \mathbf{0}$) and no irreversible mechanisms are involved ($\dot{\mathbf{V}}_k = \mathbf{0}$), Eq. (A.8), valid for any $\dot{\boldsymbol{\varepsilon}}_e$, leads to

$$\boldsymbol{\sigma} = \rho \frac{\partial \Psi}{\partial \boldsymbol{\varepsilon}_e}. \tag{A.9}$$

Conversely, in a thermal transformation with $\dot{\boldsymbol{\varepsilon}}_e = \dot{\boldsymbol{\varepsilon}}_p = \mathbf{0}$, $\dot{\mathbf{V}}_k = \mathbf{0}$, $\nabla T = \mathbf{0}$, being T arbitrary, it has to hold

$$s = -\frac{\partial \Psi}{\partial T}. \tag{A.10}$$

It is possible to define the thermodynamic forces associated with the internal variables by making the following position

$$\boldsymbol{\chi}_k = -\rho \frac{\partial \Psi}{\partial \mathbf{V}_k}. \tag{A.11}$$

Assuming always mechanisms associated to constant and uniform temperature ($\dot{T} = 0$, $\nabla T = \mathbf{0}$), an elasto-plastic model is characterized by the same stiffness during the entire mechanical process and hardening or time-dependent effects represent the inelastic phenomena inside the material. The Helmholtz free energy can be decoupled into its elastic and inelastic part, characterizing the hardening/softening behavior of the material

$$\Psi = \Psi\left(\boldsymbol{\varepsilon}_e, \mathbf{V}_k\right) = \Psi_e(\boldsymbol{\varepsilon}_e) + \Psi_i(\mathbf{V}_k). \tag{A.12}$$

In the simplest 1D model just one internal variable is used to describe the evolution of plasticity, the two energy components in Eq. (A.12) have the following expressions

$$\Psi_e(\varepsilon_e) = \frac{1}{2} E \varepsilon_e^2, \tag{A.13}$$

$$\Psi_i(\xi_p) = \frac{1}{2} h_p \xi_p^2. \tag{A.14}$$

where h_p is the hardening/softening parameter (negative for softening behavior) and ξ_p is the internal kinematic variable.
Deriving Ψ with respect to the kinematical variables, the corresponding static variables are obtained

$$\sigma = \frac{\partial \Psi}{\partial \varepsilon_e} = E \varepsilon_e, \tag{A.15}$$

$$\chi_p = \frac{\partial \Psi}{\partial \xi_p} = h_p \xi_p. \tag{A.16}$$

A unique activation function, written in terms of σ and χ_p, is needed to describe the evolution of plasticity. This can be expressed in a way similar to the strengths criteria where a variation in the threshold level of strength is admissible

$$\Phi_p(\sigma, \chi_p) = f(\sigma) - \sigma_0(1 + \chi_p) \leqslant 0 \tag{A.17}$$

Appendix B

Preventing rigid body motion by means of periodic BCs

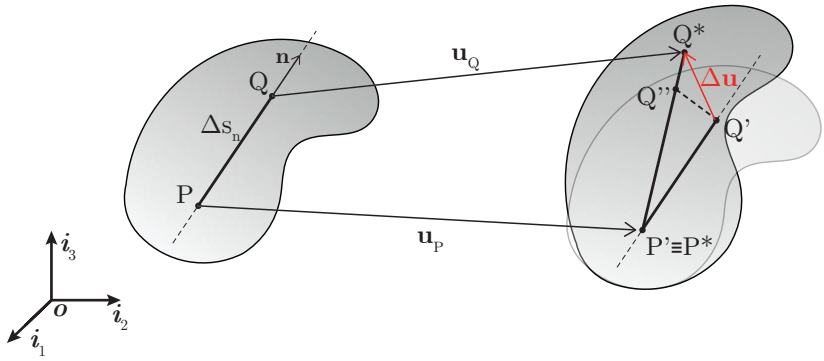

Figure B.1: Description of a change in the configuration of a fiber PQ in a solid.

In classical continuum mechanics, a change in the configuration of a generic material fiber PQ, with length Δs_n, oriented along a direction defined by the vector $\mathbf{n}$, can be described considering three sub-steps of motion as follow (see Fig. B.1):

1. Rigid translation, the two ends of the fiber shift describing the same displacement, from P to P' ($\mathbf{u_P}$) and from Q to Q';
2. Rigid rotation, the end Q' rotates around P' moving to Q" and the fiber align itself with the direction of the final configuration;

3. Uniaxial extension, Q" shifts in Q* and the vector $\mathbf{u_Q}$ is described.

The relative displacement $\Delta\mathbf{u}$, equal to the difference between $\mathbf{u_Q}$ and $\mathbf{u_P}$, can be expressed as a function of the displacement gradient of the fiber having origin in P and direction $\mathbf{n}$, $\boldsymbol{\delta}_n$. Moreover, the displacement gradient can be divided into the symmetry part, $\boldsymbol{\varepsilon}$ deformation tensor, and the asymmetry part, $\boldsymbol{\rho}$ rotation tensor:

$$\Delta\mathbf{u} = \boldsymbol{\delta}_n \Delta s_n = \boldsymbol{\varepsilon}\mathbf{n}\Delta s_n + \boldsymbol{\rho}\mathbf{n}\Delta s_n. \tag{B.1}$$

Since $\mathbf{n}\Delta s_n$ represents the vector $\overrightarrow{\mathrm{PQ}}$ and the periodic boundary condition reads $\Delta\mathbf{u} = \boldsymbol{\varepsilon}\overrightarrow{\mathrm{PQ}}$, the condition:

$$\boldsymbol{\rho}\overrightarrow{\mathrm{PQ}} = 0 \rightarrow \boldsymbol{\rho} = 0 \tag{B.2}$$

has to hold, i.e. rigid rotation is prevented if periodic boundary conditions are applied. This aspect is not always considered and some authors include the rotation in the rigid body constraints when dealing with periodic BCs [1].

Acknowledgements

La presente tesi è frutto di un percorso di ricerca svolto presso il Dipartimento di Ingegneria Civile, Ambientale, Aerospaziale, dei Materiali dell'Università di Palermo (DICAM).
Ringrazio tutte le persone che hanno fornito un contributo per lo svolgimento di tale percorso:
il professore Giuseppe Giambanco, per essere stato la principale guida di tutto il lavoro svolto, per avermi introdotto in sempre interessanti ambiti scientifici, per la sua capacità di coinvolgimento, i suoi consigli, la sua professionalità e l'interesse per la ricerca trasmesso;
il ricercatore Antonino Spada, con cui ho condiviso questo lungo lavoro di ricerca e da cui ho appreso l'attenzione per il dettaglio, l'onestà e l'umiltà intellettuale;
il professore Piervincenzo Rizzo, per avermi accolto nella mia prima esperienza di ricerca a Pittsburgh ed aver contribuito ad accrescere il mio curriculum accademico;
il professore Milan Jirásek, per aver arricchito il mio bagaglio con il suo excursus di studi discusso in occasione della summer school a Praga nel Settembre 2016;
tutto il personale docente DICAM che ha contribuito alla mia formazione in questi tre anni;
i colleghi e amici Pietro, Francesco, Gioacchino, Natalia, Mohsen, Marco, Fabio, Francesco, Gabriele, Jennifer, Giovanni, Vincenzo, per i consigli e lo svago dentro e fuori il luogo di lavoro.
In ultimo ringrazio la mia famiglia per aver costituito il supporto e l'ispirazione per il raggiungimento di questo traguardo.

Palermo, 20/12/2016